אוניברסיטת בן -גוריון בנגב
הפקולטה למדעי הטבע
המחלקה לפיסיקה

שיפור שחרור המלכודת לשם מדידת תכונותיהם של ענני אטומים קרים

מאת: רמון סמוק
בהנחיית: פרופ' רון פולמן

תמוז ה'תשע"א   יולי 2011

אוניברסיטת בן -גוריון בנגב
הפקולטה למדעי הטבע
המחלקה לפיסיקה

שיפור שחרור המלכודת לשם מדידת תכונותיהם של ע ennי אטומים קרים

חיבור זה מהווה חלק מהדרישות לקבלת התואר "מוסמך למדעי הטבע" (.M.Sc)

מאת: רמון סמוק
מנחה: פרופ' רון פולמן

חתימת הסטודנט: _____   תאריך: _____
חתימת המנחה: _____   תאריך: _____
חתימת יו"ר הועדה המחלקתית: _____   תאריך: _____

יולי 2011

Optimizing Trap Release for Measuring Properties of Cold Atomic Clouds

by

Ramon Szmuk

Submitted to the Department of Physics
in partial fulfillment of the requirements for the degree of

Master of Physics

at the Ben Gurion University July 2011

Ramon Szmuk, 2011.

Author . . . .
Department of Physics
July 31, 2011

Certified by . . . .
Ron Folman
Professor
Thesis Supervisor

Accepted by . . . .
Michael Gedalin
Chairman, Department Committee on Graduate Students

שיפור שחרור המלכודת לשם מדידת תכונותיהם של ענני אטומים קרים

מאת
רמון סמוק

תקציר

השבב האטומי (AtomChip) הוא התקן המבוסס על טכנולוגיות שך תעשית המיקרואלקטרוניקה המאפשר את לכידתם של אטומים קרים תוך ביצוע פעולות קוואנטיות עליהם.

הדיוק הרב בשיטה זו מתאפשר באמצעות לכידת אטומים במלכודות זעירות (מיקרו-פוטנציאלים) הנוצרים כתוצאה מהעברת זרמים בחוטים השונים של השבב. זרמים אלו יוצרים שדות מגנטיים שמהם יוצרים את המלכודות.

בפרט, ניתן באמצעות השבב ללכוד עיבוי בוזה-איינשטיין (Bose Einstein Condensate) אשר באמצעותו ניתן לחקור תופעות בסיסיות של מכניקת הקוואנטים.

עבודה זו מתמקדת במניפולציה של עיבוי בוזה-איינשטיין באמצעות השדות המגנטיים הנוצרים עלי ידי השבב האטומי.

מטרת עבודה זו היה לשפר את הניסוי במעבדה כך שניתן יהיה למדוד תבניות התאבכות הנוצרות כתוצאה משחרור עיבוי בוזה-איינשטיין מן המלכודות. תבנית התאבכות שכזאת טרם נראתה על גבי התקן השבב האטומי.

Optimizing Trap Release for Measuring Properties of Cold Atomic Clouds

by Ramon Szmuk
Submitted to the Department of Physics
on July 31, 2011, in partial fulfillment of the
requirements for the degree of
Master of Physics

Abstract

An AtomChip is a device that allows the trapping and manipulation of cold atoms with high accuracy using potentials created on a substrate by employing lithographic methods similar to those used in integrated circuit technology. In particular, the trapping and control of a Bose-Einsten Condensate (BEC) with such methods allows the investigation of fundamental aspects of quantum mechanics such as coherence and entanglement. This work focuses on the manipulation of a BEC by magnetic potentials created by gold current carrying wires on a silicon substrate.

The goal of this work was to optimize an experiment so that it could detect interference fringes emerging from a 1D lattice of traps. Such an interference pattern has not been seen before on an AtomChip. The complexity of the experiment requires several preparation stages, each of which may be considered a research project in its own right. It is these preparatory projects which were the goal of my work.

As part of this program, I have conducted the following research projects:

1. I performed a theoretical study of the emergence of interference patterns originating from a BEC released from a periodic potential generated by our AtomChip. The particular geometry of the potential and imaging limitations are shown to inhibit the direct observation of such fringes. We then perform a simulation of the BEC dynamics and show that gradually changing the potential in the release stage can overcome these difficulties.

2. The parameters found from the simulation analysis have been used to design and build dedicated electronics hardware that will allow us to perform such a task in the future.

3. In order to be able to assist with the loading of the atoms into the 1D lattice, I designed and built a new imaging system. At this stage, the new system was used to evaluate the cloud position relative to the various AtomChip elements. This allowed us to observe alignment problems with our previous design and has helped us design and install a new AtomChip for which the imaging system has shown that no such alignment issues remain.

4. In order to be able to further optimize the signal, once a first interference pattern is observed, I implemented an advanced control system that would enable automated optimization of the experiment by employing artificial intelligence algorithms. The new system has been tried on existing experimental signals.

All four projects were successfully carried out.

Thesis Supervisor: Ron Folman
Title: Associate Professor

Acknowledgments

A long list of amazing people made my whole experience at Ben-Gurion University very special, people with whom I was able to discuss various topics in physics during innumerable cups of coffee and who helped shape my understanding of physics and life in general.

First of all, I would like to thank my supervisor, Prof. Ron Folman, who was always available for discussions about physics and who devoted large chunks of his time supporting my work with his many ideas. Your guidance and insights will stay with me for the remainder of my life.

A special warm thanks to Dr. Mark Keil, who guided my work as the researcher in charge of the experiment and whose encouragement and support made progress possible. The long hours you invested working with me on this thesis pushed me forward and made the whole thing possible. You taught me the value of details and kept me focused throughout.

I would like to thank Ran Salem, Tal David and Julien Chabé, the PhD and Post-doc students in charge of the experiment when I arrived, for their patience when I was still too young to decipher the labyrinth that is a lab, and for their support and friendship that kept me going when things did not work out as expected.

I would also like to thank former student Yenon Benhaim for many interesting discussions and for taking the time to teach me many basic aspects of atomic physics, without whom my first steps in the lab would have been much harder to take.

I would like to thank the rest of the group members: Shimi Machluf, Plamen Petrov and Jonathan Coslovsky, the BEC-2 team, for their indispensable help along the way and for their interest and long discussions into fundamental aspects of quantum mechanics. And to the Raman group members: Meni, David, Gal, Amir, and especially Ruti, for our long discussions into philosophy and the implications of it all.

The work in the lab could not have been carried out without the help of our electronic wizard Zina, who was always available to fix a broken amplifier and design state-of-the-art shutters. And for the fabrication people, especially Yaacov, for fabricating the BGU1 chip.

A million thanks to our theoretician Yoni Japha, with whom I have spent numerous hours discussing theoretical issues, who was always there and enthusiastically willing to engage into long discussions about the motivations for our experimental work, and who spent many hours patiently working with me on this thesis.

Finally, this whole adventure would not have been possible without the loving support of my wife Irit, who had to sleep alone for many nights only to have me wake her up at 6 A.M. when I finally went to sleep, and my parents Nitza and Peter and sister Lital for convincing me from a very young age that I could do anything I wanted and provided the power tools (both psychological and electrical) to do so.

Contents

Chapter 1

Introduction

> So long as *big* and *small* are merely relative concepts, it is no help to explain
> the big in terms of the small. It is therefore necessary to modify classical ideas
> in such a way as to give an absolute meaning to size. ...In order to give an
> absolute meaning to size, such as is required for any theory of the ultimate
> structure of matter, we have to assume that *there is a limit to the fineness of*
> *our powers of observation and the smallness of the accompanying disturbance -*
> *a limit which is inherent in the nature of things and can never be surpassed by*
> *improved technique or increased skill on the part of the observer.*

Principles Of Quantum Mechanics - P.A.M. Dirac

This quote from the seminal book of Dirac [1] illustrates a basic conceptual difficulty in our understanding of Quantum Mechanics. The abstract concept of the state of a system, coupling together both the object at interest and the very act of observing it, lies at the heart of this difficulty. By using Heisenberg's uncertainty relations (assumed quite remarkably from basic philosophical principles) Dirac treats Planck's constant as a universal scaling factor that determines objectively what "small" and "big" really mean. A system is then said to be big if the act of measuring disturbs it only negligibly and it is said to be small if it disturbs it measurably. In the early days of quantum mechanics and up to recent years, physicists striving for a better grasp of the fundamental aspects of the theory had few tools to explore the basic questions it poses. Questions regarding the exact meaning of the state vector or the nature of its reduction (or collapse), were considered metaphysical questions that where beyond the scope of physics. The difficulties encountered in approaching these questions until quite recently has both historical and technical reasons. Historically, the

impression of the vast majority of physicists was that "Bohr had eventually won the debate with Einstein, so that discussing again the foundations of quantum mechanics after these giants was pretentious, useless, and maybe even bad taste" [2]. This position, together with the sheer counter-intuitive character of the theory caused a dearth in the successful studies of these questions lasting several decades.

But there is another, more technical reason, that these questions were not raised, namely due to a lack of the right kind of experimental systems capable of shedding light on such problems. In the early days of quantum mechanics, the objects to which the theory was applied were either small and simple or big and complex. Small systems, in the sense that probing them causes a disturbance that is not negligible, did not allow for conceptions of isolated quantum phenomena to be formulated (such as in early work on atomic systems). Big systems on the other hand, had the advantage of being associated with a measurement process that caused negligible disturbance, but were nevertheless too complex (such as superfluids, superconductors or various solid state systems just to name a few) to be described in terms of isolated quantum phenomena, making it virtually impossible to draw a boundary between "intensive" and "extensive" research [1]. For example, the recognition that particles obeying the Schrödinger equation can tunnel through classically impenetrable barriers is considered as one of the first successes of the quantum theory [4]. However, despite the success in calculating various tunneling rates (an emergent phenomena), asking what is the time it takes a single particle to tunnel through a barrier (a fundamental process) is still an open question [5]. Experimental observations of the tunneling of a single quantum state are quite recent (see for example [6]) and the multitude of possible theoretical descriptions of this basic phenomena only shows how deficient our current understanding of quantum mechanics really is, precisely because this problem forces us into a discussion on the fundamental nature of the state vector.

In the early stages of the development of the theory, systems which were both simple and weakly coupled to a measurement process simply did not exist, and experimentalists as well as theoreticians had no models with which they could investigate isolated quan-

---

[1]To quote Weisskopf [3]: "Looking at the development of science in the Twentieth Century one can distinguish two trends, which I will call "intensive" and "extensive" research, lacking a better terminology. In short: intensive research goes for the fundamental laws, extensive research goes for the explanation of phenomena in terms of known fundamental laws. As always, distinction of this kind are not unambiguous, but they are clear in most cases. Solid state physics, plasma physics, and perhaps also biology are extensive. High energy physics and a good part of nuclear physics are intensive."

tum phenomena. A lack of such experimental systems in a way limited the scope of the theory to the application of the axiomatic structures that were set up by Bohr, Einstein, Heisenberg, Pauli, de-Broglie and others in the Solvay meetings [7] (what later emerged as the "Copenhagen interpretation") without much questioning into its various fundamental aspects. This adoption of the orthodox formulation of the theory was later termed by N. Mermin the "shut up and calculate" interpretation of quantum mechanics [8]. This way of doing quantum physics however, is becoming less and less popular in recent years, in some part due to the fact that new experimental and theoretical tools have been developed that allow the creation of macroscopic quantum states ("big" systems in Dirac's parlance) that push the borders of the quantum world to larger and larger systems that are still neverthe-less described as single quantum objects. Since the measurement process can in these cases be treated as a negligible perturbation, it allowed (some would say forced) physicists to study isolated quantum phenomena and begin again to ponder on the fundamental aspects of quantum mechanics. One of those macroscopic quantum systems, the Bose-Einstein Condensate (BEC) and ultra-cold bosons in general, is the topic of this thesis. The following section will describe what a BEC is and how it is instrumental in answering fundamental questions of quantum mechanics.

1.1 Ultracold atomic physics

The classical formulation of statistical mechanics treats particles as distinguishable entities. Quantum mechanics on the other hand rejects this notion [9, 10]; particles with identical properties are treated as fundamentally indistinguishable and consequently their statistical behavior changes drastically. When bosons are cooled and compressed beyond a critical point a phase transition occurs in which a macroscopic number of atoms occupy the ground state [10], individual atom movement is suppressed and only coherent motion of the whole cloud is possible [11]. This new phase, called a Bose-Einstein Condensate (BEC), is a new state of matter in which the atoms are described by a single macroscopic wavefunction which evolves quantum mechanically. The transition from a classical thermal gas to a Bose-Einstein condensate occurs when the phase space density (PSD) reaches a value [10]: $n\lambda_T^3 \sim 1$, where n is the atom density and $\lambda_T = h/\sqrt{2\pi m k_B T}$ is the thermal de-Broglie wavelength [10]. The PSD represents the amount of overlap the single-particle wavefunctions

experience, thus providing a measure of the system's coherence. For PSD> 1 quantum behavior emerges and a purely classical analysis treating particles as distinct entities no longer holds. The cooling and compression processes required to satisfy this condition were made possible only recently [12, 13] by applying the techniques of laser cooling and evaporative cooling.

After the discovery of BECs, their properties and behavior have been studied extensively [14, 15]. The macroscopic wavefunction of a BEC evolving in a certain potential landscape resembles that of a single particle wavefunction. Upon measurement the macroscopic wavefunction reduces to N individual particles which are then found at positions that correspond to the amplitude of the wavefunction. It is said then that the wavefunction of a BEC has the classical interpretation of being the atomic cloud's density function, a feature that in fact allows experimentalists a tool to measure "single-particle" like wavefunctions in a single experimental run since measuring a BEC is similar to performing N separate measurements on individual particles (neglecting interactions). BECs then allow us to measure a multitude of fundamental quantum mechanical phenomena, from foundations of quantum mechanics [16, 17, 18] to solid state physics [19, 20, 21], to quantum information processing [22, 23] and even high-energy physics and cosmology [24, 25]. In addition to fundamental physics BECs can also be used for interferometry [26, 27, 28] and since BECs can be number squeezed [29, 30, 31] they are capable of surpassing the Heisenberg limit [32] and are thus expected to take a fundamental role in future quantum metrology [33].

The quantum mechanical behavior of BECs is frequently observed through the detection of interference patterns produced from splitting and later recombining the condensates. This technique allows experimentalists to directly measure coherent properties of the macroscopic wavefunction associated with a condensate. BECs are also used to study solid state systems by trapping them in periodic potentials, thus simulating particle-in-a-lattice type systems. This is the main objective of our research. We have designed and built a system capable of generating a one dimensional lattice (details of which will be discussed later) in order to study various phenomena occurring in one dimensional periodic potentials. We aim to measure coherent behavior of the trapped BEC by imaging interference fringes originating from BECs released from the sites of our engineered lattice. This objective poses several problems associated with the particular geometry of the potentials we are capable of producing and it is one of the goals of this thesis to explore these difficulties and propose

experimental solutions so that the anticipated interference patterns can be detected.

In the following chapters we will describe our setup for creating and manipulating cold quantum gases using the AtomChip [34] technology which allows for the miniaturization and integration of cold atom experiments by adapting semiconductor technology to the field of matter wave optics. The scope of this work is threefold: to study how interference fringes originating from the overlap of separated BECs can be observed in our system, during which we will identify some problems with the detection of such fringes and propose a solution. To design and build an imaging system to aid in the positioning of the cloud relative to the AtomChip elements, and to create an automatic optimization system for the various system parameters. A fourth sub-project was to construct appropriate electronics, but this will not be elaborated upon.

The precise structure of the thesis is described in the following section.

1.2   Overview of this thesis

This thesis is structured as follows: chapter 2 reviews the basic theoretical tools required for the analysis of our experiment. We discuss the basic atomic structure of ^{87}Rb, an atom from the alkali metal family used in our experimental setup. We follow with a description of the fundamental processes used to trap and cool atoms and the theory of trapped BECs in harmonic potentials.

Chapter 3 presents the experimental apparatus with its various subsystems including the computer control system and the analysis software. A separate section is devoted to the new AtomChip recently installed in the apparatus, along with a discussion of its various wires.

Chapter 4 details our proposal for measuring interference patterns originating from expanding BECs from several sites in a one dimensional magnetic lattice. Several problems that suppress the fringe contrast are discussed and a way to overcome these difficulties is presented. In this chapter we also describe theoretical calculations explaining the underlying phenomena together with detailed simulations of the cloud's expansion showing how our proposed solution solves the problem.

Chapter 5 presents the motivation and construction of a new imaging system embedded into our setup together with a discussion of the properties of the resulting images and their

usefulness.

Finally, in Chapter 6 we discuss the theoretical foundations of genetic algorithms (GAs) and their implementation in our system for the optimization of various processes. The various algorithm parameters and their meaning is also discussed, followed by a few examples showing the successful implementation of the methods.

We end the thesis with a brief summary and conclusions chapter.

Chapter 2

Theoretical Background

2.1 Atomic structure of the alkali elements

In this section we will review the tools required for the theoretical study of atomic physics. This will include a discussion of atomic structure, interactions with electromagnetic radiation, and many-body phenomena relevant to ultracold interactions. The most natural platform to derive the Hamiltonian of an atomic system is Relativistic Quantum Mechanics (RQM) and specifically Dirac's equation [1]. RQM is the birthplace of the intrinsic angular momentum (or spin) degree of freedom which plays a central role in atom trapping and cooling. Relativistic corrections appear naturally in such a derivation without the need for hand-waving arguments. We begin from the Dirac equation for an electron in the presence of a centrally symmetric potential $V(r)$ and look for stationary solutions (eigenvectors of the energy operator [35]:

$$\hat{H}\vec{\psi}(r) = [c\hat{\boldsymbol{\alpha}} \cdot \hat{\boldsymbol{p}} + \beta m_e c^2 - q_e V(r)]\vec{\psi}(r) = E\vec{\psi}(r), \tag{2.1}$$

where $\hat{\boldsymbol{p}}$ is the momentum operator and

$$\hat{\boldsymbol{\alpha}} = \begin{pmatrix} \hat{\boldsymbol{0}} & \hat{\boldsymbol{\sigma}} \\ \hat{\boldsymbol{\sigma}} & \hat{\boldsymbol{0}} \end{pmatrix} \qquad \qquad \beta = \begin{pmatrix} \hat{\boldsymbol{1}} & \hat{\boldsymbol{0}} \\ \hat{\boldsymbol{0}} & -\hat{\boldsymbol{1}} \end{pmatrix} \tag{2.2}$$

with $\hat{\boldsymbol{\sigma}} = (\sigma_x, \sigma_y, \sigma_z)$ being the familiar Pauli matrices.

We notice that unlike in the non-relativistic case (Schrödinger's equation), the orbital angular momentum operator $\hat{\boldsymbol{L}}$ is not a constant of motion in RQM since it does not

commute with the Hamiltonian (it commutes with the momentum operator squared $\hat{p}^2$ but not with $\hat{p}$, for example see for $\hat{L}_x = yp_z - zp_y$). However, the new operator:

$$\hat{\boldsymbol{J}} = \hat{\boldsymbol{L}} + \frac{\hbar}{2}\begin{pmatrix} \hat{\boldsymbol{\sigma}} & \hat{\boldsymbol{0}} \\ \hat{\boldsymbol{0}} & \hat{\boldsymbol{\sigma}} \end{pmatrix} = \hat{\boldsymbol{L}} + \hat{\boldsymbol{S}} \tag{2.3}$$

does commute with H and is thus a new constant of motion[1].

The operator $\hat{\boldsymbol{J}}$ we have introduced is interpreted as the total angular momentum while $\hat{\boldsymbol{S}}$ is referred to as the intrinsic, or spin angular momentum, a new degree of freedom with units of angular momentum but with no classical analogy. Some authors [36] treat the spin as a consequence of the linearization of the wave equation and not due to a relativistic effect. This perspective neglects the fact that the linearization of the wave equation has the proper relativistic motivation [1] of having an equation which transforms in a simple way under Lorentz transformations. This is done by giving an equal footing to the spatial and time coordinates (since the equation is linear with respect to time). Conversely, one could also argue that the experimental observation of spin confines us to theories with a linear form.

We now plug in a Coulomb potential interaction $V(r) = -\frac{Z'e^2}{4\pi\epsilon_0 r}$ in Eqn. 2.1, take the first-order terms of a non-relativistic approximation ($\frac{v}{c} \ll 1$) and after some algebraic manipulations arrive at the fine structure equation for the energy eigenvalues [35]:

$$E\vec{\psi} = \left(\frac{\hat{p}^2}{2m} - \frac{\hat{p}^4}{8m^3c^2} - \frac{Z'e^2}{4\pi\epsilon_0 r} + \frac{Z'e^2\hbar^2}{8\epsilon_0 m^2 c^2}\delta^3(r) + \frac{Z'e^2\hat{\boldsymbol{L}}\cdot\hat{\boldsymbol{S}}}{8\pi\epsilon_0 m^2 c^2 r^3} \right)\vec{\psi}, \tag{2.4}$$

where we have treated the nucleus as a point particle with an effective charge $+Z'e$ that accounts for the shielding of the nuclear charge by the core electrons and where we wrote for the potential $\vec{\nabla} \cdot \vec{V} = \frac{\rho}{\epsilon_0} = \frac{Z'e}{\epsilon_0}\delta^3(\vec{r})$.

In this expression the first and third terms give the non-relativistic Hamiltonian, the second term is the classical relativistic correction to the energy, while the fourth term is the so-called Darwin term [37] which has no classical analogy, and the final term is the celebrated spin-orbit coupling which appears naturally from the Dirac equation. The spin-

---

[1]Following Ehrenfest theorem: $\frac{d}{dt}A = \frac{1}{i\hbar} < [A, H] >$, where A is any time independent operator, commuting with the Hamiltonian results in $\frac{dA}{dt} = 0$.

orbit interaction causes the energy of the atom to depend not only on the absolute magnitude of the operators $\hat{\boldsymbol{L}}$ and $\hat{\boldsymbol{S}}$ but also on their orientation relative to each other, subsequently only the total angular momentum $\hat{\boldsymbol{J}} = \hat{\boldsymbol{L}} + \hat{\boldsymbol{S}}$ is conserved and not $\hat{\boldsymbol{L}}$ and $\hat{\boldsymbol{S}}$ separately. This first order relativistic effect breaks the $(2S+1)$ degeneracy of the atomic energy levels and causes the well known fine-structure splitting of spectral lines in atomic physics.

Up to now we have treated the nucleus as a point charge. In general however, the full interaction between the atomic electrons and the nucleus can be expanded in a multipole series [38]:

$$H_{int} = \sum_k T^k(N) \cdot M^k(e), \tag{2.5}$$

where $T^k(N)$ and $M^k(e)$ represents the multipole expansion of the electromagnetic field of the nucleus and electrons respectively. Since the atomic potential is isotropic, the atomic wavefunctions are symmetric with respect to space reflections and are thus also eigenfunctions of the parity operator $(\hat{P}\vec{\psi}(r) = \vec{\psi}(-r) = \pm\vec{\psi}(r))$. For this reason, only terms in the expansion that do not change the parity of the state have non-zero expectation values. Since the electric and magnetic field operators have parity eigenvalues $(-1)^k$ and $(-1)^{k+1}$ respectively, the only terms which remain are the even electric and odd magnetic terms in the expansion. The contributions are the electric monopole, which is just the electric charge, the magnetic dipole, the electric quadrupole and the magnetic octupole which has not been observed up to now in ^{87}Rb. This should not to be confused with electric or magnetic dipole transitions in which different states of the atom are coupled by an external electromagnetic field. Here we are discussing the terms in the multipole expansion of the unperturbed atom (nucleus + electrons) contributing to its energy level structure. The terms scale as m_e/m_p and so their effect is smaller by a factor of about 1000 between successive terms. The expansion stops at the octupole moment (k=3) for ^{87}Rb, since the largest possible rank of the tensors involved cannot exceed twice the nuclear spin [9] (which for ^{87}Rb is $I = 3/2$). Plugging in the various expressions for the multipole expansion [38] up to the electric quadrupole term one obtains the following expression for the energy levels:

$$E_{n,I,j} = -\frac{Z'^2 m e^4}{8 h^2 n^2 e_0^2}\left[1 + \frac{(Z'\alpha)^2}{n^2}\left(\frac{n}{j+1/2} - \frac{3}{4}\right)\right] + \frac{1}{2}hAK + hB\frac{\frac{3}{2}K(K+1) - 2I(I+1)J(J+1)}{2I(2I-1)2J(2J-1)},$$
$$\tag{2.6}$$

where we wrote $K = F(F+1) - I(I+1) - J(J+1) = 2I \cdot J$ and have used the constants A and B that can be obtained either from theory or from experimental measurements, and that depend on the specific level of interest [39].

In doing this we have treated I, J, and F as good quantum numbers, justified by the fact that the splitting originating from the $I \cdot J$ coupling in Eqn. 2.6 (the hyperfine splitting) is much smaller than the energy difference between levels with different J values, and certainly much smaller than the energy levels involved in changing the nuclear state. The total angular momentum F is always a good quantum number since the total angular momentum of a closed system is a conserved quantity (isotropy of space).

To obtain exact values for the energy levels from these theoretical considerations one first needs to find the principal energy level E_n prior to any fine or hyperfine splitting. This is not a simple matter since the Rydberg formula does not provide us with a good estimate for multi-electron atoms (such as rubidium) which are much heavier than hydrogen. To obtain the basic energy levels one needs to use effective values for the nuclear charge number Z (as previously discussed) or the principal quantum number n to account for various shielding effects. Eventually, semi-empirical values are obtained and the role of the theoretical model just reviewed is reduced to a qualitative discussion on the origins of the various energy level splittings. Nevertheless, the similarity of the alkali family of atoms to hydrogen (a characteristic single unpaired electron) render their spectroscopy and interactions with magnetic fields relatively simple to analyze, allowing one to grasp the fundamental processes using simple theoretical considerations. For these reasons, as well as for practical advantages (such as a split ground state and closed loop transitions), this group of atoms have taken a central position in the study of ultracold atomic physics.

Eventually one obtains for the three lowest energy levels of ^{87}Rb the structure depicted in Fig. 2-1. The colored arrows represent the four atomic transitions employed in our experimental cycle. The transitions are excited using laser radiation emitted from diode lasers which are locked to nearby atomic transitions. In the following sections we will describe in detail how we exploit this particular atomic system to create interesting quantum states that help enable studies of fundamental questions of quantum mechanics.
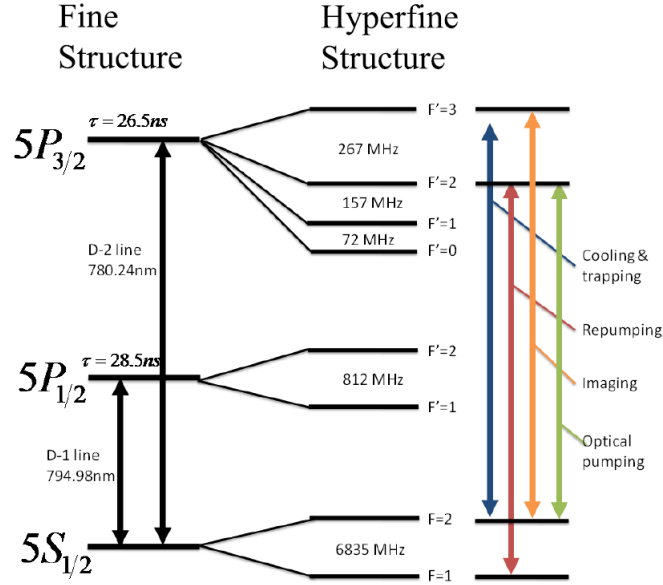
Figure 2-1: The hyperfine structure of ^{87}Rb. The energy level structure is shown with the optical transitions used for laser cooling and trapping and the lifetime (τ) for spontaneous emission to the ground state from the various levels. Taken from [40].

2.2 Interactions with a magnetic field

Since each of the hyperfine levels discussed in the previous section contains $2F+1$ degenerate magnetic sublevels, applying a magnetic field lifts the degeneracy (Zeeman splitting). An inhomogeneous field will therefore create a spatially dependent shift of the sublevels which, as we shall see below, allows a trapping potential to be formed for the atoms.

In general, there are three contributions to the atomic magnetic dipole, originating from the electron's intrinsic spin, its orbital angular momentum, and the nuclear magnetic dipole:

$$H_B = \frac{\mu_b}{\hbar}(g_s\hat{\boldsymbol{S}} + g_l\hat{\boldsymbol{L}} + g_I\hat{\boldsymbol{I}}) \cdot \hat{\boldsymbol{B}} = \frac{\mu_B}{\hbar}(g_S S_z + g_L L_z + g_I I_z)B_z. \tag{2.7}$$

For magnetic fields of around $10\,\mathrm{G}$, this Zeeman term in the Hamiltonian is much smaller than the level spacing of the hyperfine structure ($\mu_B/h \approx 1.4\,\mathrm{MHz/G}$). Treating this term as a perturbation allows us to keep treating F as a good quantum number and we can then write [39]:

$$H_B = -\hat{\boldsymbol{\mu}} \cdot \hat{\boldsymbol{B}} = \mu_B g_F m_F B_z = \mu_z B_z, \tag{2.8}$$

19

where g_F is the hyperfine Lande g-factor given by:

$$g_F \cong \frac{F(F+1) - I(I+1) + J(J+1)}{2F(F+1)}. \tag{2.9}$$

We notice that for cases with $g_F m_F > 0$ we have an energy term that increases the atom's energy for increasing fields. Such states are called low-field seeking and are attracted to a minimum of the magnetic field. In the opposite situation, states for which $g_F m_F < 0$, are called high-field seeking states and are attracted to field maxima. Due to Earnshaw's theorem [41], no magnetic field maxima are allowed in space since no magnetic monopoles seem to exist. This reduces our possibilities for trapping atoms to the class of low-field seeking states, which unfortunately are not the lowest energy states. This reminds us that particles in such states could at times decay into the lower energy high-field seeking states which are not trappable, requiring us to always make sure such loss channels are dealt with.

In fact, Earnshaw's theorem also does not allow for a field minimum. We bypass this restriction by noting that the theorem does not forbid a minimum of the modulus of the filed. Hence, as long as an adiabaticity criterion is fulfilled we may use in Eqn. 2.8 the term $|B|$. This criterion requires that the rate with which the atom's spin may follow changes in the field direction (estimated to be proportional to the Larmor frequency ω_L) is much larger than the rate with which the magnetic field changes direction (estimated to be proportional to the trap frequency ω_T). We therefore write:

$$\omega_T \ll \omega_L, \tag{2.10}$$

where ω_L is:

$$\omega_L = \frac{g_F \mu_B}{\hbar} |\hat{\boldsymbol{B}}|. \tag{2.11}$$

We see that the adiabaticity condition may be violated in regions where the magnetic field becomes small. In such cases the atomic magnetic moment cannot follow the magnetic field and might flip its orientation relative to the field (to the more probable lower energy state), changing m_F and thus switching to a strong-field seeking state which is then repelled. Such events are referred to as Majorana spin flips and, as discussed in the Sec. 2.6, are an important consideration in the design of magnetic trapping potentials.

2.3   Doppler Cooling

Atoms moving against the propagation direction of a laser beam experience a blue detuning of the frequency (Doppler shift), so a laser must be red-detuned to maintain the resonance condition. Atoms moving towards such a red-detuned laser beam will scatter more light than atoms moving in the opposite direction and the absorption of the photon's opposing momentum will cause the atoms to slow down, thereby cooling them. To first order, the Doppler cooling force is proportional to the velocity, which results in a viscous damping of the motion. For this reason the effect gained the name "optical molasses" [42]. The limit of this cooling technique may be deduced by noticing that there is some heating caused by the spontaneous emission of photons. Although on average the velocity imparted by this spontaneous emission is zero (since it is isotropic), there is still a Brownian motion in momentum space due to the finite lifetime of the excited level in the absorbing atom. A limit on this process can be obtained from:

$$\Delta E \Delta t \geq \frac{\hbar}{2}, \tag{2.12}$$

where Δt is the excited level's lifetime and ΔE is the energy associated with the transition. After averaging over the ensemble, we can take the limiting value of this equation and write:

$$k_B T_D = \frac{\hbar}{2\Delta t} = \frac{\hbar}{2}\Gamma, \tag{2.13}$$

where Γ is the energy level linewidth and T_D is the Doppler limit – the lowest temperature allowed by the linewidth of the transition. This temperature is typically several hundred μK ($\sim 140\,\mu$K for ^{87}Rb) and represents the lowest attainable temperature for many radiation cooling schemes.

2.4   Magneto-optical traps

Now we describe a dissipative trapping potential that combines the velocity-dependent cooling force (provided by red-detuned counter-propagating laser beams) with the spatially-dependent trapping force (provided by the inhomogeneous magnetic field acting upon low-field seeking states) also known as a Magneto-Optical Trap (or MOT). In Fig. 2-2, we show two laser beams counter-propagating along the $\hat{z}$-axis (denoted by their circular polarization

states as σ^+ and σ^-) and red-detuned by a frequency δ from resonance (the horizontal line denoted by $M_e = 0$). An inhomogeneous magnetic field of $\vec{B} = B_z$ induces a linear Zeeman shift as shown for the three M sublevels of a presumed $J = 1$ excited state. This Zeeman shift brings atoms positioned to the right of the trap center (*e.g.*, at z') closer to resonance if they are in the $M = -1$ sublevel (*i.e.*, if they are excited by the σ^- beam), whereas atoms positioned on the opposite side of the trap will be closer to resonance if they are excited by the σ^+ beam to the $M = 1$ sublevel. In either case, an atom experiences a force pushing it to the center ($z = 0$). By adding two additional pairs of opposing laser beams along the x- and y-axes, the atoms can effectively be trapped in three-dimensional space and simultaneously cooled by the Doppler mechanism described in the previous section.
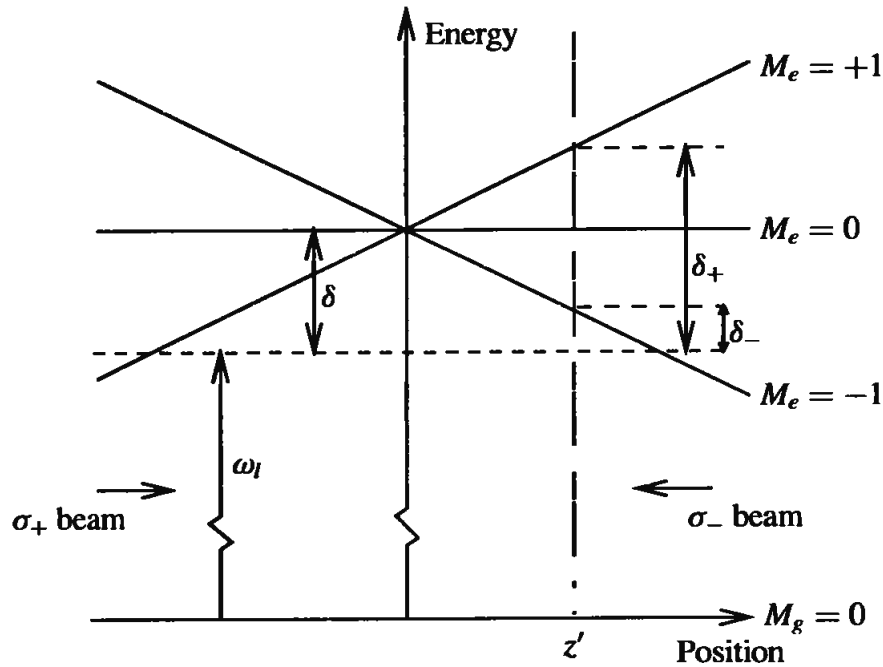

Figure 2-2: Arrangement of a MOT in 1D. Two counter propagating laser beams impinge on an atom at rest in the center of a quadrupole magnetic field. The horizontal dashed line represents the laser frequency (red shifted from resonance) as seen by the atom. Due to the inhomogeneous magnetic field the Zeeman shift is position dependent in a way that causes atoms on the right side of the trap center to be closer to resonance with the σ^- laser beam while atoms on the left are closer to resonance with the σ^+ beam. Consequently the atom feels a force directed towards the center of the trap. Taken from [43].

2.5 Sub-Doppler cooling

In a surprising experiment [44] temperatures two orders of magnitude lower than the Doppler limit were observed $(0.1 - 1\,\mu\text{K})$ in MOT experiments. This extra cooling can be explained as occurring due to a lag between the orientation of the atomic electric dipole moment and the optical field polarization vector [42]. To understand the origin of this effect we notice that the light pressure is given by the interaction of the atom's electric dipole with the laser electric field, i.e. its polarization vector. We then have for the force:

$$\hat{\boldsymbol{F}} = \nabla(\hat{\boldsymbol{d}}_{ge} \cdot \hat{\boldsymbol{E}}), \tag{2.14}$$

where d_{ge} is the dipole moment between the ground and excited levels (ge stands for the ground→excited transition). For an atom at rest at steady state the dipole moment is aligned with the polarization vector and will experience no net force. But if the optical polarization changes along the atom's path such as in the case of our $\sigma^+ - \sigma^-$ configuration, the atom's electric dipole will follow the polarization non-adiabatically and will lag behind it (see Fig 2-3), creating an angle that increases with the atom's velocity.
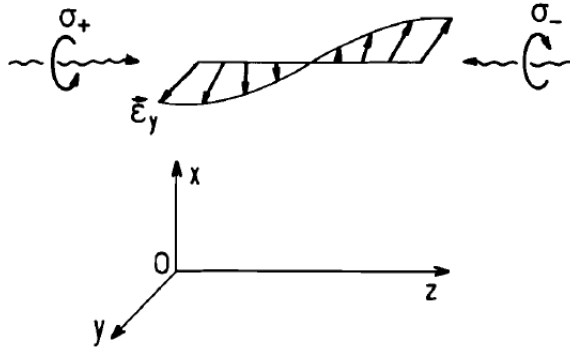

Figure 2-3: Polarization gradient cooling in 1D. Two counter propagating laser beams with σ^+ and σ^- polarizations create a linear polarization vector that rotates in space. When an atom moves through this field his electric dipole follows the optical field polarization vector with the angle between the atom's electric dipole and the optical field growing with the atom's velocity. For kinetic energies higher than $1\,\mu\text{K}$ the electric dipole lags behind the optical field, causing the process to be non-adiabatic. The force on the atom then becomes velocity dependent and thus dissipative. Taken from [42].

Such an angle will cause a net force on the atom that will oppose the motion causing it and a damping of the atomic motion will ensue. Microscopically, Dalibard et al. [42] showed that

the rotation of the quantization axis (the polarization vector) induces a higher population of the $m_F = +1$ state over the $m_F = -1$ one (in the ground state of the atom) when the atoms are moving towards the σ^+ beam and vice versa for the motion towards the σ^- beam. Since atoms in the $m_F = +1$ ($m_F = -1$) scatter light from the σ^+ (σ^-) beam more efficiently (due to the different Clebsch-Gordan coefficients) a net force opposes the atom's movement.

In contrast to the Doppler cooling mechanism whereby light is preferentially scattered due to frequency shifts induced by the Doppler effect, the polarization gradient cooling mechanism is responsible for preferentially scattering light due to the imbalance in the populations caused by the non-adiabatic following of the atomic orientation relative to the local field. In the mechanism discussed here, the cooling occurs for each scattering event, unlike in the case of Doppler cooling where cooling was a result of multiple absorption-emission cycles. For this reason the lowest temperatures attainable are set by the recoil energy of a single photon (with wavevector $\vec{k}$) and are not limited by the indeterminacy of the atomic linewidth:

$$k_B T_r = \frac{\hbar^2 k^2}{m},\tag{2.15}$$

This temperature is on the order of $1\,\mu\mathrm{K}$ and thus represents a further cooling by two orders of magnitude relative to the Doppler cooling mechanism, and is best achieved by closing the magnetic fields and further detuning the laser beams. Although extremely cold, $1\,\mu\mathrm{K}$ is still not enough to achieve a BEC where temperatures on the order of $200\,\mathrm{nK}$ are needed (required by the typical densities achievable with trapped gases). For such low temperatures different methods are employed such as evaporative cooling inside magnetic traps.

2.6   The AtomChip reflection MOT

In the case of AtomChip experiments, the chip blocks optical access along some directions, a situation which requires some modifications to the typical setup. Since the laser beams are reflected from the mirror-like surface of the AtomChip (see Fig. 2-4), the setup requires a quadrupole field rotated by 45 degrees relative to the chip surface. Such a field can be obtained by anti-Helmholtz coils with a 45 degree axis or more conveniently with a U-shaped wire (as shown in Fig. 2-5). This has received the name: The U-MOT.
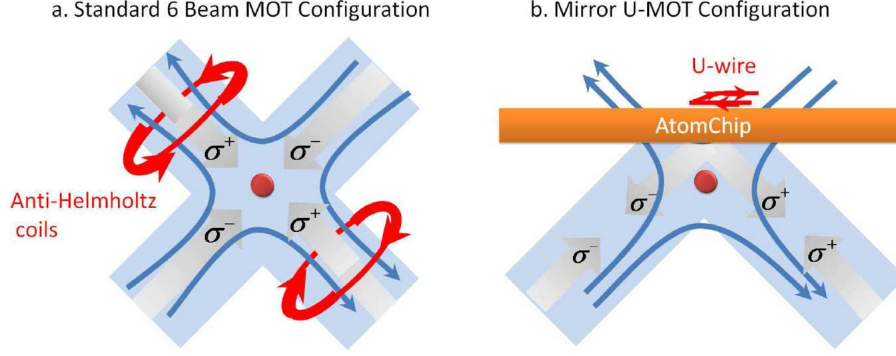
Figure 2-4: Six beam MOT Vs. Mirror MOT. a. A 2D cut through a standard 6-beam MOT b. mirror U-MOT configuration. The presence of the AtomChip prohibits one pair of beams from accessing the trapping region but fortunately also provides a solution to the problem. Since reflection reverses the circular polarization, using the AtomChip as a mirror the standard configuration of six beams with the proper polarization is maintained. Different than what is used in Fig. 2-2, the convention of polarization used here is that of the photon frame of reference. Taken from [40].

The U-wire can be regarded as a superposition of a central wire, a perpendicular bias field and two legs (the wire leads), the two legs carry currents in opposite directions, so that the net field in the middle is in the $\hat{z}$ direction. The wire together with the bias field creates an atom guide (see Fig. 2-6) for low-field seeking atoms, whose field minimum is zero, and the configuration is a two-dimensional quadrupole. By adding the two legs one creates "end caps" for the wire guide, and a 3D quadrupole is obtained.

Additionally, the U-wire trap configuration is preferred when working with AtomChips since one can form the initial MOT closer to the surface, thus allowing easier loading to the AtomChip in later stages and also permitting high magnetic field gradients due to the proximity of these wires to the atomic cloud. The MOT trap has the ability to collect a relatively large numbers of atoms, but at phase space densities that are much too low for the formation of a BEC (a typical phase space density at the MOT stage is 10^{-6}).

2.7 Magnetic traps

As previously mentioned, the point of vanishing magnetic field at the center of the quadrupole trap operates as a loss channel for cold atoms. As the temperature drops, atoms spend an increasing amount of time in the presence of low fields and spin-flip rates increase up to a point where losses become prohibitive. Consequently, in order to achieve lower temper-
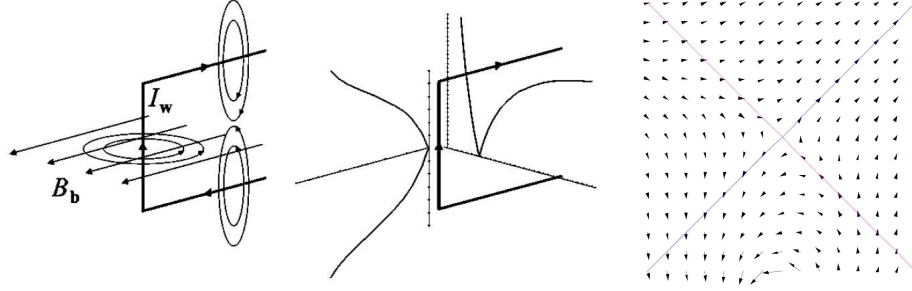
Figure 2-5: The U-MOT configuration. On the left, magnetic field lines produced by each segment of the U-wire are shown which, together with the bias field B_b, generates a confining potential along the wire axis and a sharp minimum of zero field at some distance z_0 from the wire. On the right we show the quadrupole field generated in a plane perpendicular to the central wire. In the central figure we show the radial and axial potentials of the generated trap. Notice however that in standard MOT configurations the orientation of the magnetic field (which acts as a quantization axis) relative to the direction of propagation of the laser beams is important. It might seem that our configuration will fail since the laser beams coming at 45° incidence are oriented differently than for the six-beam MOT. This confusion is resolved by noticing that the quadrupole field generated by the U-MOT is also rotated by 45° relative to standard configurations. Taken from [45] and [46].
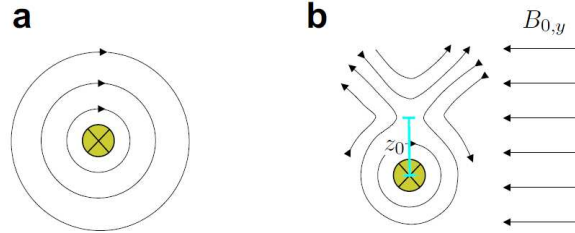

Figure 2-6: Sideguide potential. A sideguide generated from a single current-carrying wire and a perpendicular bias field. The one-dimensional guide is parallel to the wire at a distance of z_0.

atures a new trap is needed that does not have a zero magnetic field at its minima. In order to achieve a trap with high gradients and a non-zero minimum field we employ a Ioffe-Pritchard type of trap which is created by passing currents through a Z-shaped copper wire.

To understand the field configuration we first consider a sideguide generated by a single current-carrying wire (along the $\hat{x}$-axis) and a perpendicular bias field (along the $\hat{y}$-axis, see Fig. 2-6). This configuration has a field:

$$
\boldsymbol{B} = \frac{\mu_0 I}{2\pi(y^2 + z^2)} \begin{pmatrix} 0 \\ -z \\ y \end{pmatrix} + B_y \begin{pmatrix} 0 \\ 1 \\ 0 \end{pmatrix}, \tag{2.16}
$$

which due to the bias field along the $\hat{y}$-axis results in a cancellation of the overall field at the group of points $z_0 = (x, 0, \frac{\mu_0 I}{2\pi B_y})$.

This trap unfortunately is unsuitable for trapping since it suffers from the same condition of the previously encountered quadrupole, it has zero field at its center. If we apply another bias field along the $\hat{x}$-axis we will have:

$$
\boldsymbol{B} \approx \frac{\mu_0 I}{2\pi z_0^2} \begin{pmatrix} 0 \\ z_0 - z \\ y \end{pmatrix} + \begin{pmatrix} B_{0,x} \\ 0 \\ 0 \end{pmatrix} \tag{2.17}
$$

Creating an $\hat{x}$-bias field can be done by bending the wire to a Z-like shape (see Fig. 2-7 b), the bent legs now give a field at the waveguide of the form:

$$
\begin{aligned}
B_{z,legs} &= \frac{-\mu_0 I}{4\pi} \left(\frac{x + L}{z_0^2 + (x + L)^2} + \frac{x - L}{z_0^2 + (x - L)^2} \right) \\
&\approx -\frac{\mu_0 I}{2\pi} \frac{z_0^2 - L^2}{(z_0^2 + L^2)^2} x \\
B_{x,legs} &= \frac{\mu_0 I}{4\pi} \left(\frac{z_0}{z_0^2 + (x + L)^2} + \frac{z_0}{z_0^2 + (x - L)^2} \right) \\
&\approx \frac{\mu_0 I z_0}{2\pi(z_0^2 + L^2)} - \frac{\mu_0 I z_0 (z_0^2 - 3L^2)}{2\pi(z_0^2 + L^2)^3} x^2.
\end{aligned} \tag{2.18}
$$

and trapping frequencies given by:

$$
\begin{aligned}
\omega_\rho^2 &= \frac{\mu_B m_F g_F}{m} \times \frac{\partial^2 B}{\partial \rho^2} = \frac{\mu_B m_F g_F}{m} \times \frac{B_y^2}{z_0^2 B_{0,x}} \\
\omega_x^2 &= \frac{\mu_B m_F g_F}{m} \times \frac{\partial^2 B}{\partial x^2} = \frac{\mu_B m_F g_F}{m} \times \frac{\mu_0 I z_0 (z_0^2 - 3L^2)}{\pi(z_0^2 + L^2)^3} \approx \frac{\mu_B m_F g_F}{m} \times \frac{6 B_y}{L^2},
\end{aligned} \tag{2.19}
$$

where $B_{0,x} = \frac{\mu_0 I z_0}{2\pi(z_0^2 + L^2)}$ is the field at the trap bottom (called the Ioffe-Pritchard field).

In the case of the U-wire configurations we can see that the contributions from the legs cancel and the remaining field is that of a 3-dimensional quadrupole. In our experiment,
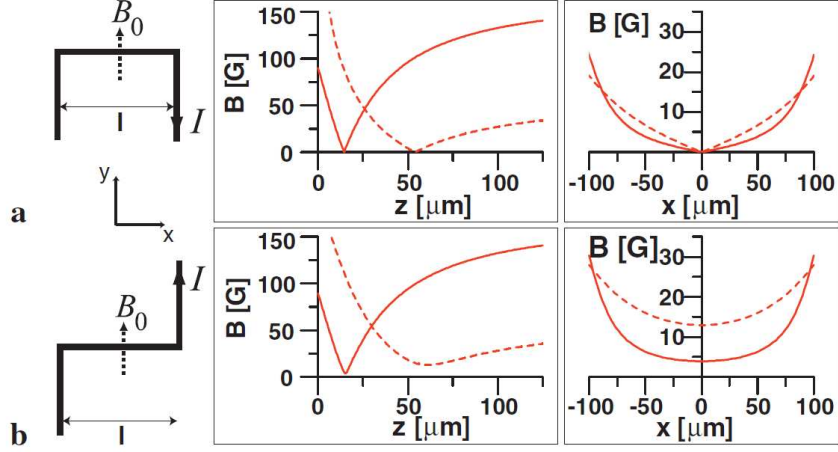
Figure 2-7: U- and Z-wire configurations and their corresponding magnetic fields. As the temperature of the trapped atoms is reduced, the U-wire configuration is no longer adequate for trapping. As slow atoms spend an increasing amount of time in a region with zero magnetic field, the probability to undergo a spin flip (Majorana spin flip) followed by a removal from the trap is no longer a negligible process. The solution to this problem is to incorporate a Z-wire type trap which has the crucial feature of allowing a non-zero minimum in the magnetic field. Majorana spin flips can then be reduced to negligible levels by setting the magnetic field minimum at approx. 1 G. Taken from [47].

we employ a combination of U- and Z-traps in order to generate the U-MOT and magnetic trap respectively. By such methods, a twelve orders of magnitude increase in phase space density (relative to room temperature and density) can be achieved by means of evaporative cooling, which is the topic of the next section.

2.8 Evaporative cooling

In order to reach the required phase space density of 2.6 [48], a further increase of 6 orders of magnitude is needed beyond what is provided by typical laser cooling. To achieve this goal we load the atoms into the Ioffe-Pritchard trap described in the previous section and exploit the inhomogeneity of the magnetic field. Following a suggestion first made by Pritchard [49] and later applied by Davis et al. [50] this variation permits the use of RF transitions to selectively excite atoms that are in a region of relatively higher field, and flip their magnetic moment to a non-trappable state, thus ejecting them from the trap. Since atoms in high field regions carry a larger than average energy (i.e., they are far from the trap minimum), their removal, followed by re-thermalization of the remaining atoms through collisions, will lower the ensemble temperature. According to Eqn. 2.8 the energy difference between two

adjacent Zeeman levels ($\Delta m_F = \pm 1$) is given by:

$$\Delta U_{\Delta m_F = \pm 1} = h\nu_{RF} = g_F \mu_B B. \tag{2.20}$$

Our cooling ground state is $|F = 2, m_F = 2 >$ where $g_F = 1/2$ and we get a splitting of $0.7\,\text{MHz/G}$ between the different levels. Applying a radio pulse with a frequency ν_{RF} will cause a transition to the $|F = 2, m_F = 1 >$ state, followed by another absorption which leads to the non-trappable $|F = 2, m_F = 0 >$ state and the desired ejection from the trap. While in the $|F = 2, m_F = 1 >$ state, the atoms are still trappable and could oscillate back to a low field region where they interact with other cold atoms in a spin exchange collision, causing additional loss from the trap. To overcome this process one needs to make sure that the spin flip rate is faster than the spin exchange time.

To find the required RF frequency we write the trapping potential in the form:

$$V_{trap} = g_F m_F \mu_B (B(r) - B_{IP}), \tag{2.21}$$

where B_{IP} is the Ioffe-Pritchard field (the field at the minimum of the Ioffe-Pritchard trap). For an applied RF field with frequency ν_{RF} we see that only atoms with energies exceeding $h(\nu_{RF} - \nu_{IP})$ will be ejected (evaporate) from the trap (where $h\nu_{IP}$ is the energy at the trap bottom). As can be seen in Fig. 2-8, atoms are distributed in the trap according to the Maxwell-Boltzmann distribution. Each atom has a mean kinetic energy of $\frac{3}{2}k_B T$ and according to the virial theorem he then spends most of his time in regions of space with comparable potential energy (magnetic in nature) [2]. The RF signal (also known as "RF knife") is kept at a constant energy above this most probable value $h\nu_{RF} = \eta k_B T$ where we have introduced a semi-empirical factor η to be optimized in the evaporative cooling procedure. The amplitude of the RF signal is chosen so that the broadening of the signal is small compared to the frequency, $\Delta\nu \ll \nu_{RF}$. Thus the RF radiation expels those atoms that are significantly hotter than the average in the trap.

RF induced evaporative cooling has several advantages over other methods (such as changing the trap depth adiabatically or optical excitation). For once, the trap depth can be changed continuously without affecting the trap confinement (and thus density) and

---

[2]According to the equipartition and virial theorems a particle has a mean energy of $3/2k_B T$ for both the kinetic and potential contributions
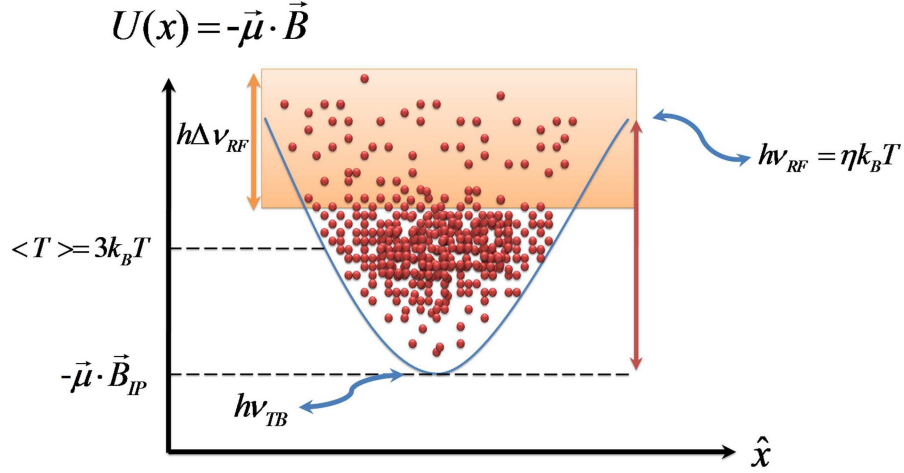
$$U(x) = -\vec{\mu} \cdot \vec{B}$$

Figure 2-8: Illustration of the RF cooling mechanism. The mean energy (kinetic + potential) of a trapped atom is $3k_BT$. The RF knife is kept at a constant ratio above the thermal average (ηk_BT) thus expelling atoms with above average kinetic energy. The constant factor η is chosen to ensure "run-away" evaporative cooling [51]. The interaction of the RF pulse with an atomic transition has a width of $h\Delta\nu_{RF}$ which depends on the power of the RF signal (power broadening) and must be taken into consideration. All the excitation frequencies in RF cooling are defined relative to the trap bottom (the minimum field or energy at the minimum, denoted here by B_{IP} or $h\nu_{TB}$) so one must also be careful to have this value stable throughout the cooling process. Taken from [40].

so the evaporation mechanism becomes largely independent of the trap shape. This fact allows working with dense samples which increases collisions and facilitates thermalization. Also, since the radiation penetrates all of the condensate, however dense (unlike methods employing optical evaporation where high optical density reduces the radiation intensity), the interaction is 3-dimensional in momentum space and thus highly efficient [51]. From a technological standpoint, RF pulses can be generated with very high precision, allowing accurate control and characterization of the cooling process.

The main limitation of such a method is in the loss of a large fraction of the sample. This could be understood by thinking of an extreme example. In principle, one can raise the trap depth to a value comparable with the total energy possessed by all the atoms in the trap. One then only needs to wait until one atom will have all of the energy of the system and subsequently escape from the trap, leaving the remaining atoms at zero temperature. Unfortunately, due to the exponential form of the Second Law of Thermodynamics, such events are extremely rare and the experimenter will have to wait a practically infinite amount of time for the process to occur. Although discouraging, this gedanken experiment demonstrates that evaporative cooling is a compromise between efficiency and cooling speed.

What sets the timescales for the method are the unavoidable loss rates which will eventually deplete the sample.

Good collisions, bad collisions, and rate equations

The depletion and thermalization of the sample are determined by atomic collision rates which set the timescale of the whole evaporation process. On the one hand, the rate of elastic collisions determines the thermalization time, and thus the rate at which the RF knife can be lowered. On the other hand, the rate of inelastic collisions (with background gases or other relaxation/recombination processes within the trap) determines the sample's lifetime which subsequently determines the time available for the evaporation process. For alkali atoms the main loss channel is background collisions. Spin flipping 2-body collisions and molecule forming 3-body collisions are present at higher densities. Background gas collisions have no energy dependence and so they remove atoms with an average energy from the trap, while the other two types are density dependent and since the density is highest for low energy atoms (near the trap minima) it predominantly removes atoms with lower than average energy from the trap, thus increasing the average energy.

For this reason evaporative cooling requires a favorable ratio of elastic to inelastic collisions, defined as $R = \tau_{loss}/\tau_{el}$, where τ_{loss} and τ_{el} stand for the mean free time between collisions. As atoms evaporate from the trap the phase space density increases but so do the loss rates; in order to maintain an accelerating collision rate ("runaway evaporation") we require that the evaporation begins with an R value larger than a certain minimum: $R > R_{min}$. Since elastic collisions are density dependent unlike background gas collisions a compression of the trap is employed prior to evaporation in order to increase the R ratio. In conclusion, the requirements to reach a BEC using RF evaporation involve:

1. A vacuum on the order of 10^{-11} Torr (ultra-high vacuum region) to suppress background collisions;

2. A minimum initial phase space density combined with a sustainable collision rate ratio R in order to be in the runaway regime;

3. Maintaining the RF knife at a constant multiple η of the temperature during the evaporation;

4. Adiabatically compressing the sample prior to evaporation to increase the good to bad collision ratio.

2.9 Theory of a BEC in a harmonic potential

The Gross-Pitaevskii (GP) equation for the multi-particle wavefunction $\Psi_0(r) = \sqrt{N_0}\phi_0(r)$ (where $\psi_0(r)$ is the single particle wavefunction and N_0 the number of atoms) is given by:

$$\left(-\frac{\hbar^2 \nabla^2}{2m} + V_{ext}(\boldsymbol{r}) + g|\boldsymbol{\Psi}_0(\boldsymbol{r})|^2 \right) \boldsymbol{\Psi}_0(\boldsymbol{r}) = \mu \Psi_0(\boldsymbol{r}), \quad (2.22)$$

where the quantity μ is the chemical potential which is fixed by the condition that there are N atoms in total, $N = \int |\Psi_0|^2 dr$, and where we have used a formulation in terms of an effective potential which when expressed in terms of the s-wave scattering length a, has the form:

$$g = \frac{4\pi\hbar^2 a}{m}. \quad (2.23)$$

The balance between the kinetic and interaction energy terms fixes a typical distance over which the condensate wave function can heal, this length scale is given by:

$$\xi = \sqrt{\frac{\hbar^2}{2mgn}} \quad (2.24)$$

where n is the sample density.

This length scale, termed the healing length, separates solutions of the GP equation into 2 classes.

For small values of ξ we can neglect the kinetic term and write the equation as:

$$\left(V_{ext} + g|\boldsymbol{\Psi}_0(\boldsymbol{r})|^2 \right) \boldsymbol{\Psi}_0(\boldsymbol{r}) = \mu \Psi_0(\boldsymbol{r}), \quad (2.25)$$

which is the useful Thomas-Fermi (TF) approximation. The solution of this equation gives:

$$|\Psi(r)_{TF}|^2 = n_{TF}(r) = \frac{\mu - V_{ext}}{g}. \quad (2.26)$$

On the other hand, for large values of ξ we can neglect the interaction term and write:

$$\left(-\frac{\hbar^2 \nabla^2}{2m} + V_{ext} \right) \mathbf{\Psi}_0(\boldsymbol{r}) = \mu \Psi_0(\boldsymbol{r}), \tag{2.27}$$

which can be solved either analytically or numerically, depending on the form of the trapping potential. Intermediate values of ξ are of course also possible, for which numerical methods are usually employed.

In the case of trapping in a harmonic potential (such as generated by the magnetic trap near its minimum) the external potential is given by:

$$V_{ext}(r) = \frac{m}{2}(\omega_x^2 x^2 + \omega_y^2 y^2 + \omega_z^2 z^2), \tag{2.28}$$

where ω_i is the trapping frequency in the ith direction. The ground state of an oscillator in the large ξ limit can be solved by a Gaussian form:

$$\Psi_{Gauss}(\boldsymbol{r}) = (\frac{m\omega_{ho}}{\pi\hbar})^{3/4} exp(-\frac{m}{2\hbar}(\omega_x x^2 + \omega_y y^2 + \omega_z z^2)), \tag{2.29}$$

where we have defined $\omega_{ho} = (\omega_x \omega_y \omega_z)^{1/3}$, and took as the chemical potential the energy of the ground state $\mu = \epsilon_0 = \frac{\hbar}{2}(\omega_x + \omega_y + \omega_z)$ The normalization condition on all solutions is:

$$\int \Psi(\boldsymbol{r})^* \Psi(\boldsymbol{r}) dr = N; \qquad\qquad n(r) = N|\Psi|^2 \tag{2.30}$$

The parameter ξ has dimensions of length; in order to have an absolute meaning to its scale we need another length dimension against which we can compare it. Since we are trapping atoms in harmonic traps the natural length scale in our situation is the oscillator amplitude ($\frac{1}{2}m\omega_i^2 a_i^2 = \frac{\hbar}{2}\omega_i$). Comparing ξ to a_i gives us:

$$\frac{\xi}{a_i} = \frac{\sqrt{\frac{\hbar^2}{2mgn}}}{\sqrt{\frac{\hbar}{m\omega_i}}} = \sqrt{\frac{\frac{1}{2}\hbar\omega_i}{gn}} \tag{2.31}$$

When the interaction term is larger than the oscillator energy, ξ is small compared to the size of the trap and a Thomas-Fermi approximation is adequate. In the opposite limit, if the oscillator energy is larger than the interaction term, interactions can be neglected, ξ is larger than the trap and we are back to the ideal gas solution with a Gaussian form. We see that the healing length can be small or large compared to the harmonic oscillator length at

each direction, and at times we can have solutions which resemble a TF form on one axis and a Gaussian form on another.

As we will later see, in our experimental setup we encounter harmonic traps which have very tight confinements only in 2 of the 3 axes. Such anisotropic traps display density profiles similar to the TF solution for the low frequency axis while simultaneously having a Gaussian profile for the high frequency ones. In the case where the tightly confined axis gives very large values of ξ relative to the oscillator length on that axis, the condensate cannot be excited beyond the lowest lying vibrational state (higher states are said to be "frozen") and the condensate is said to be in a one dimensional trap.

Chapter 3

Experimental Setup

Experimental systems of trapped neutral atoms allow scientists a unique opportunity to study atomic physics as well as many-body physics. For this to be possible the atoms must be isolated from the environment by confining them with, for example, magnetic fields as discussed in Sec. 2.4. This isolation must last long enough for the experimenter to prepare, manipulate and measure the quantum state as desired (e.g. the state of the internal and external degrees of freedom of the atoms). Amongst the experimental restrictions imposed by these requirements is that the density of background gas must be kept sufficiently low in the volume where the actual experiment takes place; background gas particles would otherwise collide with the cold atoms and eject them from the shallow magnetic trap. In particular, RF evaporative cooling (the method of cooling commonly used for reaching a BEC) depends on suppressing such background (inelastic) collisions sufficiently that elastic re-thermalization occurs within the cold gas to generate the BEC (see Sec. 2.8), with enough time remaining for experimentation. This generally requires a vacuum on the order of 10^{-11} Torr. Into this vacuum setting one then needs to introduce all the standard laser cooling schemes (involving precisely aligned laser beams and magnetic fields), then to control the various fields, and finally to image and analyze the atomic cloud. The operation of such an apparatus is the topic of this chapter which will include a discussion of all the relevant subsystems.

3.1 Vacuum system

In order to reach vacuum levels on the order of 10^{-11} Torr we use the vacuum system depicted in Fig. 3-1. The chamber is made from 316LN non-magnetic stainless steel and incorporates large-diameter tubing to allow high conductance for the ion pump. The complete system is built around a 6-way cross to which the pumps, a smaller chamber and the Atom-Chip mount are connected. The smaller chamber, an octagon (73 mm high, 200 mm wide), is where the experiment takes place and is thus termed the "science chamber". Seven of the access ports on the science chamber have optical-grade windows (anti-reflection coated for 780 nm radiation); the eighth port has an atom vapor dispenser. The atom vapor dispenser (SAES Getters Rb/NF/3.4/12) acts as our atom source by releasing rubidium into the chamber after heating with around 16 A of current at the beginning of each experimental cycle. In addition to the dispenser, we use an array of ten UV LEDs positioned around the chamber; the light-induced atom desorption (LIAD) effect causes rubidium atoms to desorb from the vacuum chamber walls [52]. Releasing atoms from the surface allows us to use lower current for the dispenser while generating the same number of gas atoms, thus recycling rubidium and helping to reduce the overall pressure.
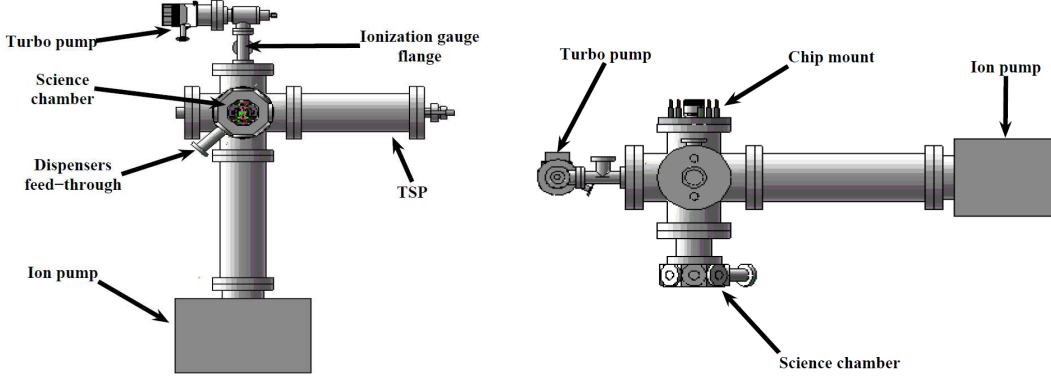

Figure 3-1: Vacuum System. Top view on the left and front view on the right of the vacuum system used in our setup. Adapted from [40]

The vacuum system incorporates four types of pumps, a dry scroll pump, a turbo pump, an ion pump and a titanium sublimation pump (TSP). Initially, a dry scroll pump (Varian SH-100) evacuates the chamber to low pressure (10^{-2} Torr) to allow the turbo pump (Varian TV70LP, 70 l/s) connected to it in series to start working (since turbo pumps cannot start from atmospheric pressure). This initial pump-down brings the chamber to high vacuum

levels (10^{-8} Torr). To achieve ultrahigh vacuum ($< 10^{-10}$ Torr) needed for our experiments, it is then necessary to implement a baking procedure [53] to extract water vapor stuck to the chamber's walls that would otherwise provide an almost infinite source of gas. We use a relatively low baking temperature of $150°$C to avoid damaging the AtomChip, since gold can diffuse at high temperature. We generally bake the system for 5-7 days even though the chamber is flushed with nitrogen when opening it for maintenance. The ion pump (Varian Vac-ion, 300 l/s) is started during the baking procedure and is kept on permanently. When the gas load due to baking has declined sufficiently, the turbo pump is separated from the chamber using a UHV valve (VAT all-metal UHV angle valve - series 54). Occasionally we run the TSP in order to further reduce the pressure, but this operation tends to cause instabilities in the experiment and is not applied frequently. These four pumps, together with the science chamber and the AtomChip mount, occupy 5 ports of the 6-way cross (see Fig. 3-1). The ion pump is kept at a distance from the science chamber so that the magnetic field utilized by the pump will not interfere with the experiment. This is done by placing a 500 mm-long tube between the pump and the science chamber where the atomic cloud is located.

In order to measure the pressure we use a nude ionization gauge (Varian UHV-24p) between the valve connecting the turbo pump and the 6-way cross. The rated low-pressure limit of this gauge is $5 \cdot 10^{-11}$ Torr, although we achieve a magnetic trap lifetime on the order of 60 s, indicating an effective background pressure on the order of 10^{-12} Torr. Thus the actual pressure is usually below the nude ion gauge limit, which is therefore used only during pump-down and bakeout.

3.2 Laser light

In our experimental system we use four different laser frequencies in order to induce the required atomic transitions (see Fig. 2-1 and Sec .2.3).

1. Cooling - $|F = 2 > \rightarrow |F' = 3 >$, red-detuned by 16 MHz, σ^+ polarization, power delivered to the experiment of around 90 mW;

2. Repumping - $|F = 1 > \rightarrow |F' = 2 >$, on resonance, σ^+ polarization, power ≈ 10 mW;

3. Imaging - $|F = 2 > \rightarrow |F' = 3 >$, on resonance, linear polarization, power of few μW;

4. Optical pumping - $|F = 2 > \rightarrow |F' = 2 >$, on resonance, σ^+ polarization, power of few

μW.

In order to generate these four frequencies we use two lasers and shift their frequencies using acousto-optical modulators (AOM's). The AOM's are also used as fast shutters and to adjust the cooler and repumper frequencies in real time during the MOT and optical molasses stages (the former aiming at the Doppler limit and the latter at the recoil limit by shutting down the magnetic fields and further detuning the lasers), all of which are controlled by the computer. Noting that three of the required laser transitions originate from the $|F = 2 >$ state, while one originates from the $|F = 1 >$ state, the resulting frequency spacing between the repumper and the other beams (6.835 GHz) is too large to be obtained using standard high-efficiency AOM's (capable of shifting frequencies by only a few hundred MHz).

The first laser, a TA100 unit from Toptica (utilizing a master-slave tapered amplifier architecture), generates up to 1 W of power at 780 nm and is split into the cooling, imaging, and optical pumping beams. A second laser, a DL100 unit also from Toptica, has an output power of 80 mW and is used only for the repumper beam. The TA100 is locked using a Pound-Drever-Hall detector (PDD) with a 20 MHz current modulation around the $1 - 3$ crossover peak of ^{87}Rb which is then fed back into the Toptica PID regulator. The spectroscopy peak is obtained by a saturated absorption spectroscopy technique. The repumper laser is locked using the Toptica PID regulator directly locked to the $1 - 2$ crossover peak obtained again from a saturated absorption spectroscopy signal. Both spectroscopy setups supply us with Doppler-free spectroscopy signals for the various locking mechanisms. The lasers and their respective spectroscopy optics are located on a separate breadboard sitting on the optical table for increased stability, and are enclosed in a box to reduce air currents and acoustic vibrations. The table itself sits on standard pneumatic legs to reduce vibrations.

Optical layout

The optical layout in our setup is illustrated in Fig. 3-2. The cooler beam is shifted by 196 MHz to be near-resonant with the $|F = 2 > \rightarrow |F' = 3 >$ cooling transition (212 MHz detuning is on resonance) by going through the AOM twice in a double-pass configuration. The imaging beam is detuned by 212 MHz to be on resonance with the cooling transition.

The optical pumping beam is tuned to be on resonance with the $|F = 2 > \to |F' = 2 >$ transition by passing once through the AOM and shifting the frequency to the red of the crossover by $50\,\mathrm{MHz}$. The repumper beam is tuned on resonance with the $|F = 1 > \to |F' = 2 >$ transition, $80\,\mathrm{MHz}$ detuned from the lock point of the DL100 laser, by a single pass through the AOM.
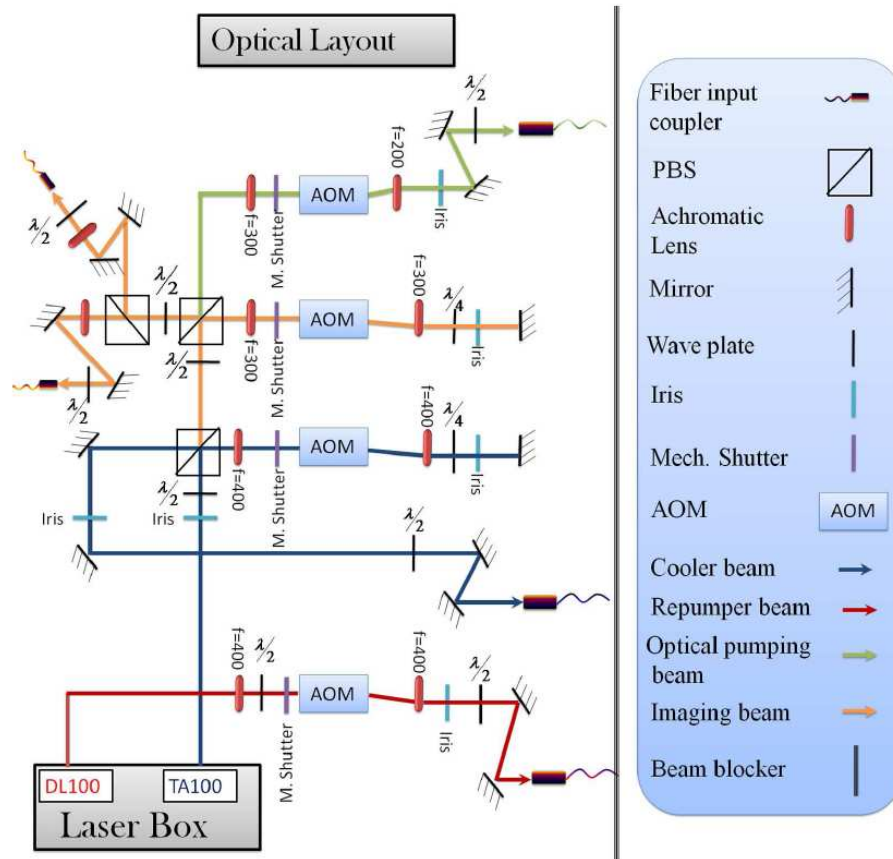

Figure 3-2: Optical layout. The TA100 and DL100 main beams are split into four beams and each one is shifted individually by an AOM. The imaging beam is further split into two for the separate imaging axes. These five laser beams are then injected into five fibers for greater stability and spatial filtering; the fiber outputs are then fed into the science chamber. Taken from [40].

Shutting off the AOM's causes the laser beam to be blocked and the AOMs are thus used also as fast shutters (ns time scale). However, the AOM's allow some light to leak through even when shut, so we trigger mechanical shutters (Uniblitz) shortly after the AOM's in order to completely block the residual light. All four laser beams are coupled into polarization-maintaining fibers for more convenient transmission to the science chamber, to improve beam quality (the emerging beam is Gaussian), and to reduce stray light entering

39

the science chamber.

The cooler and repumper beams are superimposed using a polarizing beam splitter (re-combiner) and then split into the four counter-propagating MOT beams, each of which passes through a $\lambda/4$ waveplate to change the light polarization to σ^+ (in the photon frame) immediately before entering the science chamber.

The optical pumping beam and the main imaging beam are inserted into the science chamber along the $\hat{y}$-axis. For imaging atoms very close to the AtomChip surface ($h < 50\,\mu$m) we tilt both the imaging beam and the camera by about 5°, so that the beam reflects off the AtomChip; the resulting mirror images then directly give the distance of the atoms from the chip surface (see [54] for more details).

An additional imaging beam is injected parallel to the plane of the AtomChip at a 45°-angle to the $\hat{y}$-axis; its optics provide smaller magnification in order to image larger clouds (in the MOT and magnetic trap stages) further from the AtomChip. A third imaging beam incorporates a setup along the $\hat{z}$-axis using a periscope system with the AtomChip acting as a mirror in order to image the atoms from below (more on this in Sec. 5). Three cameras are positioned opposite each imaging beam's entrance ports and are triggered to take an absorption image of the cloud at the desired time.

Figure 3-3 shows the layout of the various laser beams positioned around the science chamber.

3.3   Magnetic fields

3.3.1   Coarse magnetic fields

We construct magnetic traps by combining homogeneous ("bias") and inhomogeneous fields. In order to generate bias magnetic fields, our system incorporates three pairs of coils oriented along the three orthogonal axes, and a fourth pair oriented along the $\hat{x}$-axis but allowing opposite current polarity for conveniently reversing the direction of the field along this axis. All four coils are centered around the science chamber. For the main x- and the y-coils, we use two identical pairs of square coils separated by 285 mm, with inner dimensions of 110 mm. The coils are constructed from 25 turns of 25 mm^2 cross section copper wire, resulting in outer dimensions of 200 mm. Each pair of coils has a resistance of 70 Ω and an inductance of 0.56 mH, and generates a measured field of 0.54 G/A at the center of the
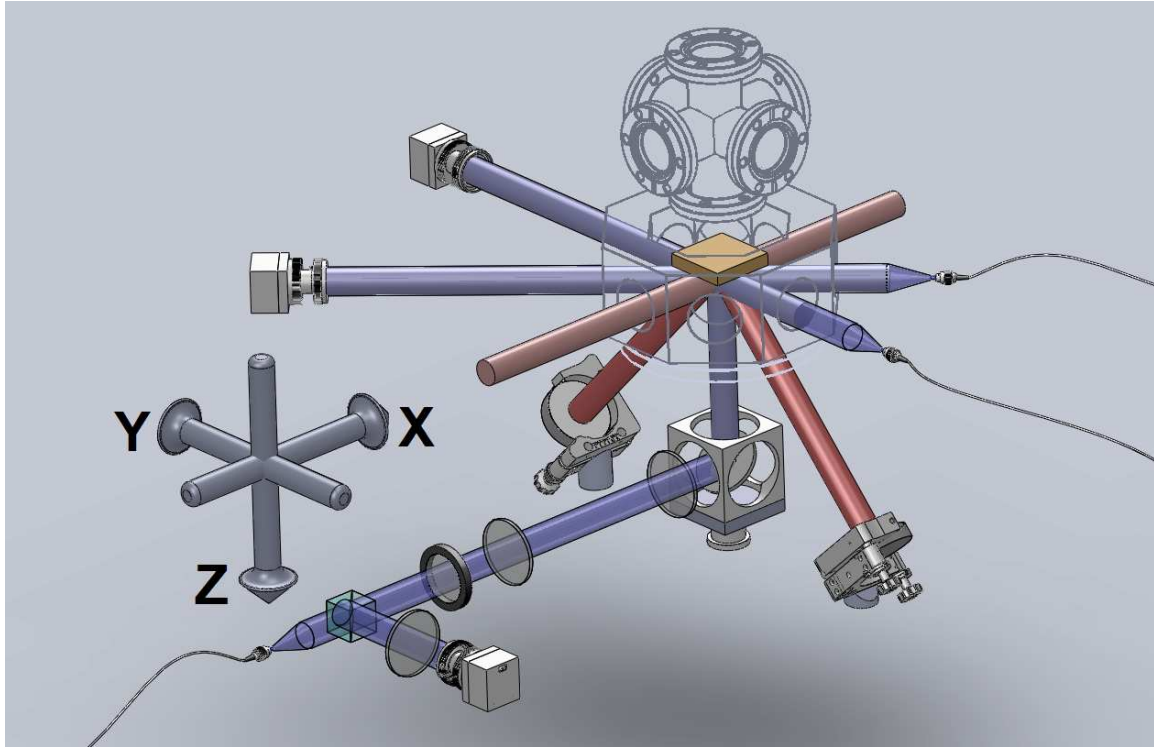
Figure 3-3: Science chamber layout. Blue rods represent the imaging beams while the red ones are the cooler/repumper beams. The cooler/repumper beams show only the last segments prior to entering into the chamber.

science chamber with good uniformity within the central few cubic cm of the chamber.

The z coils are made from 20 turns of the same wire but have a circular shape with an inner and outer diameter of 220 and 283 mm respectively. Their separation is only 85 mm, resulting in a stronger measured field of 1.54 G/A at the center of the science chamber.

In addition to these bias fields, we create inhomogeneous fields for trapping by pushing current through various elements (such as the U- and Z-wire) discussed previously (see Sec. 2.4). The wire elements are embedded in the AtomChip mount (see Fig. 3-4), which is inserted into the 6-way cross from above (Fig. 3-1) and brings the AtomChip through the cross all the way down to the center of the science chamber.

As seen in Fig. 3-5 we have built a set of copper wire elements, supported and aligned by a macor structure. These four elements are the U-wire (for the MOT quadrupole field), the Z-wire (for the Ioffe-Pritchard magnetic trap), and two "legs" that allow us to add further confinement to the magnetic trap. These thick copper wires are responsible for generating the required inhomogeneous magnetic fields used for trapping atoms before transferring to

Figure 3-4: The AtomChip mount.

the AtomChip magnetic potentials. The wires are connected to Cu leads (10 mm diameter for the Z-wire, 6 mm diameter for the other three wires) going upwards from the macor block to feedthroughs in the 160CF flange. Four stainless steel rods welded to the flange support the entire AtomChip structure mechanically (Fig. 3-4). The diameter of the Z-wire leads was increased from 6 mm to 10 mm since the smaller diameter caused unexpectedly large thermal expansion of the Cu leads. The expansion of the new mount leads has been reduced to 250 μm, which was measured by running the experimental cycle with maximum currents for a period of 24 hr. Insulation between the U- and Z-wires is ensured by a small piece of Kapton tape positioned between the pieces.

In addition to homogeneous and inhomogeneous fields, fast switching times are required for the various stages of the experiment. The current supplies we use (Agilent) allow switching times no faster than a few tens of ms; such slow shutting times would result in giving atoms a "kick" during the trap release stage and must be shortened. In order to reduce this time we have built current shutters capable of shutting down the currents in $10 - 200 \, \mu$s, depending on the amount of current initially passing through them and limited by the coil's inductance.
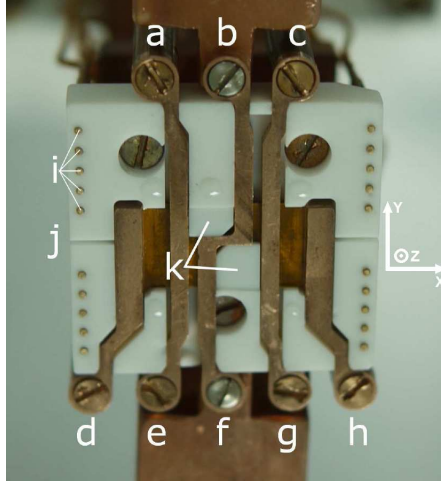
Figure 3-5: The macor piece and copper structures. 1. U-wire - Current is passed from (d) to (h); the central portion is covered with a thin layer of Kapton tape to ensure electrical insulation. 2. Z-wire - Current is passed from (f) to (b); in combination with a bias field along the $\hat{y}$-axis this creates a Ioffe-Pritchard magnetic trap. 3. Leg wires - current is passed in series from (e) to (a) for the left leg and from (g) to (c) for the right one, allowing an additional inhomogeneous field for changing confinement along the $\hat{x}$-axis. 4. There are twenty CuBe pins (i) positioned along the sides of the macor piece for bonding to the AtomChip. 5. Notches for aligning the AtomChip are machined on both sides of the macor piece (j). 6. Two additional macor pieces (k) are positioned to restrain the movement of the Z-wire along the $\hat{y}$-axis.

3.3.2   Fine magnetic fields - the AtomChip

Alongside the AtomChip lab at Ben-Gurion University of the Negev (BGU), a fabrication facility dedicated to the atom optics community was established under the name of The Weiss Family Nano-Fabrication Center. Our AtomChips (the current version, BGU1, is the second) are fabricated by depositing a single Au layer on top of a Si wafer using standard lithographic techniques borrowed from the microelectronics industry. The Si wafer is a good heat conductor (important for heat dissipation from the current carrying elements), but is not a perfect electrical insulator. We therefore use substrates with a thin layer of SiO_2 onto which we evaporate a thin layer of Ti to improve the adhesion of Au. The Au layer is $0.5\,\mu$m thick, a value which enables on the one hand a large enough current to be pushed through and on the other a decreased amount of thermally activated (Johnson) noise, but this will not be elaborated upon here. Gold is selected for its low electrical resistivity ($\rho_{Au} = 2.21 \times 10^{-8}\,\Omega$m) and high infrared reflectivity (reflectance at $45°$ incidence is $> 95\,\%$ at $780\,$nm). We also note that the thinner the wire, the higher the current density which

may be pushed through before heating causes damage. In the following we elaborate on this point.

A wire of thickness t and surface area A will generate Ohmic heating as given by

$$P_{heating} = tAJ^2\rho(1 + \alpha\Delta T), \tag{3.1}$$

where ρ is the resistivity of gold, J the current density pushed through the wire, and the power $P_{heating}$ is given in Watts. We have used the temperature coefficient ($\alpha = 0.0037\,\mathrm{K}^{-1}$ for gold) to account for the variations in resistivity at different temperatures. Also, the heat conducted to the substrate is given by Fourier's law:

$$P_{dissipation} = \kappa A\Delta T, \tag{3.2}$$

where κ is the thermal conductivity per unit length of gold ($\kappa = 4 \times 10^6\,\mathrm{Wm}^{-2}/\mathrm{K}$) and ΔT the temperature gradient between the current-carrying gold element and the substrate. The maximum temperature increase we allow for safe operation is approximately $50\,\%$ of the base temperature [55] (which in our case is taken to be $270\,\mathrm{K}$), giving $\Delta T_{\max} = 135°\mathrm{C}$. This results in a maximum current density of

$$J_{max} = \sqrt{\frac{\kappa\Delta T_{max}}{t\rho(1 + \alpha\Delta T_{max})}}. \tag{3.3}$$

We see that thinner wires allow larger current densities. A lower bound may be given by the need for a large absolute current. In addition, if one does not utilize a mirror layer, the lower bound is given by the requirement that the reflectivity of the surface will not deteriorate. We have chosen a value of $0.5\,\mu\mathrm{m}$ for the thickness, providing us with a good reflective surface, twice the current density and half the total current that was available in the old, $2\,\mu\mathrm{m}$ thick BGU0 version. Plugging in the various constants we get a maximum current density of $J_{max} = 1.72 \times 10^7\,\mathrm{A/cm}^2$, resulting in a maximum current of approx. $0.7\,\mathrm{A}$ for the $8\,\mu\mathrm{m}$-wide snake wire and $8.6\,\mathrm{A}$ for the $100\,\mu\mathrm{m}$-wide loading wires (more on these wires in the following section). Our AtomChip design is the first BGU chip to employ a two-chip architecture, placing some of the microstructures on a lower chip and thus allowing for geometries which are otherwise impossible unless one utilizes multi-layer techniques which are complex (more on the chip in the next section). The two individual chips (each

300 μm thick) composing the composite BGU1 AtomChip are glued to one another using a UHV-compatible epoxy (Epotek ND353). The composite chip is then glued to the macor; the UHV epoxy also has good thermal conductivity and allows heat to dissipate from the chip through the rest of the mount.

BGU1 AtomChip wires

Here we discuss the various wire elements incorporated into our latest double-layered Atom-Chip, which we have called BGU1. On the top chip we deposited three separate Z-wires side-by-side. Using the outer two $100\,\mu$m-wide wires in series (co-propagating currents) when the atoms are relatively far from the chip effectively generates a Ioffe-Pritchard trap corresponding to a single $200\,\mu$m-wide wire. These wires are used for conveying atoms from the initial magnetic trap (generated by the copper Z-wire) to the inner $8\,\mu$m-wide experimental wire, and they are called our "loading" wires. As shown in Fig. 3-6 the edges of the central Z-wire have sinusoidal modulation, and the wire is thus termed the "snake" wire. This modulation is the main ingredient in our experimental setup aiming at measuring quantum interference effects. A more detailed discussion of this wire is presented in Chapter 4. For now it is sufficient to state that the final goal of the experiment is to trap atomic clouds using the snake wire and several bias fields at a height of approx. $5\,\mu$m above the AtomChip.

The double-layered BGU1 chip has several advantages over our previous single-layer chip. Firstly, the magnetic traps for loading and experimentation are located at the same (x, y)-co-ordinates since their centers are in the same position. This reduces the need for bias fields along the $\hat{z}$-axis which can cause the potential to tilt towards the chip surface, thus losing atoms especially at small trap distances. Similarly, we have improved the chip alignment with respect to the copper Z-wire by using alignment marks and by physically restraining motion of the copper Z-wire along the $\hat{y}$-axis. Also, our new bottom imaging allows us to directly measure the cloud position in the $x - y$-plane and ensure that it is located directly above the desired wire (see Chapter 5). This could be done only indirectly before implementing the bottom imaging, and was very difficult to achieve with BGU0 since its wires were not properly aligned with respect to each other, nor to the copper Z-wire.

Magnetic field simulations show that transferring atoms from the copper Z-wire trap to the snake wire trap can be accomplished by a two-step loading scheme, first ramping up the

current in the $100 \, \mu$m loading wires (while lowering the copper Z-wire current) and then by ramping down the loading wire current while turning on the snake wire. We have already accomplished the first step of this procedure and, as hoped, we have found it to be much easier than with the BGU0 chip.

The three wires of the upper chip comprise the main components required for our experiment, while the ancillary wires are positioned on the lower chip. The ancillary wires which are rotated by 90 degree relative to the main wires, enable stronger confinement along the x-axis as the atom cloud is brought closer to the surface. In addition, moving wires from the top surface to a second (lower) surface gives rise to less diffraction of light which, in the previous chip, compromised the signal-to-noise in the reflected imaging detection.
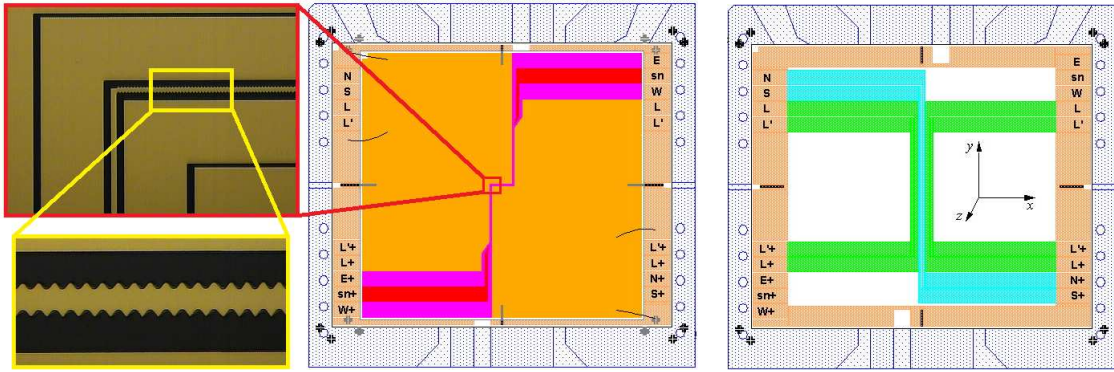

Figure 3-6: The two-layered BGU1 AtomChip. On the left is a photomicrograph of the upper chip, showing the snake wire enclosed by the two $100 \, \mu$m-wide loading wires. The width of the snake wire is $8 \, \mu$m and the period of its edge modulation is $5 \, \mu$m. Note that the edge modulation of $2 \, \mu$m amplitude is assymetric. The gold layer is $0.5 \, \mu$m thick. The middle and right frames show schematic drawings of the upper and lower chips, respectively, mounted on the macor block (light blue background). On the right a diagram of the bottom chip shows two wires (blue) designed to generate a constant $\hat{x}$-bias field at a height of $5 \, \mu$m above the chip and two pairs of wires (green, four in total) designed to add longitudinal confinement to the trap. The axes convention used throughout this work is shown on the right frame.

In the lower chip we have placed the wires shown in Fig. 3-6 on the right. The green labeled wires provide extra confinement along the longitudinal axis. There are two such pairs, both $300 \, \mu$m wide and separated by $500 \, \mu$m and $850 \, \mu$m (center of chip to center of wire) respectively. The blue wires provide an extra $\hat{x}$-bias field in the center of the trap, they are $250 \, \mu$m wide and displaced by $185 \, \mu$m from the center of the chip.

The AtomChip pads of the various wires are electrically connected to the CuBe pins positioned in the macor (see Fig. 3-5 (i)) by 10 Au bonding wires for each contact (this

overkill is done to ensure operation even in the case some wires break off). As a lesson from the BGU0 AtomChip we have moved all of the pins to the sides of the macor piece to have a clear view along the $\hat{y}$-axis, which is our main imaging axis.

3.4 Imaging setup and analysis

Our experimental setup supports imaging along several axes during any stage of the experiment. We use the technique of absorption imaging [48], whereby we trigger two consecutive $50\,\mu$s-long laser pulses (using the AOM's and the mechanical shutters), $500\,$ms apart, beginning shortly after the atoms are released from the trap. The imaging beam is tuned to be resonant with the $|F = 2 >\rightarrow |F' = 3 >$ atomic transition. The first pulse passes through the atomic cloud with a measurable fraction being absorbed by the atoms. The excited atoms re-emit light due to spontaneous emission in an isotropic process with a solid angle of 4π steradians. As long as the solid angle of the cloud seen by the first lens of the imaging system is much smaller than the full 4π, we can neglect the contribution of fluorescence altogether and treat the resulting image as a shadow of the atomic cloud. The second pulse then reaches the CCD camera without any loss since all the atoms disperse in much less than $500\,$ms.

The two images are used, together with the parameters of the atomic transition and the laser light, to determine the optical density of the atomic cloud, integrated along the imaging axis as we now discuss.

A single atom interacting with a beam of intensity I directed along the $\hat{y}$-axis will scatter light proportional to the relevant cross section. An atomic cloud characterized by a density distribution $n(x, y, z)$, will reduce the intensity of a beam traveling an infinitesimal distance dy through the cloud by

$$\Delta I = -\sigma I n(x, y, z) dy, \tag{3.4}$$

where the scattering cross section depends on the intensity of the incoming light:

$$\sigma = \frac{\sigma_0}{1 - I/I_{sat}}. \tag{3.5}$$

In the limit of low light intensity as in our work, $I \ll I_{sat}$ (where I_{sat} is the saturation

intensity) and the nonlinear term can be neglected. By integrating Eqn. 3.5 along the direction of propagation of the laser beam we get the Beer-Lambert law:

$$I(x, z) = I_0 \ \exp(-\sigma_0 \int n(x, y, z) dy) = I_0 \ \exp(-\sigma d(x, z)), \qquad (3.6)$$

where $d(x, z)$ is the column density of the cloud projected on the $\hat{y}$-axis and I_0 is the intensity of the incident beam. The product $\sigma d(x, z)$ is often referred to as the optical density (OD) of the atomic cloud.

For an $|F = 2 >\rightarrow |F' = 3 >$ transition and linearly polarized incident light[1] the cross section is $\sigma = 1.938 \times 10^{-9} \, \text{cm}^2$ for ^{87}Rb, and the saturation intensity is $I_{sat} = 2.503 \, \text{mW/cm}^2$ [39]. The intensity ratio between the two images obtained above, corresponding to I and I_0, can be calculated for each pixel in the image, from which we then obtain the column density:

$$d(x, z) = -\log(\frac{I}{I_0})/\sigma = -\log(\frac{N}{N_0})/\sigma \qquad (3.7)$$
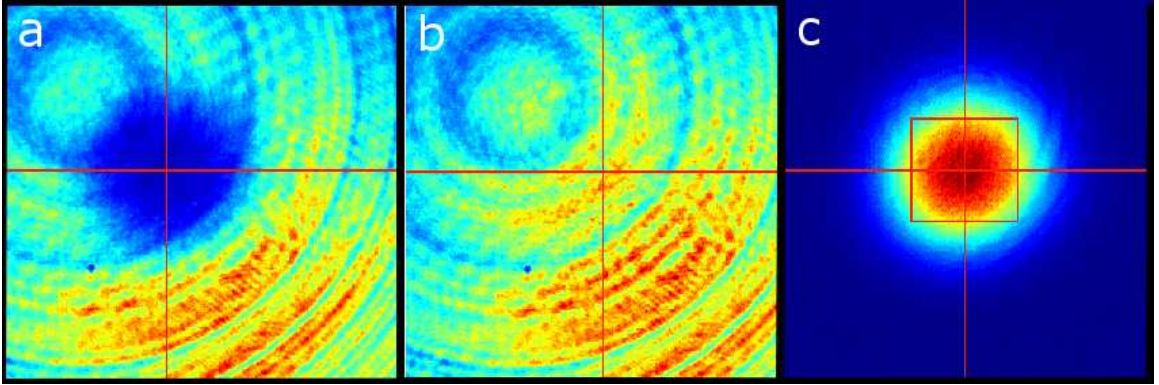
An example of this method is shown in Fig. 3-7.

Figure 3-7: Absorption imaging sequence. a) The shadow cast by the atomic cloud from the first laser pulse. b) The incident intensity I_0 is obtained by taking a second picture after the atoms have dispersed. c) An absorption image is generated pixel-by-pixel from the logarithmic ratio of these two pictures.

Imaging along the three axes is done by passing a laser beam through the relevant

---

[1] In principle the interaction with circularly polarized light is stronger (higher values of σ and lower values of I_{sat}) and will thus result in higher sensitivity, but since we are imaging near the surface of the AtomChip, only linearly polarized light can be adjusted to have the same intensity before and after reflection from the chip's mirror surface.

science chamber ports as shown in Fig. 3-3. The imaging beam along the $\hat{y}$-axis is tilted by 5° to reflect off the surface of the AtomChip. This allows us to image clouds very close to the chip surface and to measure the distance of the cloud from the chip directly. The other two imaging axes are used for imaging the cloud when its further away from the chip and for determining the cloud position relative to the AtomChip wires.

The coherent nature of laser radiation can easily cause interference patterns on the imaging plane. Interference rings such as those visible in Fig. 3-7 can be caused by multiple reflections from optical surfaces along the imaging laser beam path, or by imperfections in the optical elements themselves. In principle such interference patterns should not cause a deterioration of the absorption image; since only relative intensities are important, inhomogeneous spatial intensity distributions cancel out. However, movement due to the mechanical shutters, cooling fans or acoustic vibrations can cause the two images to be misaligned and introduces noise into the image (see Fig. 3-8). This problem is aggravated when reflecting the imaging beam from the AtomChip (for imaging atoms close to the surface). Shutting down the strong magnetic fields applies a force on the conducting elements rigidly attached to the AtomChip and moves the whole construction by a few μm.

Other noise sources also add to the noise level: Speckle patterns originating from the interference of spuriously scattered light with the imaging beam, dust particles that scatter light and noise originating from the CCD itself such as dark currents (false signals caused by thermally excited electrons), readout noise (noise originating from the reading and amplification processes involved in extracting the image from the CCD), and fluctuations due to the limited quantum efficiency of the CCD cells. We have minimized the noise level in our setup by employing various precautions. Stray light is kept out of the experiment by covering the setup with a black curtain; mechanical shutters are decoupled from the optical table by hanging them on a separate frame; and the time between the two images is shortened as much as possible to minimize the displacement of various elements due to vibrations. Taking these measures brings the noise level to an optical density of slightly below 0.1 which means that our column density detection limit is $\approx 0.5\,\mu\mathrm{m}^{-2}$. A similar setup built by our group standing right next to our optical bench is constructed more rigidly and reaches noise levels of 0.03. Noise originating from a relative movement of the two frames or other variations in the background image can also be reduced by using image processing methods [56].
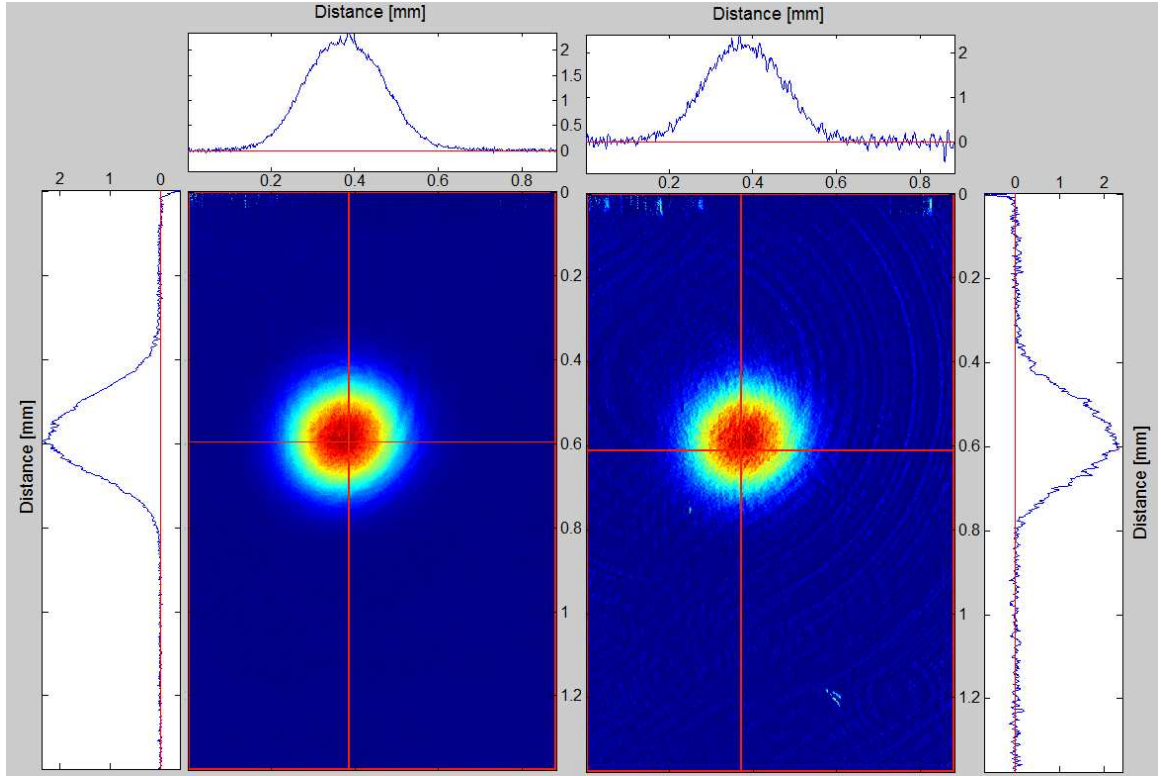
Figure 3-8: Noise due to vibration. The same absorption image as in Fig. 3-7 is shown on the left. On the right a new absorption image is generated by displacing the second picture in the absorption imaging sequence by two pixels corresponding to a movement of $3\,\mu$m on the image plane. The simulated vibration adds considerable noise to the image due to a misalignment of interference rings and other features. The increase in noise by a factor of about 5 is evident by comparing the one-dimensional cuts for the two analyses.

Given that mechanical vibration is a major source of noise in our current imaging setup, we must evaluate this noise when considering alternative imaging methods. In particular, two other methods [48, 57], which utilize spatial filters onto which the unscattered light is focused and blocked (dark-ground imaging) or phase shifted (phase-contrast imaging), require precise focusing of the beam and may therefore be even more prone to noise due to mechanical vibrations. In terms of the signal level, we have for the intensity (initially I_0) at a point in the image plane (after traversing a cloud with density n and cross section σ_0) [48]:

$$< I >= I_0\tau^2 - I_0\sigma_0\tau \left[\frac{\delta}{1+\delta^2} \sin\gamma + \frac{1}{1+\delta^2} \cos\gamma \right] n, \tag{3.8}$$

where τ^2 is the transmitted fraction, γ the phase shift and δ the detuning. All three cases are treated by this equation, absorption imaging ($\tau = 1, \gamma = 0$), dark-ground ($\tau = 0$) and

phase-contrast ($\tau = 1, \gamma = \pm\pi$) are obtained as special cases. The equation shows that the absolute maximum signal is obtained by choosing $\delta = \gamma = 0$ and $\tau = 1$ which is the case of absorption imaging. Dark-ground imaging is far from optimum and phase-contrast imaging is a factor of two lower. The only consideration left is that of sufficient dynamic range i.e., the ability of the CCD chip in the camera to adequately distinguish between the imaging beam intensity with and without atoms. In this aspect phase-contrast and dark-ground imaging might have an advantage since they map the atomic density to a signal with a lower background. In our system we utilize a digital camera (Prosilica GC2450) employing a CCD detector (Sony ICX625) with a 12-bit sampling. Since we are using the camera at around 50% of its saturation level, we have a dynamic range determined effectively by 11-bit sampling. This then allows us to distinguish between intensities (and thus optical densities) on the order of $2^{-11} \approx 10^{-3}$ which is considerably below the 0.1 noise level we observe. We conclude that dynamic range is not an issue for our detector and methods such as dark-ground or phase-contrast imaging, will not improve the signal-to-noise ratio for detected atoms (though these methods may be advantageous for other reasons, such as non-destructive imaging [58, 59]).

3.5 Experimental control

In order to control the various parameters in our setup (laser detuning, magnetic fields, pulse timing, currents, etc.) we have designed an experimental control system based on a PXI unit by National Instruments (NI). This computer-controlled unit has an independent processor along with multiple input and output ports that allows one to manage various signals on a μs time scale. The experimental sequence is controlled using a graphical user interface (GUI) programmed with Labview 8 (NI). After setting up the various parameters the user executes the experimental cycle. The sequence is then uploaded to the PXI's internal memory and commands are sent to the various devices according to the user's specification independent of any other external clock. This by-passes the PC-based clock, whose synchronization can be lost when other processes are running on the computer. The PXI also has much faster time resolution, which is necessary for several of the experimental events.

The PXI sequence also triggers the various cameras used in the experiment and the images thereby acquired are stored on a computer. The software (programmed with Mat-

lab) then processes the raw images to generate an absorption image and executes fitting algorithms that calculate the OD, cloud size, position, and other parameters of the trapped atomic cloud. In addition to this standard operation, the system can also run in a loop mode in which parameters can be scanned through a predetermined array of values without the need of human intervention for each iteration. This can be especially helpful for measuring atomic cloud temperature (by time-of-flight methods) or the lifetime of atoms in the trap. Also, an optimization mode is available, in which the imaging software analyzes the output of the experiment and determines the values of the next iteration automatically using a machine learning algorithm as will be discussed in Chapter 6. The operator then decides which parameters to optimize automatically and the criterion for their optimization (such as maximizing the atom number, positioning the cloud in a specific location, etc.), and sets their limiting values.

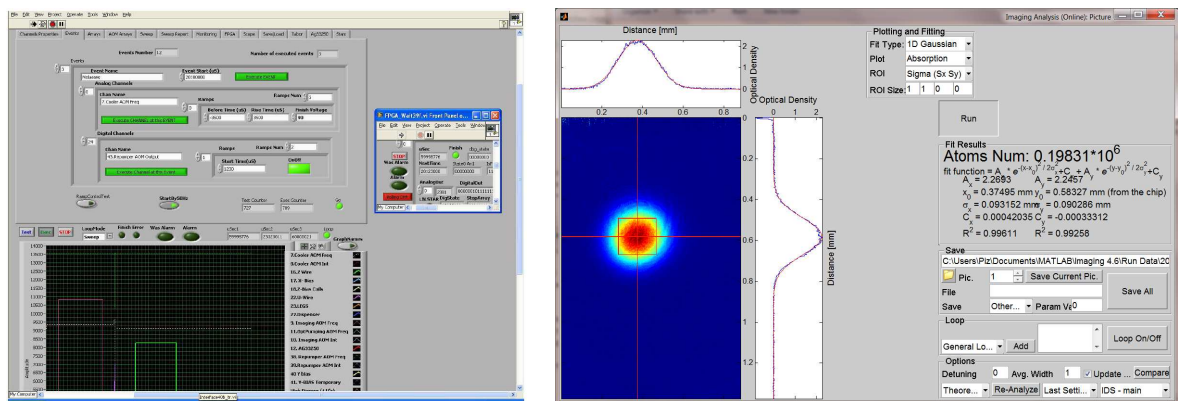Fig. 3-9 shows the various software used in our setup.

Figure 3-9: Computer interface. On the left the Labview based interface for the various channel controls, on the right the image analysis software.

Chapter 4

Gradual Release

In recent years, the use of BECs as a source of phase coherent matter waves to study basic phenomena in physics gained much popularity following exciting advances in the field. Today the generation of BECs is a standard method employed in numerous laboratories around the world and has matured into a benchmark for the study of fundamental quantum mechanical phenomena such as tunneling, insulating phases, Bloch oscillations, interferometry, coherence and breakdown of coherence just to name a few. One of the most important tools for exploring such phenomena is coherent matter trapped in periodic potentials (lattices), which is usually achieved by counter-propagating laser beams that create a standing wave, thereby generating a periodic potential for the atoms via the Stark effect. The size of these traps is determined by the wavelength of the laser field, which is usually smaller than a micrometer, resulting in a spatial separation of the clouds that render the direct imaging of the various sites very difficult. Luckily, probing these ordered configurations is made possible by imaging the interference patterns observed after the release of atoms from the trap: atoms from adjacent lattice sites interfere with their phase coherent neighbors and the interference patterns become much larger than the initial trap, rendering their observation a relatively simple task from an optical standpoint.

The implementation of periodic potentials on AtomChips, by using magnetic fields instead of optical fields, is an intriguing goal that seems to offer additional flexibility for engineering lattices [60]. The restrictions on the shape and separation of the lattice sites inherent in optical lattices are not present when the potential is generated by magnetic fields originating from wires which can be engineered to any desired shape using standard

lithographic processes. Some progress in this field was already obtained by perturbing trapped atoms using double well potentials [61, 62, 63]. Coherent evolution from two or more trapping sites by employing only static magnetic fields (as opposed to methods such as RF potentials employing varying fields) was achieved only recently [64]. However, an interference pattern from such an apparatus is yet to be observed.

In this chapter we propose an experiment in which a one-dimensional periodic potential, with many sites along its length, is created using only the static magnetic field of a single wire (see Fig. 4-1), with the aim of observing the first matter-wave interference pattern in such a configuration. One-dimensional BECs are well suited for the study of Bose-Hubbard type Hamiltonians (a theoretical tool for dealing with interacting particles in a lattice having a certain probability to tunnel to adjacent sites) [65], as well as for the study of quantum fluctuations, since the energy associated with order in one dimension is smaller than in two- and three-dimensional systems, rendering fluctuations more influential in determining the dynamics of phase transitions. Once an interference pattern is observed, we will move on to study the above topics.

We generate a periodic magnetic potential by fabricating a Z-wire whose edges are modulated periodically. We will show that this configuration allows control of the barrier height between adjacent sites. The unique features of this trap also pose some challenges concerning how to view the coherent evolution and interference pattern. As we will show, we have found that by turning off the magnetic trap gradually rather than suddenly during the trap release, we can control the expansion dynamics of the trapped clouds, thereby overcoming these problems.

4.1 The snake wire

The magnetic lattice is generated by a sinusoidal corrugation of the edges in the central wire in the Z-trap of our BGU1 AtomChip (see Fig. 3-6) and has the dimensions shown in Fig. 4-1. This potential is an example of "engineered fragmentation" allowing us to study processes originating from the splitting of BECs.

The snake wire has a sinusoidal periodicity of $5\,\mu$m and an edge modulation amplitude of approx. $2\,\mu$m. Note that the edge modulation is asymmetric [66]. In order to calculate the resulting potential [54] we have used a finite-element method (FEM Lab) to numerically
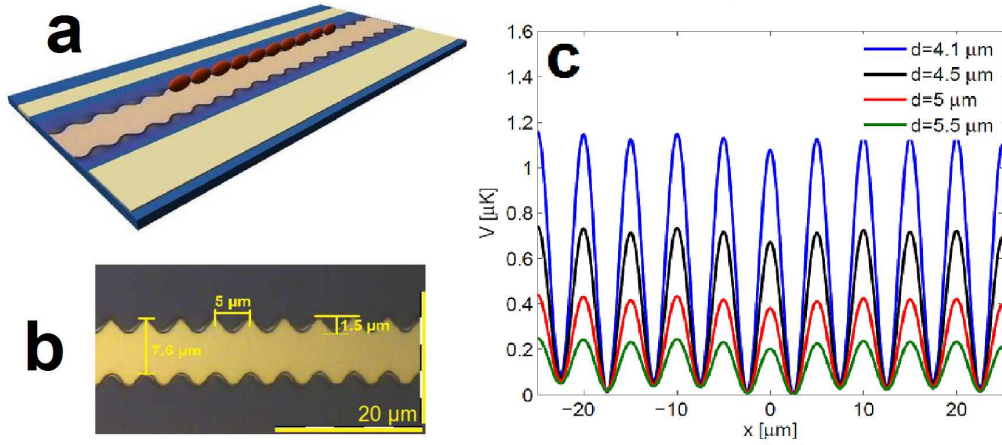
Figure 4-1: The "snake" wire middle section. (a) A BEC (shown in red) simulated at small atom surface separations $< 5\,\mu m$ is fragmented by the lattice potential. (b) A photomicrograph of the snake wire with its dimensions. (c) The potential energy (relative to the global minimum) along the minimum-energy path for a few values of the trap height d. Adapted from [54].

evaluate the current density passing through every point along the wire. The magnetic potential can then be calculated at any position and for any current. The periodicity of the wire is the source of a component in the Fourier expansion of the potential with a value of $2\pi/5\,\mu m^{-1}$. The amplitude of this component decays exponentially with distance from the chip [67], which means that at large atom-surface distances ($\gg 5\,\mu m$) the corrugation is not seen by the atoms. For this reason, potential modulation is significant only for heights of approx. $5\,\mu m$ and below, therefore requiring the atomic cloud to be trapped very close to the chip.

With typical currents of about $0.1\,A$, single site trapping frequencies obtained from our numerical analysis are approx. $1\,kHz$ for the longitudinal axis and $30\,kHz$ for the radial one (depending on the height above the AtomChip), giving an aspect ratio of around $1:30$. This high aspect ratio causes the radial wavefunction to have a Gaussian shaped solution (see Sec. 2.9), similar to single particle states, while the longitudinal axis simultaneously has a Thomas-Fermi profile. This state of affairs means that the lowest few radial vibrational state are occupied and the wavefunction behaves much like a one-dimensional system along the longitudinal axis.

An important distinction between the situation presented here and that in a typical optical lattice is the relative orientation of the adjacent atomic clouds. In an optical lattice, the individual clouds are displaced along their tightly trapped axis (see Fig. 4-2) while in

our case the clouds are separated along their loosely trapped axis.

After release from the trap, we expect expansion along the longitudinal axis to be much slower than along the radial axis (this is the origin of the well-known "flip" in aspect ratio, one of the signatures of BEC). Consequently, it will take longer for the separated clouds to overlap along the longitudinal axis and the anticipated interference patterns will only occur at longer expansion times than for optical lattices. Additionally, as we show below, no interference pattern can form at all if the expansion velocity is too slow. These difficulties can be overcome by releasing the trap sufficiently slowly, thereby effectively allowing the longitudinal expansion to "catch up" with the radial expansion of the cloud.
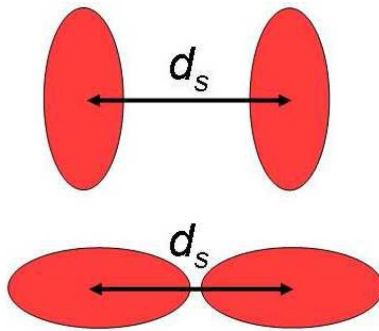

Figure 4-2: Orientations of adjacent clouds in typical lattices (top) and in our magnetic lattice (bottom). d_s is defined as the center to center distance between adjacent clouds. Taken from [54].

4.2 Sudden release

4.2.1 Fringe velocity

In this section we will discuss the relevant dynamics of interference fringes originating from an overlap of BEC wavefunctions suddenly released from the snake sites. To simplify the discussion we note that although the snake wire consists of many sites, many of the important characteristics of the interference fringes can be studied by analyzing a simple two-site model. While the width of each fringe depends on the number of sources, their number and spacing does not, as can be seen in Fig. 4-3.

Using the two-site model for the study of interference patterns between expanding BECs, we start by writing the total wavefunction as [15]:
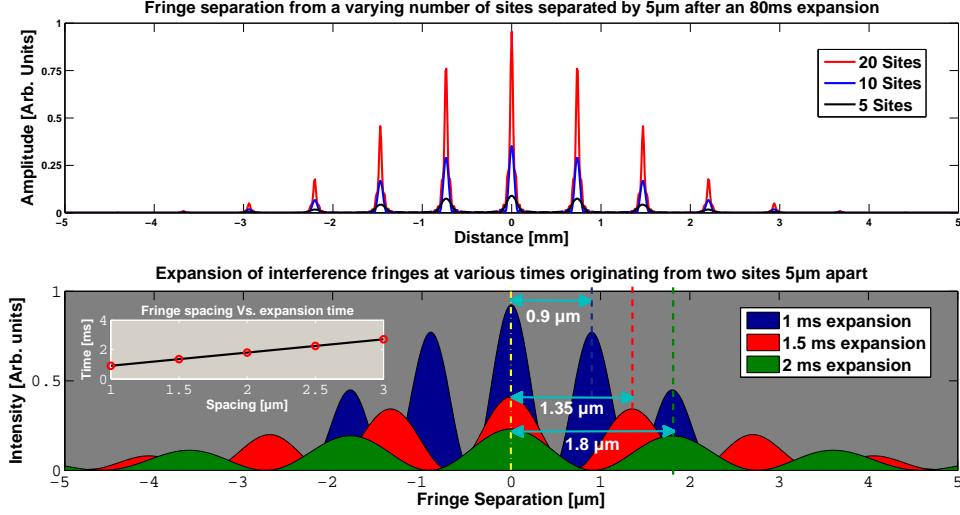
Figure 4-3: Interference pattern from 5,10 and 20 sites calculated by expanding wavepackets from localized sources separated by $5\mu m$. (Top) shows that the fringe separation is independent of the number of sites once the interference pattern has emerged. (Bottom) shows that the fringe spacing increases linearly with time, in this case at $0.9\,\mu m/ms$; the inset shows the linear relation between expansion time and fringe separation.

$$\Psi(\hat{\boldsymbol{r}}, t) = \sqrt{N_1}\psi_1(\hat{\boldsymbol{r}}, t) + \sqrt{N_2}\psi_2(\hat{\boldsymbol{r}}, t)e^{i\phi}, \tag{4.1}$$

where N_1 and N_2 are the number of atoms in the two sites, ψ_1 and ψ_2 are the single particle wavefunctions localized in the respective sites, ϕ the initial constant relative phase between the two sites and the wavefunction is normalized to the total atom number. The atomic density is then given by

$$n(\hat{\boldsymbol{r}}, t) = |\Psi(\hat{\boldsymbol{r}}, t)|^2 = N_1|\psi_1|^2 + N_2|\psi_2|^2 + 2\sqrt{N_1 N_2}\Re(\psi_1\psi_2^* e^{-i\phi}), \tag{4.2}$$

where $\Re$ denotes the real part of the multiplication of two sources with a fixed phase relation (with a quadratic spatial dependence due to their kinetic energy after the release) and thus has an oscillatory behavior in space and time. This behavior gives rise to an interference pattern in atomic density similar to the case of a Young double-slit experiment.

Next we will develop the expression for the fringe spacing in the interference pattern generated by overlapping clouds. In order to have an expression that takes into account the interaction of the particles we will follow the work of Castin and Dum [68] that showed analytically that for an expanding cloud in a time dependent harmonic trap the cloud size

57

evolves as if it undergoes a scaling transformation (a dilatation) for all three axes ($x \rightarrow \lambda_x(t)x$, $r \rightarrow \lambda_r(t)r$), where x and r are the longitudinal and radial directions respectively and $\lambda_i(t)$ is the time dependent scaling factor for the ith axis. The Castin-Dum derivation assumes a Thomas-Fermi profile for the expanding cloud (strong interactions) and thus neglects the kinetic energy term, writing:

$$\Psi(r,0) = \psi_{TF} = \left(\frac{\mu - U(\vec{r},0)}{Ng} \right)^{1/2}, \tag{4.3}$$

where μ is the chemical potential, $U(\vec{r},t) = \frac{1}{2}\sum_{j=1,2,3} m\omega_j^2(t)r_j^2$ is the time dependent harmonic potential, g is the interaction parameter and N is the atom number. To get ψ as a function of time one cannot use the standard Thomas-Fermi approximation since the time variation of the trapping potential can convert potential energy into kinetic energy, which therefore could no longer be neglected. However, by introducing the transformation:

$$R_j(t) = \lambda_j(t)R_j(0) \qquad (j = 1,2,3), \tag{4.4}$$

the authors were able to eliminate this extra kinetic energy while obtaining an equation for the scaling factors $\lambda_j(t)$:

$$\ddot{\lambda}_j = \frac{\omega_j^2(0)}{\lambda_j\lambda_1\lambda_2\lambda_3} - \omega_j^2(t)\lambda_j, \tag{4.5}$$

with the initial conditions $\lambda_j(0) = 1$ and $\dot{\lambda}_j(0) = 0$ (since the cloud is initially at rest). The form of the time dependent wavefunction after the transformation is:

$$\psi(\vec{r},t) = e^{-i\beta(t)}e^{im\sum_j r_j^2\dot{\lambda}_j(t)/2\hbar\lambda_j(t)} \times \frac{\tilde{\psi}[r_k/\lambda_k(t)_{k=1,2,3}]}{\sqrt{\lambda_1\lambda_2\lambda_3}}, \tag{4.6}$$

where $\beta(t)$ is a global phase factor obtained from $\hbar\dot{\beta} = \mu/\lambda_1\lambda_2\lambda_3$ and $\tilde{\psi}$ is the transformed Thomas-Fermi solution.

For cigar shaped traps ($\omega_y = \omega_z \equiv \omega_\perp \gg \omega_x$) and for the simplest case of a sudden release of the trap at $t = 0$ the equation (4.5) for the evolution of the scaling parameters simplifies to:

$$\frac{d^2}{d\tau^2}\lambda_\perp = \frac{1}{\lambda_\perp^3\lambda_x}, \qquad \frac{d^2}{d\tau^2}\lambda_x = \frac{\epsilon^2}{\lambda_\perp^2\lambda_x^2}, \tag{4.7}$$

where $\tau = \omega_\perp(0)t$, $\epsilon = \omega_x(0)/\omega_\perp(0) \ll 1$ and $\lambda_\perp$ and λ_x are the radial and longitudinal scaling parameters respectively. Solving up to second order in the small parameter ϵ one obtains for the expansion parameters:

$$\lambda_x(\tau) = 1 + \epsilon^2[\tau \arctan(\tau) - \ln \sqrt{1+\tau^2}] + O(\epsilon^4), \qquad (4.8)$$

$$\lambda_\perp(\tau) = \sqrt{1+\tau^2} \qquad (4.9)$$

where for long expansion times ($t \gg 1/\omega_\perp$) one gets:

$$\lambda_x(\tau) \approx \frac{\pi}{2}\frac{\omega_x^2(0)}{\omega_\perp(0)}t, \qquad (4.10)$$

$$\lambda_\perp(\tau) \approx \omega_\perp(0)t. \qquad (4.11)$$

One notices by looking at the previous results that the longitudinal expansion rate depends on both the longitudinal and radial frequencies while the radial expansion rate depends only on the radial frequency. This can be understood by noticing that the momentum (kinetic energy) of an atom in the trap has two sources, one is the initial momentum, which is proportional to the inverse of the initial width of the trapped condensate (and is thus larger for the radial direction) and the second originating from the gradient of the density (see for example Eqn. 2.22) and is due to interactions between the atoms (and is thus also larger for the denser radial direction). For these reasons, for high aspect ratio traps, the radial expansion is faster than the longitudinal one and the expansion of the radial direction will constitute the major contribution to the dilution of the density in the cloud and subsequently reduce also the repulsive force that causes acceleration along the longitudinal axis (notice that the radial trapping frequency is in the denominator in Eqn. 4.10), while the longitudinal expansion does not contribute much to the change in density causing the radial expansion to be independent of the longitudinal one.

Equation 4.10 allows us to plug into Eqn. 4.6 the following expression for λ_x:

$$\frac{\dot{\lambda}_x}{\lambda_x} \approx \frac{1}{t}, \qquad (4.12)$$

and obtain for the interference term in Eqn. 4.2 for the case of two sites separated by a distance d_s:

$$2\sqrt{N_1 N_2}\Re(\psi_1 \psi_2^* e^{-i\phi}) \approx A(r,t)\cos(\frac{md_s}{\hbar}\frac{\dot{\lambda}_x}{\lambda_x}x + \varphi(t)) = A(r,t)\cos(\frac{md_s x}{\hbar t} + \varphi(t)), \quad (4.13)$$

where the prefactor $A(r,t)$ represents the envelope (depending on time and space) of the expanding condensate and $\varphi(t)$ is a homogeneous phase (with a time dependence). The distance between adjacent peaks in the interference pattern is given by finding multiples of 2π in the above cosine expression:

$$\frac{md_s x}{\hbar t} = 2\pi n \rightarrow \Delta x = \frac{2\pi\hbar t}{md_s} = \frac{ht}{md_s}. \quad (4.14)$$

We see that for long times, the fringe separation is independent of the initial cloud size, resulting in a fringe velocity which depends only on the separation of the sites in the lattice:

$$v_x = \frac{h}{md_s}. \quad (4.15)$$

Thus the fringe velocity is a system constant, which in our case is $0.92\,\frac{\mu m}{ms}$ since the snake lattice periodicity is $5\,\mu$m. If the expansion velocity is faster than the fringe velocity, more and more atoms could reach regions of space occupying fringes and the interference pattern amplitude will increase with time. Later we will see that the longitudinal expansion velocity of our clouds is smaller than the fringe velocity for an abrupt release from the trap and the amplitude of the diffraction pattern will decrease with time under these conditions of trap release.

4.2.2 Expansion velocity

In what follows we will develop an expression for the expansion velocity within the individual clouds in order to compare it to the fringe velocity (Eqn. 4.15) and see if an interference pattern will emerge with time. We will again assume a Thomas-Fermi profile for the clouds along the longitudinal axis (for reasons described in Sec. 2.9 and as required by the Castin-Dum treatment). The longitudinal half-length of the cloud in the Thomas-Fermi

approximation is given at $t = 0$ by:

$$X_0 = \sqrt{\frac{2\mu}{m\omega_x^2}}. \tag{4.16}$$

Once the cloud is released, it expands according to the Castin-Dum equation discussed above and, using the expressions for a sudden trap shut-down and the limit of long expansion times ($t >> \frac{1}{\omega_r}$), we get for the condensate's half-width at time t:

$$X_t = \lambda_x X_0 \approx \frac{\pi}{2} X_0 \frac{\omega_x^2}{\omega_r} t = \frac{\pi}{2} \sqrt{\frac{2\mu}{m}} \frac{\omega_x}{\omega_r} t = \frac{\pi}{2} \left(\frac{15Na\hbar^2}{m^2} \right)^{1/5} \left(\frac{\omega_x^2}{\omega_\perp} \right)^{3/5} t, \tag{4.17}$$

where in the last step we have used the expression for the chemical potential in the Thomas-Fermi approximation $\mu = \frac{1}{2}\hbar(\omega_x\omega_\perp^2)^{1/3}(15Na\sqrt{m(\omega_x\omega_\perp^2)^{1/3}/\hbar})^{2/5}$ in order to express X_t in terms of the frequencies alone.

By plugging into the expression for the longitudinal expansion velocity (the derivative of Eqn. 4.17 with respect to time) typical values for the snake potential (a chemical potential $\mu \approx 1.4\,\mu\text{K}$ and aspect ratio $\omega_r/\omega_x \approx 30$) we get an expansion velocity of $\approx 0.85\,\frac{\mu\text{m}}{\text{ms}}$ which is lower than the $0.92\,\frac{\mu\text{m}}{\text{ms}}$ value we got previously for the fringe velocity. Considering that this expansion velocity is based upon the half-width of the cloud from Eqn. 4.16, the fringes separate faster than the majority of the expanding atomic density from each site. Therefore, a substantial optical density for the fringes will not build up. Altering the trap frequencies during a gradual and controlled trap release, thereby increasing the cloud longitudinal expansion velocity, would however, provide one possible solution for detecting an interference signal.

4.3   Controlled trap release

In this section, we propose releasing the trap gradually rather than suddenly. Considering that our traps have high aspect ratios, we will show that choosing the trap release rate carefully can ensure adiabatic evolution for the radial direction (thereby preserving optical density for longer expansion times), while simultaneously maintaining the initial momentum along the longitudinal direction. Looking at Eqn. 4.17 we notice that doing so will modify the trap aspect ratio to our advantage since it will increase the longitudinal expansion velocity while simultaneously slowing it down along the radial direction, which will give

the longitudinal axis more time to evolve under conditions of high density and increase its velocity further due to the added interaction energy. We will show that this method will allow the interference pattern to emerge before the optical density falls below the limits of our detection system. Using this method we hope to be able to see interference patterns from released clouds in our experiment.

We start the discussion by finding the relevant time scales. A trapping potential must change slower than certain time scales. A faster evolution will not allow the system to evolve adiabatically, where the adiabatic condition is given by:

$$\left| \frac{d\nu_{trap}}{dt} \right| << \nu_{trap}^2, \tag{4.18}$$

which in general must be maintained for each axis independently for the system as a whole to evolve adiabatically. As noted, the trapping frequencies of a typical site in the snake wire potential are on the order of $\nu_x = 1\,\text{kHz}$ for the longitudinal axis and $\nu_r = 30\,\text{kHz}$ for the radial one, defining different adiabaticity time scales of $t_x = 1/\nu_x = 1\,\text{ms}$ for the longitudinal axis and $t_r = 1/\nu_r = 33\,\mu\text{s}$ for the radial axis. Atoms in the trap will see perturbations of the trapping potential that occur faster than these time scales as abrupt changes and will not be able to follow them, thus for example, shutting down the trap abruptly in $1\,\mu\text{s}$ or in $10\,\mu\text{s}$ will have the same effect on the atoms. Closing the potential slower than both of these time scales will cause both the radial and longitudinal trapping frequencies to evolve to a lower value, but while a lower radial frequency is advantageous (as previously described), a lower longitudinal frequency will cause a slower expansion along the longitudinal axis, thus defeating our initial goal. Shutting down the trap in an intermediate time with a value between t_x and t_r will, on the other hand, be seen as an adiabatic process for the radial part of the atomic motion but as an abrupt change for the longitudinal part. The radial expansion will adiabatically lower the radial trapping frequency until Eqn. 4.18 no longer holds. Later on the cloud will expand freely in the radial axis as well as in the longitudinal one, but this time with a reduced radial trapping frequency. Assuming a release time of $250\,\mu\text{s}$ for example, Eqn. 4.18 shows that the adiabaticity criterion is satisfied for the radial direction, but not for the longitudinal one. The cloud will expand until Eqn. 4.18 no longer holds, i.e., until the frequency of the decaying trap evolves to a value of $1/250\,\mu\text{s} = 4\,\text{kHz}$. Fig. 4-4 shows how it is thereby possible to also flip the predominant expansion direction

from the radial to the longitudinal axis.

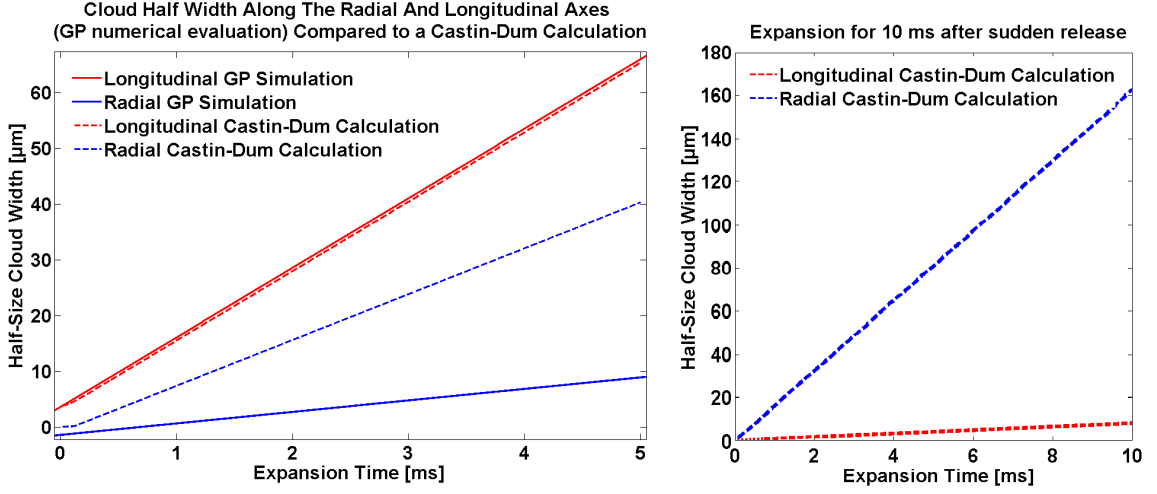Figure 4-4: Gradual Vs. Sudden release of a single site. A BEC trapped with a longitudinal frequency of $2\pi \times 1\,\mathrm{kHz}$ and a radial frequency of $2\pi \times 30\,\mathrm{kHz}$. On the left a time dependent Gross-Pitaevskii simulation of a BEC released gradually by shutting down the trapping potential in $250\,\mu\mathrm{s}$. On the right we show the case of a sudden release of the trap (Castin-Dum calculation). The half widths of the cloud longitudinal (red) and radial (blue) axes are plotted vs. time. The solid lines are linear fits to the numerical simulation, the dashed lines are the Castin-Dum calculated cloud widths. The longitudinal expansion is accurately described by the Castin-Dum expression since the profile is indeed a Thomas-Fermi one, as required for such a calculation. The radial expansion does not fit the Castin-Dum expression since for high trapping frequencies the kinetic term is no longer negligible and assuming a Thomas-Fermi profile gives incorrect results. Note particularly that the gradual release preserves the aspect ratio, whereas the sudden release results in a characteristic "flip" of the aspect ratio.

We end this section by comparing interference patterns resulting from sudden vs. gradual release of BECs from adjacent sites on the snake-wire potential, as shown in Fig. 4-5. The expression 4.11 for $\lambda_\perp$ and the Castin-Dum treatment for the radial direction cannot be applied in our case to obtain quantitative results, since (as discussed in Sec. 2.9) the high frequency in the radial direction means that the form of the wavefunction for this axis cannot be represented by the Thomas-Fermi approximation but is actually closer to a Gaussian. Thus the scope of the analytical derivation in the radial direction will be limited in our case to gaining only qualitative insight, and a numerical simulation of the time dependent Gross-Pitaevskii equation will be used to obtain quantitative results.
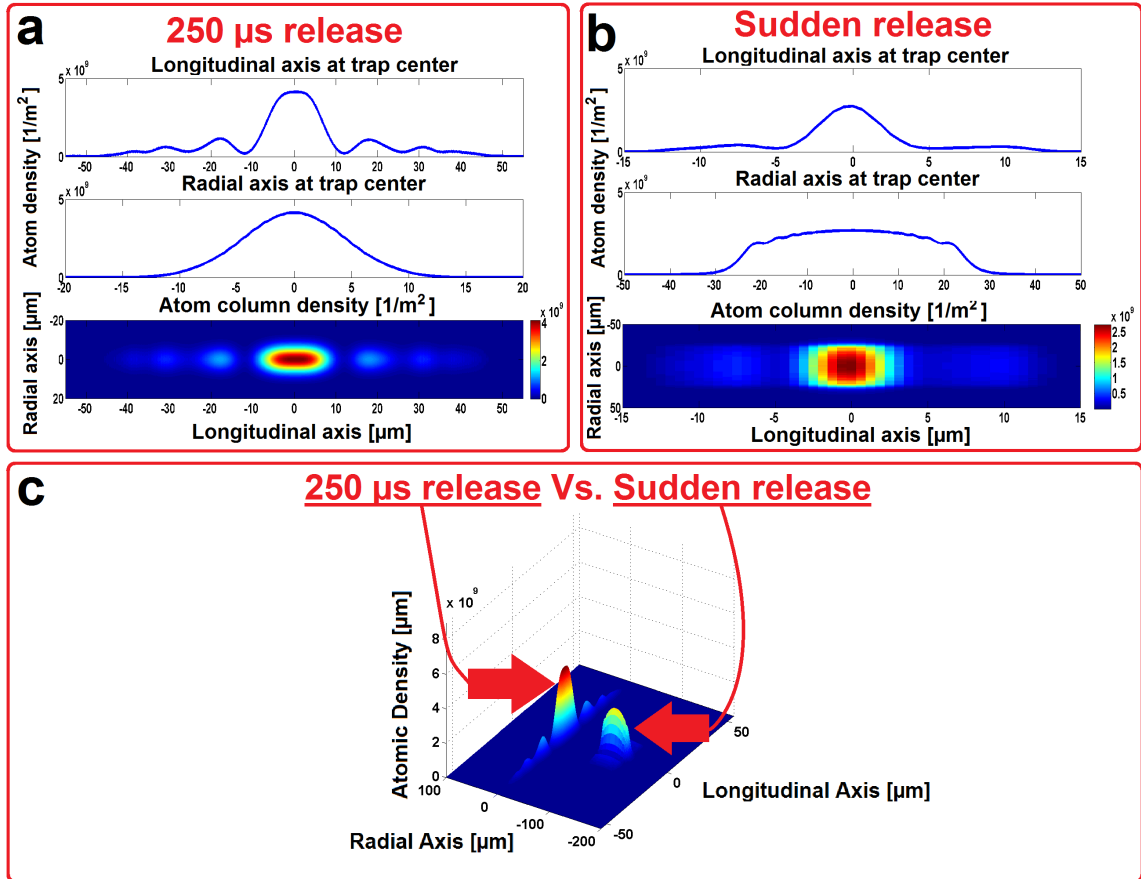
Figure 4-5: Interference patterns from two expanding clouds 10 ms after releasing them from the snake trapping potential. In (a) we show the result of a gradual release occurring over a period of 250 μs. In (b) we show the interference pattern originating from the sudden release of the trap (we show the atomic column density below and two profiles along the radial and longitudinal axes passing through the trap center). In (c) we show the 3D profile of the atomic density for both cases, clearly showing how atomic density is shifted from the radial direction to the longitudinal one. Note that the gradual and sudden release cases have different scales in the graphs. Both the zero order and first order interference fringes have a larger amplitude in the gradual release case. Also, the ratio of amplitudes between the first-order fringes and zero-order fringe is two times higher in the gradual release case, indicating that a gradual release indeed allows for a better formation of interference fringes.

4.4 Expansion from multiple sites

In order to demonstrate the method sketched above for many sites we show in Fig. 4-6 a simulation of a BEC of 125 atoms per site occupying 8 sites of the snake trapping potential after a 10 ms expansion. The comparison between the sudden and gradual release cases indicates that the method can indeed be used in our experiment to detect interference fringes from overlapping clouds. The interference pattern shown is taken after only 10 ms which is not a sufficient amount of time for a full pattern to form, but due to the fast dissipation of atoms from the trap we are constrained to measurements occurring shortly after the release, after which the density is too low for detection. The pattern shown however is sufficient to conclude that a superposition of coherent matter waves should indeed occur. The images were also processed to simulate our imaging capabilities by taking the Fourier transform of the image and removing the spatial frequencies which correspond to features which are smaller than our diffraction limit ($\approx 6\,\mu$m), and then binned to represent our $1.5\,\mu$m-sized pixels.

We now wish to verify that no other evolution of the system can imitate the signal we expect to observe. We have thus included a simulation done by expanding a single site and then copying it eight times, each time displacing it by the snake lattice periodicity ($5\,\mu$m). We then performed the calculation in two ways: first by squaring the amplitudes of each site (Fig. 4-7 a) and then adding them all together (thus eliminating any interference between sites) and secondly by first adding the amplitudes and then squaring the total wavefunction (Fig. 4-7 b). This calculation is an approximation to the full Gross-Pitaevskii picture since it neglects interactions between different sites and thus underestimates the expansion along the longitudinal axis (the interaction term g for ^{87}Rb is positive and thus represents a repelling force). We adopt this approximate procedure since a method that does not assume full coherence between different sites is not currently available. In addition to the comparison of the signal to an incoherent evolution we would like to also analyze the effect of partial coherence or random phases.

The Gross-Pitaevskii equation assumes full coherence of the BEC a priori and is thus inadequate for simulating several incoherent sources. In a real experimental setting however, a variation of the barrier height in the periodic potential will change the tunneling rate between the sites and consequently alter the coherence of the system. Altering the barrier
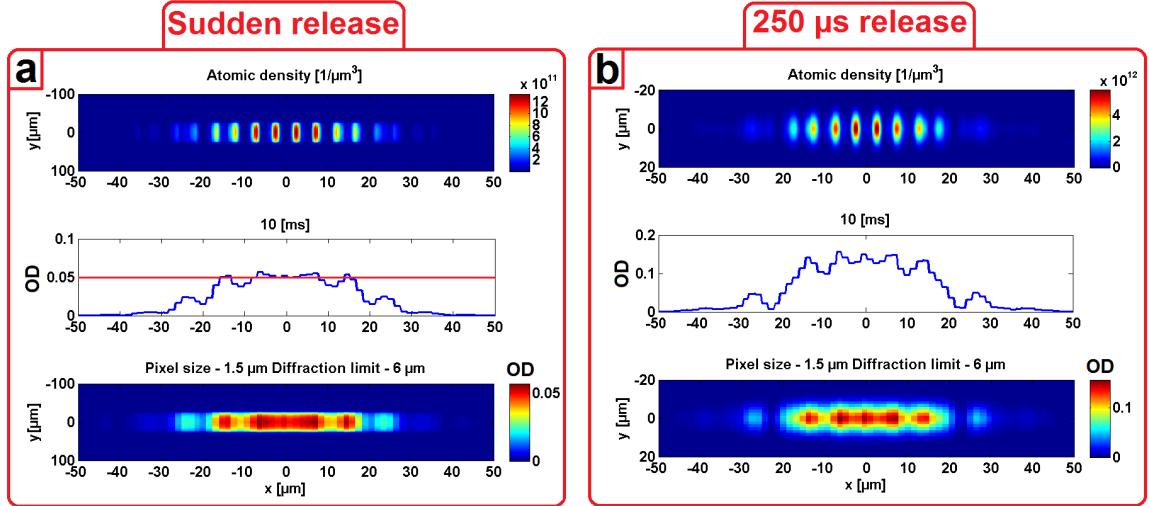
Figure 4-6: Comparison of sudden and gradual release from 8 sites (to be distinguished from the 2 site results in Fig. 4-5). The graphs describe the evolution of a BEC released from the snake potential after a 10 ms expansion. Box (a) shows the result of the calculation for the case of a sudden release of the trap while box (b) shows a calculation for a trap gradually released over a period of 250 μs. The boxes (a) and (b) are composed of three parts: on the top we show the calculated atomic column density of a BEC occupying 8 sites of the snake trapping potential 10 ms after being released. The calculation was performed by numerically solving the time-dependent Gross-Pitaevskii equation. The bottom part shows the image as it would be seen by our imaging system (see text). Note that the radial axis for the sudden release is expanded by a factor 5 relative to the gradual release. The central part shows a profile of the optical density at the center of the BEC. The interference pattern in the sudden release case is below our detection limit and will not be observed, while for the gradual release case it is within our capabilities (≈ 0.1 optical density).

height can be done by changing the current in the snake wire and is thus a tunable parameter in our system. In the previous calculations we have assumed that the tunneling rate is sufficient to establish full coherence between the different sites, but in practice this is not required since interference patterns will be observed even if no coherence relation exists between the sites. To convince the reader of this point we ran a simulation (Fig. 4-7 c-f) for a single site, copied it eight times as before, but this time assigning each site a random phase, thus creating a situation equivalent to an incoherent superposition of wavefunctions. The simulation shows that interference fringes do occur for each run but with random position. By averaging over ten such runs the interference pattern vanishes, indicating that this is indeed a simulation of incoherent sources that display constant phase relations between sites without having a global phase [69, 70, 71]. This simulation shows that interference fringes will be visible for any barrier height and a global phase encompassing all sites is

not required [72]. The signature for having such a global phase (i.e. for barrier heights low enough to allow for a sufficient tunneling rate) is a reduction in the fluctuations of the fringe position [72], i.e., of a deterministic fringe pattern remaining visible even after averaging many runs.

Following this simulation work we have designed and built an electrical shutter for the controlled closing of the $\hat{y}$-bias magnetic field. Enabling synchronized and controlled extinction of the external coils and trapping wire currents will allow us to realize the method of controlled release and improve the fringe contrast (visibility) in our interference experiments.
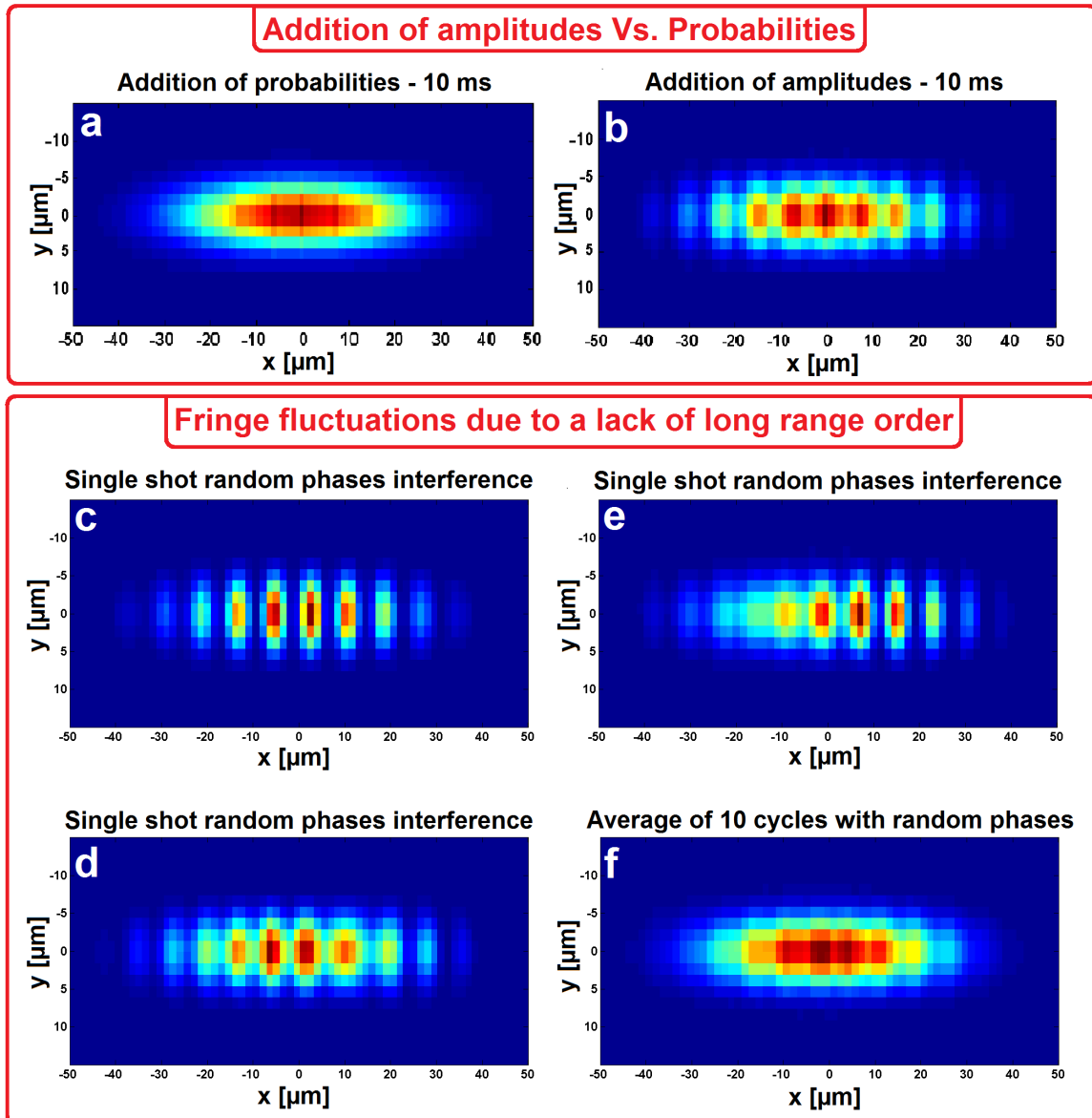
Figure 4-7: Interference fringes from coherent and incoherent BEC clouds. These six images show calculations in which the expansion of a single site has been evaluated and then copied 8 times, each time displaced by the snake periodicity ($5\,\mu$m). In (a) the addition was done after squaring the amplitudes, thus eliminating any interference between sites. In (b) the individual wavefunction amplitudes were added and then the total was squared, thus displaying an interference pattern. This illustrates that the source of density modulation is indeed due to phase relations between adjacent sites. In (c), (d), and (e) each site has been assigned a random phase prior to adding amplitudes and squaring the total, thus simulating a situation where no long range coherence exists and the relative phase between adjacent sites is random. Three different iterations of the same simulation are shown to demonstrate the resulting fluctuations in the fringe position. This illustrates that even in the case where the coherence does not extend over the whole snake lattice interference fringes are still visible. In (f) we see an average of ten runs showing that the interference pattern is washed away when averaging over many consecutive experimental runs; averaging successive experiments to improve the signal-to-noise ratio would in this case result in reduced fringe contrast compared to the case shown in (b).

Chapter 5

Vertical Imaging

The manipulation of atomic clouds using AtomChip technology requires the positioning of trapping potentials to within a few μm. As outlined earlier, we rely on absorption imaging techniques (Sec. 3.4), which yield the atom density integrated along an axis parallel to the plane of the AtomChip. The position of the atomic cloud along the imaging axis is therefore lost, and no information is available on the cloud position relative to structures on the AtomChip surface. Regaining this information, by using an imaging axis that is perpendicular to the AtomChip, can therefore be very helpful, particularly for precisely positioning the atomic cloud near specific features of the chip. The presence of the AtomChip itself obstructs the view from this axis and a special imaging system was designed in order to overcome this obstacle. The requirements from such a system are purely geometrical, to allow us to determine the position of the atomic cloud relative to the various AtomChip wires. Since the size of these elements is typically on the scale of a few tens of μm, it allows us to sacrifice resolution for simplicity. The standard analysis performed by the $\hat{x}$- and $\hat{y}$-axis imaging setups is not affected and can run independently. The design process and construction of such a system is described in this chapter, including examples that show the various advantages it provides us during daily operation.

5.1 Apparatus

The apparatus is shown in Fig. 5-1. Light emanating from the output of the imaging fiber goes through a standard microscope setup with a focal length of 200 mm for the lens closest to the chamber and 500 mm for a second lens positioned next to it. A further focusing on

69

the camera plane is done with a 25 mm focusing lens to allow us to position the camera at an arbitrary position along the optical axis.
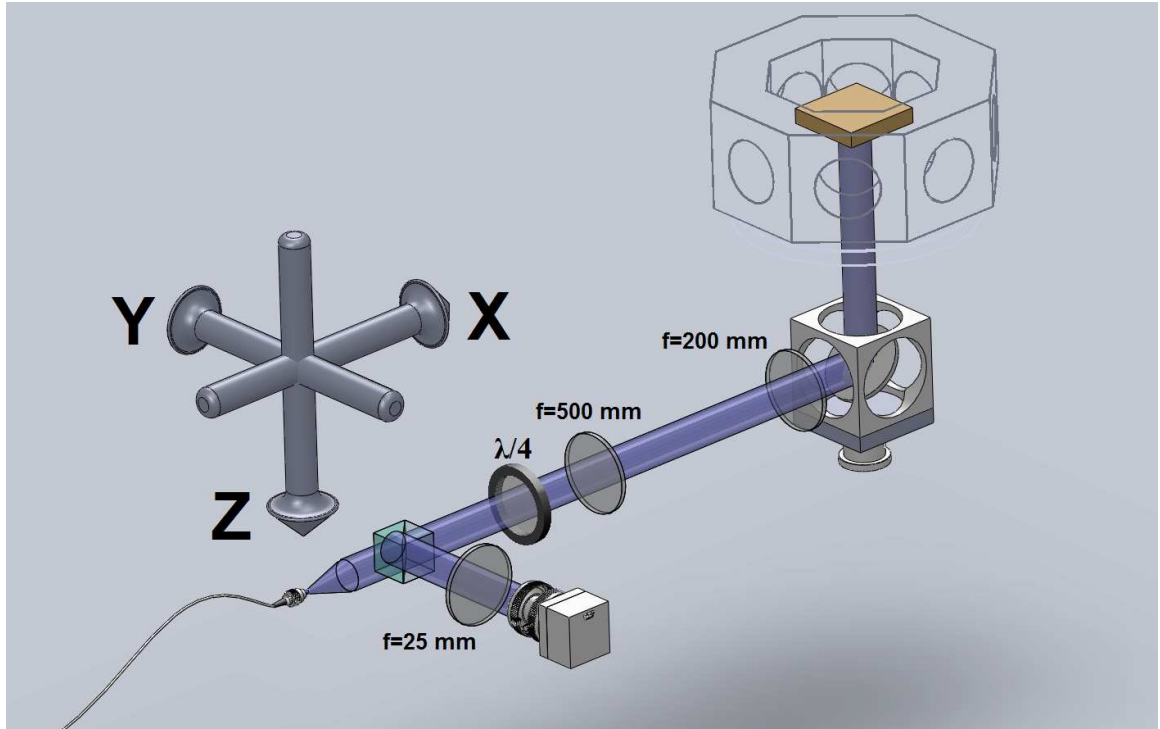

Figure 5-1: The vertical imaging setup. The imaging fiber output passes through a polarizing-beam splitter cube, a $\lambda/4$ waveplate and through 2 lenses. It is then inserted from the bottom window of the science chamber via a 45° mirror. The atomic cloud casts a shadow on the beam as in a standard absorption imaging setup. The light then reflects back on its path and passes the $\lambda/4$ waveplate again, shifting the polarization so that it will get directed by the polarizing beam-splitter cube into the focusing lens and the camera. The lens closest to the chamber has a focal length of 200 mm and is focused on the Atom-Chip, while the second lens along the beam path has a focal length of 500 mm resulting in a magnification of approx. 2.

5.2   Test bench

In the initial stages of design we had several concerns regarding the vertical imaging of an atomic cloud a few wavelengths away from a reflective surface. One such concern was the effect of diffraction from the surface structures. Hence, although the resolution requirements were not very strict (we were looking for anything below $10\,\mu$m), we decided to develop and test the system in a dedicated manner. In order to experiment with several configurations, we manufactured a special resolution target by coating an old unusable AtomChip with a

$1\,\mu$m layer of photoresist (SU8) and deposited a thin layer of gold on top, thus creating a resolution target elevated $1\mu m$ away from the AtomChip. Figure 5-2 displays the end result and the capabilities of our imaging system in resolving the target. Although quite modest, this resolution is adequate for our needs and was later incorporated into the main system as described in the next section.
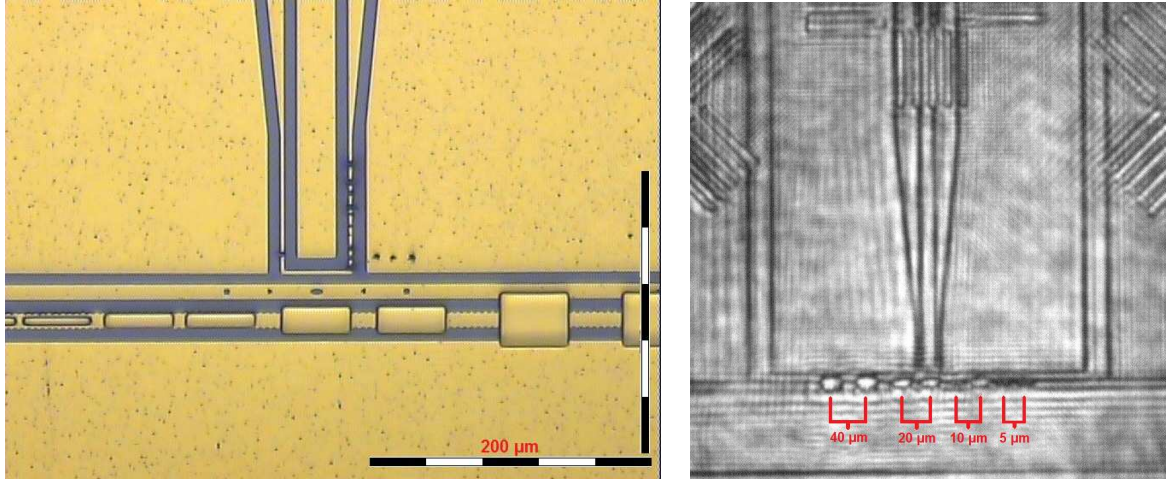

Figure 5-2: Vertical imaging resolution target. The resolution target on a test chip (on the left) and how it was seen using our vertical imaging system (on the right). In the resolution target, the line of rectangle shapes is the added layer above the SU8 layer. The rest of the structures belong to the old chip used for this test.

5.3 Applications (magnetic trap and chip loading)

Using the previously described system we are able to establish the position of the atomic cloud relative to the various AtomChip elements. Figure 5-3 shows how we use the vertical imaging in order to help us optimize the transfer of the MOT to the magnetic trap. The trap position and size of the compressed MOT and Z-trap must be matched in order to transfer the atoms without causing any heating or loss. By using the vertical imaging, matching these parameters for an optimal transfer of atoms is much easier and more accurate than with imaging systems used previously.

We have used the vertical imaging system to perform two tasks. The first is to assist us in loading the magnetic trap from the MOT (shown in Fig. 5-3), the second was to facilitate the loading of specific AtomChip wires when we were still working with the BGU0 AtomChip (an older version) which had the AtomChip Z-wire misaligned with the copper
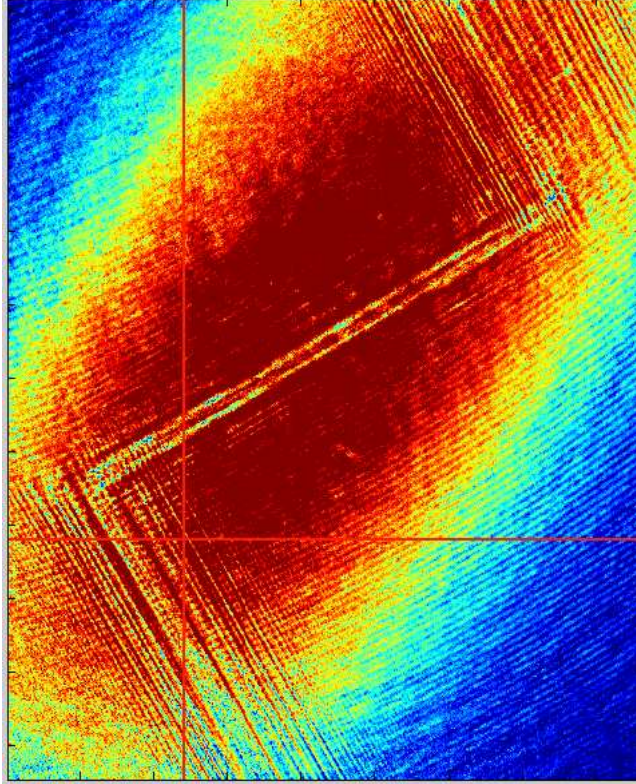
Figure 5-3: Magnetic trap using the copper Z-wire and bias fields. There is no current flowing through the AtomChip Z-wire but it is visible in the image due to scattering of the imaging beam upon reflection from the AtomChip. The position of the trap is symmetric around the AtomChip Z-wire without the need to apply a lot of bias field along the $\hat{z}$-axis, indicating a good alignment of the BGU1 chip with the macor piece and the copper structures. In the previous AtomChip (BGU0), the alignment was poor and required us to apply a $\hat{z}$-bias field which complicated the loading sequence to the AtomChip later on. Moreover, this misalignment was not readily measurable with the imaging system used previously.

Z-wire. Figure 5-4 shows the second application. The images were taken while trying to optimize the AtomChip BGU0 loading event. On the left we see an atomic cloud trapped with both the copper Z and the AtomChip Z-loading wire. Due to a misalignment between the copper Z and the AtomChip loading Z-wire the minima of the two potentials are difficult to superimpose adequately, resulting in an effective minima positioned a few microns away from the AtomChip Z-wire. Consequently a complete transfer of the atoms to the AtomChip potentials was much more difficult. Using the vertical imaging system this problem can be easily identified and fixed by optimizing the relevant currents through the various wires and bias fields while observing the position of the cloud. The new imaging system successfully enabled us to position it on top of the AtomChip Z-trap and subsequently transfer the cloud to a trap generated by the AtomChip currents alone.
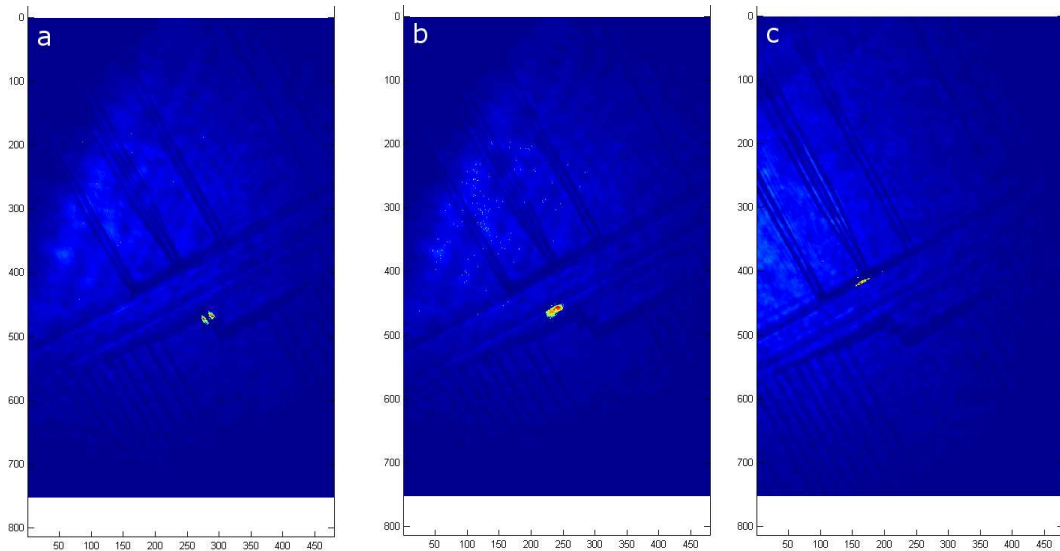

Figure 5-4: Vertical imaging of atomic clouds on top of various locations on the AtomChip. (a) The cloud is positioned far away from the AtomChip Z trap, the seemingly split cloud is in fact a single one accompanied by its reflection from the chip. (b) By tweaking the relevant currents and bias fields the cloud position is optimized towards its desired position. The cloud and its reflection are now less separated since the height is lower, approaching complete loading of the atoms on the chip. (c) The atomic cloud is now trapped using only the AtomChip wires and bias fields at a height of less than $10\,\mu$m. The visible increase in the cloud aspect ratio is due to the removal of the copper Z contribution from the potential.

73

Chapter 6

Optimization Algorithms

In our experimental setup, both the system's control and the data analysis are performed by a computer, resulting in an almost fully automated run of the experimental cycle. In contrast, the tweaking of the various parameters to fit our demands is still essentially carried out by trial-and-error, resulting in a lengthy process of parameter selection. In order to solve this problem we have incorporated a control system that automatically performs the process of parameter optimization by employing an optimization based on Genetic Algorithms (GA). By employing these methods in our control system we were able to reduce the amount of time required to optimize the system for day-to-day operation. More specifically, we have improved the MOT stage. In the future it is hoped that this system will also be able to improve the interference signal by optimizing the loading, trapping and releasing of the snake lattice. In this chapter we will discuss the nature of these methods in detail with a particular emphasis on their implementation in the settings of an atomic physics experiment [73], referring to concrete examples where possible.

6.1 Theory of global optimization algorithms

Optimization algorithms are methods for finding optimal solutions for a given problem. In the context of computer science a "problem" is defined as an objective function $f(\vec{x})$ that returns a value we are seeking to maximize. The input to the objective function is a vector $\vec{x}$ that contains a list of input values to the system (such as currents, laser detuning etc.). The goal of an optimization algorithm is straightforward: to find an input $\vec{x}$ that maximizes (or minimizes) $f(\vec{x})$ (there is of course no difference, maximizing the function

$f(\hat{x})$ is equivalent to minimizing $-f(\hat{x})$). Objective functions don't necessarily have to be mathematical expressions; as we shall see, they can also be actual experimental processes or simulations.

Optimizing real-life processes often has the disadvantage of having long execution times, requiring the user to be careful when choosing the right algorithm and its settings. The hyperplane that consists of all the possible values that $\hat{x}$ can attain is called the parameter space or landscape and is usually very large. Even a small problem may have many thousands of different configurations and an exhaustive search is usually not a viable option for finding optimal configurations. At first it might seem a simple task: one can start from an arbitrary point in the parameter space $\hat{x_0}$ and move iteratively in the direction of the gradient (by what is called the local hill-climbing method) until a maximum is found (see Fig. 6-1). Such methods are usually not very useful since simple landscapes with few maxima are rare and the hill-climbing method can converge to a local maximum that is very far from the desired global maximum, especially in real-life applications where noise is also an issue. It is then understood that what we need are methods that will explore large parts of the parameter space and find global maxima in an efficient manner.
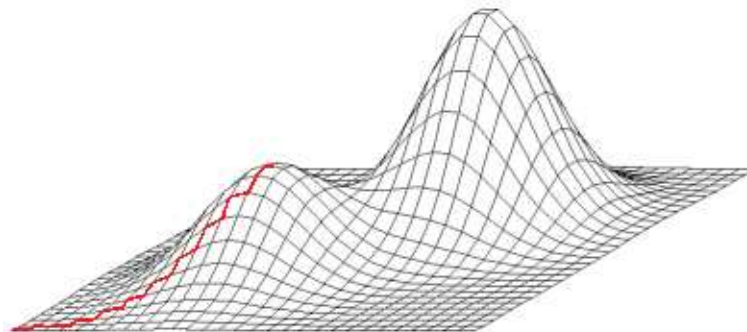
Figure 6-1: A naive approach to optimization. Hill-climbing type algorithms have the disadvantage of getting stuck on a local maximum or minimum.

6.2 Genetic algorithms

Genetic algorithms are based on imitating the process of evolutionary adaptation by means of natural selection as first described by Charles Darwin in his influential work from 1859 [74]. In Darwin's theory, a species is a set of individual organisms (a population)

that reproduces to form new generations of offspring. These offspring share some of their traits with their ancestors (heredity) and also display a certain amount of random variation (mutation). The peculiar characteristics of a certain environment cause some individuals in the population to be less likely to survive and reproduce. Such unfortunate individuals are said to be less fit for that particular environment. The fittest individuals are then selected preferentially for reproduction, allowing them to pass on their traits to their offspring. The random variations present in the reproduction process diversifies the following generation's overall spectrum of traits and subsequently allows for a quicker adaptation of the species to the environmental constraints. In this way, an improvement in the probability to survive is produced as we progress through the generations and an evolution of the species is said to occur. The mechanics of heredity, by which offspring acquire (with variations) the characteristics of their parents, is controlled by genes which encode the various traits possessed by an organism; some of these genes are transfered from parent to offspring and some are randomly generated. The complete set of genes of an organism is called its genotype and it is precisely this genotype which evolves between generations to adapt to a specific environment.

The influential work of Darwin inspired computer scientists to design algorithms that mimic the natural selection process in order to solve various problems. Artificial evolution became a widely recognized method as a result of the work of Ingo Rechenberg [75] where he used evolution strategies to solve complicated engineering problems. The application of artificial evolution to generate useful solutions to optimization and search problems became popular following the influential work of Holland in 1975 [76] that will be discussed later on.

In genetic algorithms, the role of the environment is portrayed by the function we wish to optimize (the "fitness function") which sets the standard against which proposed solutions to the problem are compared. The process (see Fig. 6-2 for reference) involves the random generation of an initial "population" of individuals $\{\vec{x}_i\}$, each one a candidate for the maximization of the said function. An evaluation process then evaluates the fitness function for each individual and calculates its fitness, which is nothing but the value of the function $f(\vec{x}_i)$ we wish to optimize. Once this is done a new generation of candidate solutions is formed from the previous one by a process that resembles breeding; Pairs of individuals are chosen based on their relative fitness and new "offspring" are generated by
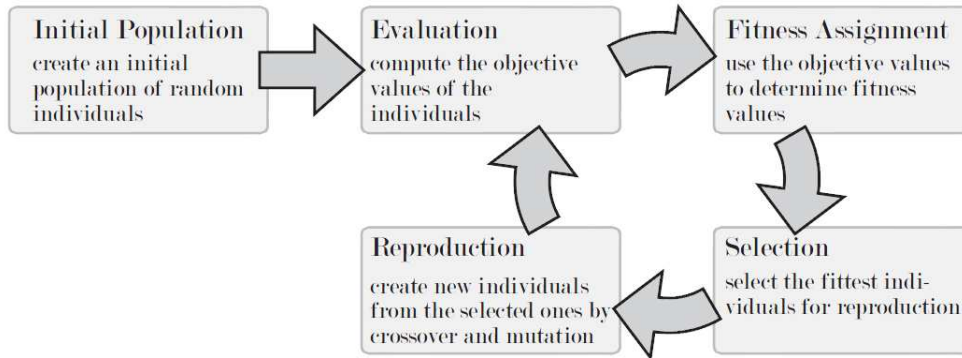
Figure 6-2: The basic cycle of evolutionary algorithms. Taken from [77].

inheriting values from each parent (a crossover operation). Mutation is allowed by having a small part of the new values generated randomly. In the context of genetic algorithms, a simplistic (from a biology standpoint) notation is used in which an individual is fully represented by a "chromosome" which is just a string of numbers, or genes. In this context an individual and his chromosome are actually the same object.

Let us discuss the details of the method in the context of a concrete example. Fig. 6-3 shows the results of our implementation of a genetic algorithm to maximize the number of atoms in a magneto-optical trap (MOT). The control parameters (the genes, components of the chromosome) are the cooler and repumper detuning frequencies and the repumper output power, comprising the x, y and z axes respectively. Each point represents an individual (a chromosome) composed of these three parameters (genes), and each generation consists of a population of ten such individuals. For example, the individual $\{5, 6, 2\}$ is composed of three genes: the cooler frequency, the repumper frequency and the repumper power with values 5, 6 and 2 respectively. The 3D plots represent the parameter space of this particular optimization problem during a period of 4 generations. Initially, the algorithm randomly generates a set of ten individuals to populate the first generation. The experimental system is then run once for each individual, updating the lasers frequencies and power to correspond to the individual's values. The imaging system then takes an absorption image of the atoms and calculates the corresponding atom number in the MOT, representing each individual's fitness value. The ten individuals are then ranked according to their fitness values, and the best ones are given a higher probability to breed and create the following generation. In our system each run takes 1 minute to complete. Since a generation is comprised of
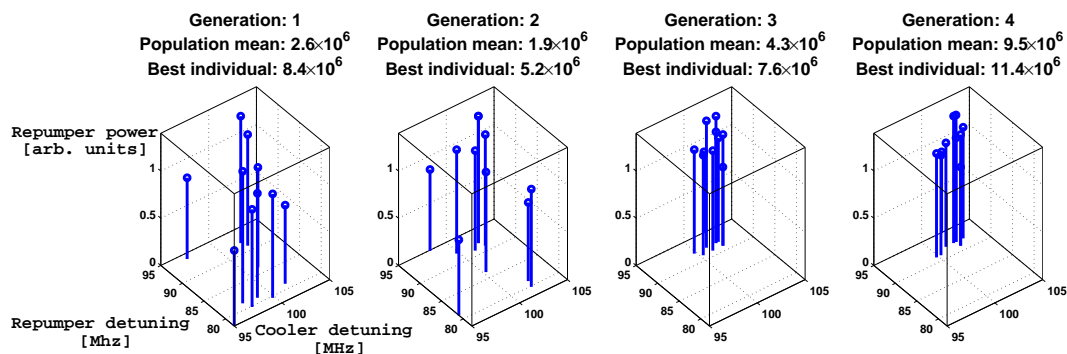
77

Figure 6-3: Optimizing the MOT. Optimization of the number of atoms in a magneto-optical trap (MOT) using a genetic algorithm, showing a population of 10 individuals evolving for four generations with a total running time of 40 minutes. The spread in repumper power remained relatively constant throughout the optimization process, indication that the system is relatively insensitive to this parameter.

ten individuals, the whole optimization task took 40 minutes to complete. During this run an improvement of 35% is achieved in the number of atoms without human intervention. Notice also that as the evolution progresses the scatter of the points is reduced, indicating that the algorithm converges. The improvement referred to here is that of the best overall individual and not the mean fitness of the population, since what we are looking for is one set of optimal parameters and not a family of values. The mean fitness of each generation is provided by the software (which is based on Matlab's optimization toolbox adapted for our needs) in order to monitor the convergence of the algorithm.

6.2.1 Selection, crossover and mutation

Selection

The process of selecting a subset of the population for breeding is not as straightforward as one might expect. The simplest way of performing this operation is to assign a probability for breeding to each individual based on his fitness, and randomly select parents based on this weighted distribution. The downside of this approach (especially for small populations) is that the initial distribution of fitness scores has a large standard deviation and a few fit individuals are usually much better than the rest. A selection procedure based on a weighted distribution will then predominantly choose a small subset of the population for reproduction and will not allow the descendants of less fit individuals a chance to explore the parameter space more thoroughly. The selection process can then be said to be too

78

"elitist", causing a dilution of diversity and subsequently a premature convergence to a local optimum. It is then said that the process puts too much emphasis on "exploitation" over "exploration", favoring highly fit individuals at the expense of exploring other regions of the search space. We will see throughout this treatment that a good balance between these two qualities is basically what is needed in order to have a successful optimization process.

In order to compensate for this overly elitist selection process several other scaling methods were developed. One of the most common is the so-called "sigma scaling" method in which individuals are given an expectation value for selection normalized by the standard deviation of the population, for example [78]:

$$
\begin{cases}
1 + \frac{f(i) - \bar{f}}{2\sigma} & if \ \sigma \neq 0 \\
1 & if \ \sigma = 0
\end{cases}
\tag{6.1}
$$

where $f(i)$ is the fitness of individual i, $\bar{f}$ is the mean fitness of the population and σ the standard deviation. Such a scheme normalizes the selection based on the variation in the population. At an early stage, the population has a large standard deviation and so the fittest individuals will not be many standard deviation above the mean and consequently will not be selected so often. As the algorithm progresses, the deviation becomes smaller (see Fig. 6-3) and the fittest individuals will stand out more, driving the algorithm towards convergence. This method is designed to keep a constant "selection pressure" (the amount of offspring allocated to highly fit individuals) throughout the evolution process.

In addition to selection we also apply an "elitism" operation which keeps a fraction of the fittest individuals for the next generation, ensuring that the fittest individuals are not lost due to mutation/crossover or simply because they were not selected, and allows their genes to propagate to the next generations. Also, since the values assigned to each individual have a random character (system stability, shot-to-shot noise) this procedure allows for a better estimation of the fittest individuals since they are re-evaluated several times.

Crossover

The use of a crossover operation is often said to be the distinguishing feature of genetic algorithms since it is precisely this operation which allows the algorithm to propagate successful

forms of solutions from one generation to the next (more on this later in the section on the "schema" theorem). Here also, we need to be careful in choosing a proper implementation of this core process. The simplest form of such an operation is the single-point crossover function (see Fig. 6-4), in which a point i in the chromosome is randomly selected and an exchange of genes is performed between two parents such that the offspring is composed of the genes of parent A up to point i and of parent B from that point onwards. Again, as in the case of the selection process, we get into trouble by choosing the most straightforward method. One of the problems with using a single-point crossover is that not all possibilities are accessible to the offspring. For example, two parents having chromosomes of the form [1###1] and [##1##] (the wildcard # can take any value, [1###] for example refers to all the chromosomes starting with 1, this notation defines a hyperplane of chromosomes, also called a "schema") will not be able to produce an offspring of the form 1#1#1 with a single-point crossover mechanism. Also, the first and last bits of the chromosome are transferred to the offspring in a preferential manner since they always appear in their original position. Furthermore, long blocks of genes that form successful parts of a chromosome are more easily destroyed compared to short sequences, causing the process to eventually favor solutions with short building blocks, which cannot be justified a priori. To overcome these we use a multi-point crossover scheme (see Fig. 6-4 for an example of a two-point crossover), in which several points $i, j, ..$ are chosen at random and the chromosomes in between are exchanged. Some practitioners [79] advocate using "parametrized uniform crossover" in which an exchange happens at each chromosome position with a probability p (which is typically $0.5 < p < 0.8$). This form of crossover is highly disruptive and can in principle destroy more easily successful sequences in the chromosome. Which form of crossover to use is largely a matter of experimentation. Broadly speaking, a more general crossover mechanism such as parametrized uniform crossover allows an offspring to reach any possible permutation of his parents, thereby increasing the rate of exploration. This however comes at the expense of convergence, which typically slows down when the parameter space accessible to the population increases.

Mutation

The mutation rate is defined as the probability that a gene in a chromosome will be randomly generated. After the algorithm has assigned values to offspring via the crossover process, it

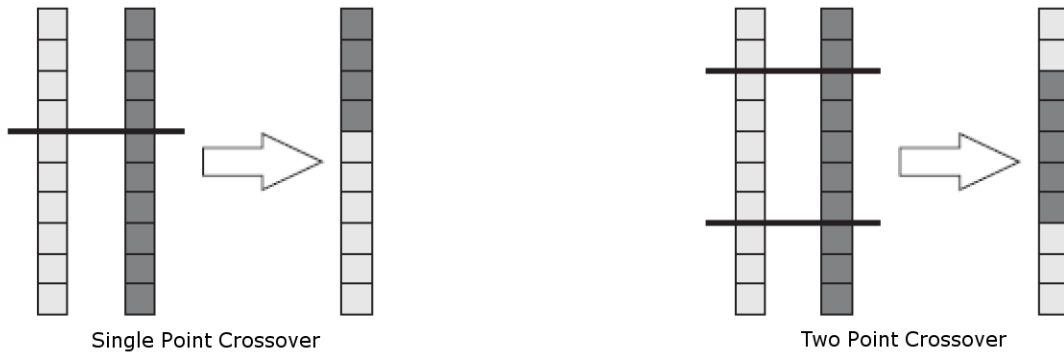Single Point Crossover   Two Point Crossover

Figure 6-4: Single-point Vs. two-point crossover. On the left, the single-point crossover operation mixes the chromosomes of the parents around a single position. This implementation has the disadvantage of limiting the number of possible permutations thus reducing diversity in the following generations. This can be overcome with more elaborate crossover operations such as the two-point crossover. Taken from [77].

selects a fixed percentage of the offspring's chromosomes and replaces them with randomly generated genes. This process allows one to fix a minimum value of the rate of exploration that is independent of other processes or even the initial population. Usually the mutation rate is taken to be quite low ($< 5\%$) so as not to disrupt convergence.

6.2.2   The Schema Theorem

Prior to discussing our implementation of Genetic Algorithms in more detail we must first present Holland's influential work on artificial adaptation giving us a framework for our future discussions. The work of Holland [80] is widely considered as the theoretical foundation for understanding the power of genetic algorithms. In it he describes how different characteristics of genotypes propagate during the evolution process.

The fundamental assumption of Holland was that genetic algorithms work by discovering, emphasizing, and recombining good "building blocks" of solutions in a highly parallel fashion [78]. The idea is that successful individuals tend to be composed of successful configurations of genes, and that there is an underlying structure to the chromosomes that is being propagated through the generations. The formal structure of Holland's theory is based on "schemas", previously mentioned, which are simply structural blocks that define hyperplanes of chromosomes. For example, the schema $H = [1\#\#\#]$ defines a hyperplane (thus the capital H) that groups all chromosomes with the value 1 assigned to their first gene, followed by any allowed combination of genes. We then say that the chromosome [1000]

is an instance of H. If an individual is an instance of two different schemas we say that the two schemas are "compatible". We then notice that any chromosome of length l is an instance of 2^l different schemas (we here take the genes to be binary variables for simplicity; for a general k-bit gene replace all occurrences of 2 with k). A population of N individuals then represents anything between 2^l and $N \times 2^l$ schemas (for example [10] is an instance of the four schema: [1#], [#0], [10] and [##], although some individuals may represent the same schema). This means that although each evaluation of a population only evaluates N individuals, it nevertheless simultaneously evaluates all compatible schemas, a much larger number of configurations, where the fitness of a schema is defined as the average fitness of all the chromosomes that are instances of that schema. By evaluating single individuals we are gradually obtaining information on the fitness of their related schemas, a feature that Holland has termed "implicit parallelism" and that is the fundamental advantage of genetic algorithms.

A genetic algorithm will discover schemas which have a good influence on the overall fitness of the solution candidates. The genetic algorithm is then seen as a search algorithm for schemas and not for optimal individuals. A successful schema will increase the fitness of the individuals which are a part of it and they will subsequently survive with a higher probability, transferring the schema to the next generation. Stated more precisely the schema theorem shows that schemas found in individuals with above average fitness scores propagate to the next generation in an exponential way, given by the equation:

$$E(m(H, t+1)) \geq \frac{m(H, t)f(H)}{a_t}[1 - p], \tag{6.2}$$

where m is the number of individuals which share the schema H, $E(m(H, t+1))$ is the expectation value of m in the following generation, a_t is the average fitness of the population and $f(H)$ the average fitness of the schema H. The term $[1 - p]$ is called the disturbance, and it represents the probability that crossover or mutation will destroy the schema H. Eventually we hope that a greater number of compatible schemas will be discovered in such a way, leading us to an optimal configuration.

The schema theorem helps us answer another important question relevant to our particular situation: given a fixed amount of time available to us (since each evaluation costs a dear one minute), should we run the system several times for each individual in order

to have a better evaluation of its fitness (due to shot-to-shot fluctuations)? or should we rather compromise on the precision of the fitness score and use the time saved in order to evaluate more individuals? It turns out [81] that the latter option is generally better, the schema theorem shows that what is actually being evaluated from generation to generation is the various schemas, which are anyway being evaluated several times for each population since the successful ones appear more frequently. In other words, the implicit parallelism of genetic algorithms allows us to find patterns in the parameter space even in the presence of considerable noise in the fitness evaluation, one of the major reasons why we have chosen genetic algorithms for system optimization in our experiment. We will later use the implications of the schema theorem to better understand how one should tweak the various parameters of the algorithm.

6.3 Applications (MOT, offline trap hunting)

In what follows we will go through two applications of genetic algorithms to our experimental challenges, throughout which our common goal is finding a balance between exploration and exploitation, namely, balancing the quality of the most successful individual with the speed of search. As previously mentioned, the importance of striking a good balance between the two is emphasized in our case by the fact that we pay expensively for each iteration (1 minute) and not many iterations of the algorithm are feasible.

Figure 6-5 displays an optimization process that maximizes the atom number in a MOT. Prior to running the algorithm we manually found a set of parameters that provided us with an initial vector. We fed that vector into the algorithm as one of the individuals in the first generation. After seven generations we were able to improve our MOT size by approximately 40%. The population size chosen was 12, a size that seemed to balance the speed of convergence with the quality of the final solution. The mutation rate was set at 1% and we used a scattered crossover function that generates a random 3-bit sequence, taking genes from one parent for each position where the outcome was 1 and the genes from the other parent where the outcome was 0. After 7 generations with a total run time of 108 minutes the algorithm converged to a solution as can be seen by the increase in clustering in the last generations relative to the first. Convergence is also evident as a decrease in standard deviation for the mean fitness of the various generations. The population scatter
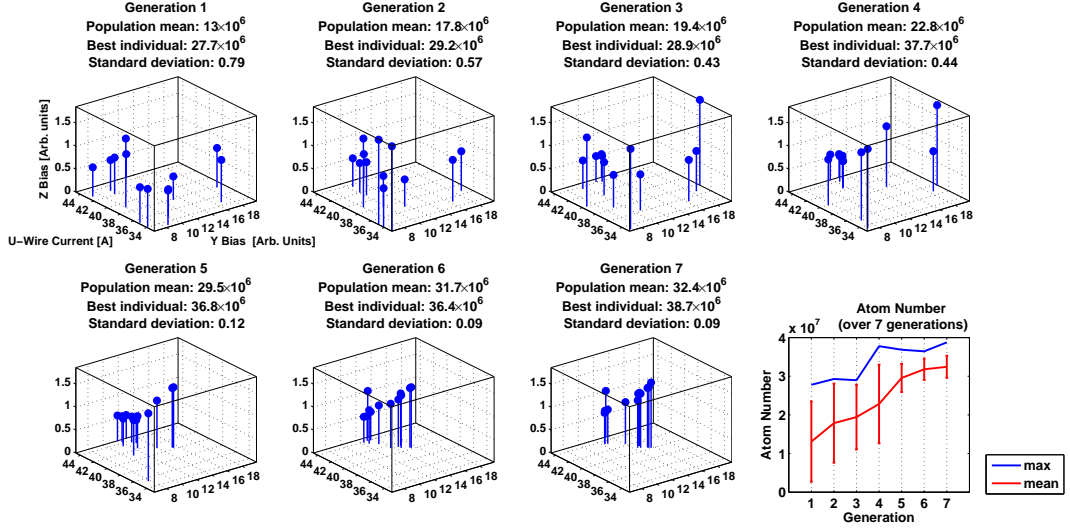
Figure 6-5: Optimization of the number of atoms in a magneto-optical trap (MOT) using a genetic algorithm. A population of 12 individuals evolves for seven generations with a total running time of 84 minutes. The control parameters used are the magnetic bias fields along $\hat{y}$ and $\hat{z}$ and the current through the U-wire. These parameters are chosen since they are the ones which define the shape and position of the trap. The last plot shows the evolution of the mean and maximum number of atoms in the population as the generations progress.

is relatively large in the first four generations indicating that the algorithm explores a large region of the parameter space. In the fourth generation a successful individual (relative to the population mean) is found, causing the algorithm to start converging toward the sub-region containing that individual. The evolution in the following generations is then mainly directed towards exploiting this sub-region of parameter space, indicated by the sharp drop in the population standard deviation (some 25% of the scatter in the first four generations). This exploitation finally finds a slightly better individual in this sub-region at the seventh generation. The fact that the algorithm automatically strikes a balance between exploring and exploiting the parameter space is due to the fact that the propagation of successful configurations has an exponential dependence on fitness (the schema theorem), thus causing the algorithm to exhibit these kinds of transitions from an exploring phase (generations 1-4) to an exploiting phase (generation 5-7) once an individual with a fitness considerably higher than the population mean is found.

Figure 6-6 shows the offline optimization process of a trapping potential. By modeling the AtomChip elements in a simulated environment we can input values for the currents pushed through the different wires and the bias fields along the three axes. The software
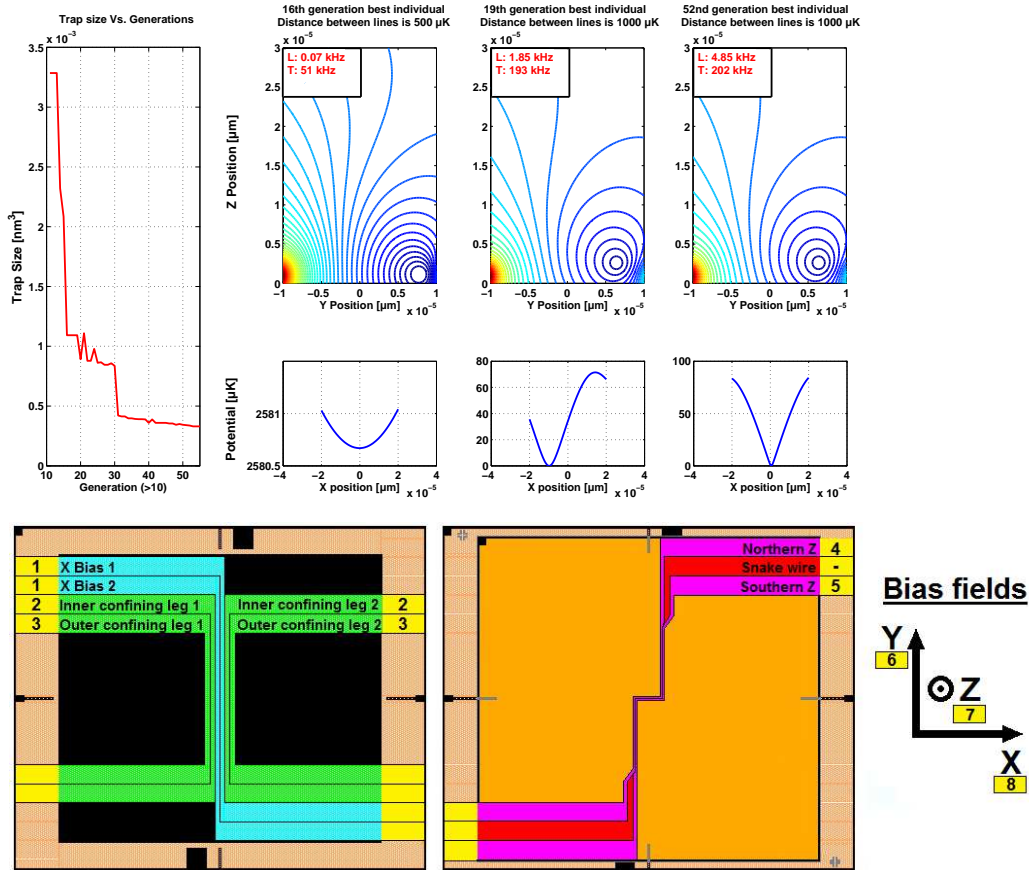
Figure 6-6: Off-line optimization using a genetic algorithm. Optimizing the trap size using 8 parameters: The $\hat{x}$-bias wires, the inner and outer confining legs, the two Z-wires, and the three bias fields (the wires and bias fields pertaining to these 8 parameters are shown in the figure below). The algorithm was given a large parameter space and thus started converging only after around 10 generations but then quickly found a parameter set corresponding to a tightly confining potential. Notice that the leftmost trap has a different energy scale for the trapping potential and is in fact much wider than the other two.

then calculates the various trap parameters using a finite-element method (if a trap is formed at all) corresponding to the input values. By letting a genetic algorithm optimize a certain trap parameter we are able to find useful current configurations without much trial and error. The offline optimization process is of course much faster since it does not require minute-long experimental cycles and thus allows for larger populations. In this process we have optimized the size of the trap (as defined by the Thomas-Fermi lengths along the three axes) by tweaking 8 parameters. The population size used was 50 and the algorithm converged to our requirements after 55 generations with a total run time of a couple of hours.

Aside from using genetic algorithms to optimize the real time execution of the experimental cycle we have shown how the method can be used to assist the researcher in finding new configurations of his system. By first creating a simulation of the experimental system in a computer, and later applying a genetic algorithm to test various configurations of the simulated environment, one can use the method in order to find parameter configurations that will optimize a high level goal, such as to find exotic trapping geometries or extreme values for various trap properties. We hope that this method will allow us in the future to design interesting trapping potentials by focusing on the final desired result instead of the standard method of parameter tweaking that in the end may limit the designer to a subspace of previously known geometries.

Chapter 7

Summary

In this work we have analyzed issues concerning the expansion and subsequent interference of BECs originating from adjacent sites of the 1D magnetic lattice created by our AtomChip wires. We have analyzed the specific features of our trapping potential, namely, that adjacent sites are aligned along their weakly confined longitudinal axis, and have found that the longitudinal expansion is too slow to allow adjacent sites to overlap sufficiently and form interference patterns with an optical density that will allow detection. We described how we may overcome these difficulties by gradually turning off the trapping potential rather than releasing the atoms suddenly and have shown that this gradual release method specifically alters trapping frequencies and expansion velocities of a BEC released from the snake potential. This mechanism can be exploited so that after an expansion period an overlap of adjacent sites will cause an interference fringe pattern to emerge. We have analyzed both analytically and numerically the situation for various scenarios and found optimal values that will enable fringe visibility to be within reach of our imaging system. Following this theoretical work we have designed and built dedicated electronics hardware that will allow us to perform the gradual release scheme. Being able to detect interference patterns from overlapping wavefunctions opens the way to probing coherence properties of a BEC in a 1D lattice. Since the height of the barrier depends on the current passed in the snake wire (a controlled quantity), the effect of trapping frequencies and tunneling rates may be studied. Success in this experiment will provide the first observation of matter-wave interference formed by a static magnetic trapping potential on an atom chip. It will also be the first controlled interference originating from a potential positioned only a few microns from the

chip surface. This will allow us to create and test interesting effects such as the super-fluid to Mott-Insulator transition, phase diffusion and decoherence and models based on Bose-Hubbard type Hamiltonians under new conditions.

We have also shown in this thesis, how imaging from the reflective surface of the Atom-Chip is possible with a resolution adequate for the determination of the position of atomic clouds above specific AtomChip wires. We have shown images of atomic clouds taken above the chip and demonstrated how this vertical imaging system has helped us to better position the cloud. Imaging issues such as diffraction from the chip wires and resolution limits were shown not to be detrimental for these tasks. The imaging system helped us analyze the misalignment of the various structures. By trapping an atomic cloud with the copper structure alone and imaging it with the vertical imaging we could detect that the center of the copper Z-wire was shifted relative to the AtomChip Z-wire. This inaccuracy was fixed in our new version by incorporating alignment marks on the AtomChip. All in all, our current imaging systems allows us to resolve the cloud position on all three axes in every shot.

In order to further optimize the signal by improving the loading, trapping and releasing of the snake lattice, we have also implemented a control system that utilizes a machine learning algorithm for the optimization of various tasks in the lab whether on-line or off-line. The system was embedded into our experimental setup and allows us to optimize user-defined specific goals (such as maximizing the number of atoms in a MOT) by automatically generating experimental parameters, evaluating them and reformulating new parameters based on previous results. The method was also employed off-line by running it on a simulated environment of the various wires and bias fields present in our lab. The user of the software can input parameters desired for the magnetic potential (e.g., minimum position, frequencies, etc.) and have the algorithm find optimal configurations of currents and bias field that will generate such a field.

As interference experiments with cold atomic clouds continue to be a topic of intense interest, the methods developed and optimized in this thesis could help experimenters achieve stronger interference and diffraction signals and hopefully improve the feasibility of future quantum devices.

Bibliography

[1] P.A.M. Dirac. *The principles of quantum mechanics.* Oxford University Press, USA, 1981.

[2] F. Laloë. Do we really understand quantum mechanics? Strange correlations, paradoxes, and theorems. *American Journal of Physics*, 69:655, 2001.

[3] P.W. Anderson. More is different. *Science*, 177(4047):393, 1972.

[4] R.W. Gurney and E.U. Condon. Quantum mechanics and radioactive disintegration. *Physical Review*, 33(2):127, 1929.

[5] R. Landauer and Th. Martin. Barrier interaction time in tunneling. *Review of Modern Physics*, 66(1):217–228, Jan 1994.

[6] J.R. Friedman, V. Patel, W. Chen, S.K. Tolpygo, and J.E. Lukens. Quantum superposition of distinct macroscopic states. *Nature*, 406(6791):43–46, 2000.

[7] N. Bohr. The Solvay Meetings and the Development of Quantum Physics. In *The Quantum Theory of Fields*, volume 1, page 13, 1961.

[8] N.D. Mermin. Could Feynman Have Said This? *Physics Today*, 57(5):10, 2004.

[9] L.D. Landau and E.M. Lifshitz. *Quantum Mechanics Non-Relativistic Theory: Volume 3.* Butterworth-Heinemann, 1981.

[10] R.K. Pathria. Statistical mechanics, 1996.

[11] F. Dalfovo, S. Giorgini, L.P. Pitaevskii, and S. Stringari. Theory of Bose-Einstein condensation in trapped gases. *Reviews of Modern Physics*, 71(3):463, 1999.

[12] M.H. Anderson, J.R. Ensher, M.R. Matthews, C.E. Wieman, and E.A. Cornell. Observation of Bose-Einstein condensation in a dilute atomic vapor. *Science*, 269(5221):198, 1995.

[13] K.B. Davis, M.O. Mewes, M.R. Andrews, N.J. Van Druten, D.S. Durfee, D.M. Kurn, and W. Ketterle. Bose-Einstein condensation in a gas of sodium atoms. *Physical Review Letters*, 75(22):3969–3973, 1995.

[14] C.S. Raman, J. Stenger, J.M. Vogels, Z. Hadzibabic, S. Inouye, C.E. Kuklewicz, A.E. Leanhardt, D.M. Stamper-Kurn, and C.A. Stan. Cooling and trapping neutral atoms.

[15] C. Pethick and H. Smith. *Bose-Einstein condensation in dilute gases*. Cambridge Univ Pr, 2002.

[16] F. Laloë and W.J. Mullin. Interferometry with independent Bose-Einstein condensates: parity as an EPR/Bell quantum variable. *The European Physical Journal B*, 70(3):377–396, 2009.

[17] Z. Guo-Feng, Y. Wen, L. Jiu-Qing, and Y. Qi-Wei. Generation of Bell states in two-component Bose–Einstein condensates. *Chinese Physics*, 13:988, 2004.

[18] R. Healey. Reduction and Emergence in Bose-Einstein Condensates. *Foundations of Physics*, pages 1–24, 2010.

[19] M. Greiner, O. Mandel, T. Esslinger, T.W. Hänsch, and I. Bloch. Quantum phase transition from a superfluid to a Mott insulator in a gas of ultracold atoms. *Nature*, 415(6867):39–44, 2002.

[20] I. Bloch. Ultracold quantum gases in optical lattices. *Nature Physics*, 1(1):23–30, 2005.

[21] B. Paredes, A. Widera, V. Murg, O. Mandel, S. Fölling, I. Cirac, G.V. Shlyapnikov, T.W. Hänsch, and I. Bloch. Tonks–Girardeau gas of ultracold atoms in an optical lattice. *Nature*, 429(6989):277–281, 2004.

[22] C. Orzel, A.K. Tuchman, M.L. Fenselau, M. Yasuda, and M.A. Kasevich. Squeezed states in a Bose-Einstein condensate. *Science*, 291(5512):2386, 2001.

[23] H.J. Briegel, T. Calarco, D. Jaksch, J.I. Cirac, and P. Zoller. Quantum computing with neutral atoms. *Journal of Modern Optics*, 47(2):415–451, 2000.

[24] O. Lahav, A. Itah, A. Blumkin, C. Gordon, S. Rinott, A. Zayats, and J. Steinhauer. Realization of a sonic black hole analog in a Bose-Einstein condensate. *Physical Review Letters*, 105(24):240401, 2010.

[25] K. Osterloh, M. Baig, L. Santos, P. Zoller, and M. Lewenstein. Cold atoms in non-Abelian gauge potentials: From the Hofstadter" moth" to lattice gauge theory. *Physical Review Letters*, 95(1):10403, 2005.

[26] E.A. Hinds, C.J. Vale, and M.G. Boshier. Two-wire waveguide and interferometer for cold atoms. *Physical Review Letters*, 86(8):1462–1465, 2001.

[27] S. Chu. Cold atoms and quantum control. *Nature*, 416(6877):206–210, 2002.

[28] A. Landragin, P. Cheinet, F. Leduc, and P. Bouyer. Atom Interferometry. *Optics in Astrophysics*, pages 359–366, 2005.

[29] C.S. Chuu, F. Schreck, T.P. Meyrath, J.L. Hanssen, G.N. Price, and M.G. Raizen. Direct observation of sub-poissonian number statistics in a degenerate Bose gas. *Physical Review Letters*, 95(26):260403, 2005.

[30] G.B. Jo, Y. Shin, S. Will, TA Pasquini, M. Saba, W. Ketterle, D.E. Pritchard, M. Vengalattore, and M. Prentiss. Long phase coherence time and number squeezing of two Bose-Einstein condensates on an atom chip. *Physical Review Letters*, 98(3):30407, 2007.

[31] J. Grond, G. Von Winckel, J. Schmiedmayer, and U. Hohenester. Optimal control of number squeezing in trapped Bose-Einstein condensates. *Physical Review A*, 80(5):053625, 2009.

[32] S. Choi and B. Sundaram. Bose-einstein condensate as a nonlinear ramsey interferometer operating beyond the heisenberg limit. *Physical Review A*, 77(5):053613, May 2008.

[33] J. Dunningham, K. Burnett, and W.D. Phillips. Bose-Einstein condensates and precision measurements. *Philosophical Transactions of the Royal Society A: Mathematical, Physical and Engineering Sciences*, 363(1834):2165, 2005.

[34] R. Folman, P. Krüger, J. Schmiedmayer, J. Denschlag, and C. Henkel. Microscopic atom optics: from wires to an atom chip. *Advances in Atomic, Molecular, and Optical Physics*, 48:263–356, 2002.

[35] L.I. Schiff. *Quantum mechanics 3rd ed.* McGraw-Hill, 1968.

[36] W. Greiner. *Quantum mechanics: an introduction.* Springer Verlag, 2001.

[37] C.G. Darwin. The wave equations of the electron. *Proceedings of the Royal Society of London. Series A*, 118(780):654, 1928.

[38] E. Arimondo, M. Inguscio, and P. Violino. Experimental determinations of the hyperfine structure in the alkali atoms. *Reviews of Modern Physics*, 49:31–76, 1977.

[39] D.A. Steck. Rubidium 87 D-line data. 2001.

[40] Y. Benhaim. Quantum optics of ultracold neutral atoms based on micro-scale magnetic traps (AtomChip). Master's thesis, Ben-Gurion University, Israel, 2009.

[41] S. Earnshaw. On the nature of the molecular forces which regulate the constitution of the luminiferous ether. *Trans. Camb. Phil. Soc*, 7:97–112, 1842.

[42] J. Dalibard and C. Cohen-Tannoudji. Laser cooling below the Doppler limit by polarization gradients: simple theoretical models. *Journal of the Optical Society of America B*, 6(11):2023–2045, 1989.

[43] H.J. Metcalf and P. van der Straten. Laser Cooling and Trapping. Graduate texts in contemporary physics, 1999.

[44] P.D. Lett, R.N. Watts, C.I. Westbrook, W.D. Phillips, P.L. Gould, and H.J. Metcalf. Observation of atoms laser cooled below the Doppler limit. *Physical Review Letters*, 61(2):169–172, 1988.

[45] A. Haase, D. Cassettari, B. Hessmo, and J. Schmiedmayer. Trapping neutral atoms with a wire. *Physical Review A*, 64(4):43405, 2001.

[46] E. Fleminger. Faculty of Natural Sciences. Master's thesis, Ben-Gurion University of the Negev, 2006.

[47] J. Reichel. Microchip traps and Bose–Einstein condensation. *Applied Physics B: Lasers and Optics*, 74(6):469–487, 2002.

[48] W. Ketterle, D.S. Durfee, and D.M. Stamper-Kurn. Making, probing and understanding Bose-Einstein condensates. In *Proceedings of the International School of Physics-Enrico Fermi*, page 67, 1999.

[49] D.E. Pritchard, K. Helmerson, and A.G. Martin. Atom traps. In *Atomic physics 11: proceedings of the Eleventh International Conference on Atomic Physics, 4-8 July 1988, Paris, France*, page 179. World Scientific Pub. Co. Inc., 1989.

[50] K.B. Davis, M.O. Mewes, M.A. Joffe, M.R. Andrews, and W. Ketterle. Evaporative cooling of sodium atoms. *Physical Review Letters*, 74(26):5202–5205, 1995.

[51] W. Ketterle and N.J. Druten. Evaporative cooling of trapped atoms. *Advances in atomic, molecular, and optical physics*, 37:181–236, 1996.

[52] S.N. Atutov, V. Biancalana, P. Bicchi, C. Marinelli, E. Mariotti, M. Meucci, A. Nagel, K.A. Nasyrov, S. Rachini, and L. Moi. Light-induced diffusion and desorption of alkali metals in a siloxane film: Theory and experiment. *Physical Review A*, 60(6):4693, 1999.

[53] T. David. *Magnetic Interactions of Ultra-cold Atoms Near Surfaces*. PhD thesis, Ben Gurion University, 2009.

[54] R. Salem. *Bose-Einstein Condensate on the Atom Chip*. PhD thesis, Ben-Gurion University of the Negev, 2010.

[55] S. Groth, P. Krüger, S. Wildermuth, R. Folman, T. Fernholz, J. Schmiedmayer, D. Mahalu, and I. Bar-Joseph. Atom chips: Fabrication and thermal properties. *Applied Physics Letters*, 85:2980, 2004.

[56] C.F. Ockeloen, A.F. Tauschinsky, R.J.C. Spreeuw, and S. Whitlock. Detection of small atom numbers through image processing. *Phys. Rev. A*, 82(6):061606, Dec 2010.

[57] D. Moravchik. Imaging methods of cold atoms. Master's thesis, Ben Gurion University, 2009.

[58] M.R. Andrews, M.O. Mewes, N.J. Van Druten, D.S. Durfee, D.M. Kurn, and W. Ketterle. Direct, nondestructive observation of a bose condensate. *Science*, 273(5271):84, 1996.

[59] B.P. Anderson, P.C. Haljan, C.A. Regal, D.L. Feder, L.A. Collins, C.W. Clark, and E.A. Cornell. Watching dark solitons decay into vortex rings in a bose-einstein condensate. *Physical Review Letters*, 86(14):2926–2929, 2001.

[60] A. Günther, S. Kraft, C. Zimmermann, and J. Fortágh. Atom interferometer based on phase coherent splitting of Bose-Einstein condensates with an integrated magnetic grating. *Physical review letters*, 98(14):140403, 2007.

[61] T. Schumm, S. Hofferberth, L.M. Andersson, S. Wildermuth, S. Groth, I. Bar-Joseph, J. Schmiedmayer, and P. Krüger. Matter-wave interferometry in a double well on an atom chip. *Nature Physics*, 1(1):57–62, 2005.

[62] G.B. Jo, J.H. Choi, C.A. Christensen, Y.R. Lee, T.A. Pasquini, W. Ketterle, and D.E. Pritchard. Matter-wave interferometry with phase fluctuating Bose-Einstein condensates. *Physical Review Letters*, 99(24):240406, 2007.

[63] P. Böhi, M.F. Riedel, J. Hoffrogge, J. Reichel, T.W. Hänsch, and P. Treutlein. Coherent manipulation of Bose–Einstein condensates with state-dependent microwave potentials on an atom chip. *Nature Physics*, 5(8):592–597, 2009.

[64] K. Maussang, G.E. Marti, T. Schneider, P. Treutlein, Y. Li, A. Sinatra, R. Long, J. Estève, and J. Reichel. Enhanced and reduced atom number fluctuations in a BEC splitter. *Physical Review Letters*, 105(8):80403, 2010.

[65] D. Jaksch and P. Zoller. The cold atom Hubbard toolbox. *Annals of Physics*, 315(1):52–79, 2005.

[66] Y. Japha, O. Entin-Wohlman, T. David, R. Salem, S. Aigner, J. Schmiedmayer, and R. Folman. Model for organized current patterns in disordered conductors. *Physical Review B*, 77(20):201407, 2008.

[67] S. Aigner, L.D. Pietra, Y. Japha, O. Entin-Wohlman, T. David, R. Salem, R. Folman, and J. Schmiedmayer. Long-range order in electronic transport through disordered metal films. *Science*, 319(5867):1226, 2008.

[68] Y. Castin and R. Dum. Bose-Einstein condensates in time dependent traps. *Physical Review Letters*, 77(27):5315–5319, 1996.

[69] M. Naraschewski, H. Wallis, A. Schenzle, J.I. Cirac, and P. Zoller. Interference of bose condensates. *Phys. Rev. A*, 54(3):2185–2196, Sep 1996.

[70] M.R. Andrews, C.G. Townsend, H.J. Miesner, D.S. Durfee, D.M. Kurn, and W. Ketterle. Observation of interference between two Bose condensates. *Science*, 275(5300):637, 1997.

[71] A. Polkovnikov, E. Altman, and E. Demler. Interference between independent fluctuating condensates. National Acad Sciences, 2006.

[72] Z. Hadzibabic, S. Stock, B. Battelier, V. Bretin, and J. Dalibard. Interference of an array of independent bose-einstein condensates. *Phys. Rev. Lett.*, 93(18):180403, Oct 2004.

[73] W. Rohringer, R. Buecker, S. Manz, T. Betz, C. Koller, M. Goebel, A. Perrin, J. Schmiedmayer, and T. Schumm. Stochastic optimization of a cold atom experiment using a genetic algorithm. *Applied Physics Letters*, 93:264101, 2008.

[74] C. Darwin. On the origin of species by means of natural selection, or the preservation of favoured races in the struggle for life. *New York: D. Appleton*, 1859.

[75] I. Rechenberg. Evolutionsstrategie–Optimierung technisher Systeme nach Prinzipien der biologischen Evolution. 1973.

[76] J.H. Holland. Adaptation in natural and artificial systems. 1975.

[77] T. Weise. Global Optimization Algorithms–Theory and Application. *URL:* `http://www.it-weise.de` , Abrufdatum, 1, 2008.

[78] M. Mitchell. *An introduction to genetic algorithms*. The MIT press, 1998.

[79] K. De Jong and W. Spears. An analysis of the interacting roles of population size and crossover in genetic algorithms. *Parallel problem solving from nature*, pages 38–47, 1991.

[80] J.H. Holland. Adaptation in natural and artificial systems. 1975. *Ann Arbor MI: University of Michigan Press.*

[81] J.M. Fitzpatrick and J.J. Grefenstette. Genetic algorithms in noisy environments. *Machine Learning*, 3(2):101–120, 1988.